A Quantitative Analysis of Hemodynamic Forces on Cellular Response

Alexander Thomas White

Department of Materials Science and Engineering

University of Sheffield

A thesis submitted for the degree of

Doctor of Philosophy

2013

Acknowledgements

First and foremost, I would like to thank my supervisor Dr Chuh K. Chong for giving me the chance to undertake this project and for his invaluable support and patience throughout my PhD studies. Thanks also to my second supervisor Prof. Paul Evans for his valuable help and advice.

I would also like to thank all of the members of Dr Chong's and Prof. Evans' research groups and the wider tissue engineering research group. Particular thanks to Claire Johnson, Mark Wagner and Robert Dickinson for their technical support, Nii Armah-Armah, Lindsey Dew, Schweta Mittar, Le Luong and Guilia Gigliobianco for their help and input with my experimental work and Bernadette Deere for her help with my image processing work.

Finally, I would like to thank my family and my girlfriend Madeleine Treavis for their support throughout my studies.

Abstract

Mechanical forces are known to be important in various physiological and pathological processes, including the development of atherosclerosis. In particular it is believed that abnormal shear stress, transduced by the vascular endothelium, is particularly important in promoting atherogenesis. However, it is still unclear to what extent the precise details of the mechanical environment to which the vascular endothelium is subjected affect its response. Therefore, a novel flow-bioreactor system has been developed which is capable of subjecting endothelial cells cultured *in vitro* to various mechanical parameters at similar levels to those applied *in vivo*. The fluid dynamics within the flow-bioreactor system has been analysed computationally to accurately quantify the mechanical forces experienced by cells cultured within the flow-bioreactor system, and a validation of the computational model used has been performed to ensure the accuracy of the results of the computational fluid dynamics analysis.

The flow bioreactor system has been used to subject human endothelial cells to physiologically realistic mechanical forces for up to 24 hours. The cells were shown to realign in the direction of the shear stress and elongate in response to the application of WSS, consistent with the results shown both in other mechanical models and *in vivo*. A computational image processing programme has been developed to accurately quantify the

morphology of cells. Quantitative analysis using this programme showed that the degree of realignment and elongation was significantly dependent on the local cell density.

The enabling technologies developed during this project may help with future work aimed at elucidating the features of the mechanical environment which are important in promoting or suppressing atherogenesis.

Contents

List of Figures

List of Tables

Nomenclature

Roman Symbols

A	Surface area
b	Breadth of flowchamber
c	Speed of sound
CV	Control volume
e_i	Velocity component in direction i
F	Force due to presence of a field
f	Probability distribution function
g	A function defining flow rate vs time for a pulsatile flow waveform
g_{osc}	The oscillatory component of g
H	Shortest length scale of flow
h	Height of flowchamber
Kn	Knudsen number
l	Characteristic length scale
L_e	Entrance length
l_m	Molecular mean free path

m	Gradient of line of best fit
Ma	Mach number
p	Pressure
Q	Volume rlow rate
r^2	Coefficient of determination
Re	Reynolds Number
T	Time for one complete cycle
t	time
u	Velocity
Wm	Womersley number
x	Position
x'	Modified position

Greek Symbols

ϵ	A measure of axisymmetry
μ	Viscosity
ν	Kinematic viscosity
ω	Highest angular frequency of oscillations
ρ	Density
σ	Variance
τ^*	Component of WSS vector that acts at either 90 or 180 degrees to the mean WSS direction
τ_w / τ	Wall shear stress

θ Angle

Other Symbols

$\mathbf{M}$ Moment of distribution function

$\mathbf{n}$ Vector normal to a face

Acronyms

BGK Bhatnager, Gross, Krook

CFD Computational fluid dynamics

EC Endothelial cell

ECM Extrecellular matrix

F-BS Flow-bioreactor system

FEM Finite element method

FVM Finite volume method

LAD Left anterior descending coronary artery

LBM Lattice Boltzmann method

MSE Mean squared error

OSI Oscillatory shear index

PA Poplitial artery

PIV Particle image velocimetry

PPFC Parallel plate flowchamber

RCA Right coronary artery

SFA Superior femoral artery

SMA Superior mesenteric artery

SMC Smooth muscle cell

SWSSG Spatial wall shear stress gradient

TWSSG Temporal wall shear stress gradient

WSS Wall shear stress

Chapter 1

Introduction

1.1 Background

1.1.1 The Arterial System

The arterial system is a large, branching network of muscular tubes. It facilitates the distribution of blood from the heart to organs and cells which require a continuous supply of oxygenated blood for normal homeostasis.

A normal artery consists of three distinct layers, the intima, or endothelium, the media and the adventitia, as shown in figure 1.1. The endothelium is a monolayer of endothelial cells (ECs) which are in direct contact with the flowing blood. The ECs are attached to the internal elastic lamina. The intima provides an antithrombotic surface and regulates mass transport to and from the blood. Underneath the endothelium is the media, which is composed largely of smooth muscle cells (SMCs) and is responsible for regulating vascular tone. Finally the adventitia is composed of a mixture of fibroblast cells, smooth muscle cells and connective tissue which provides mechanical

support for the artery.

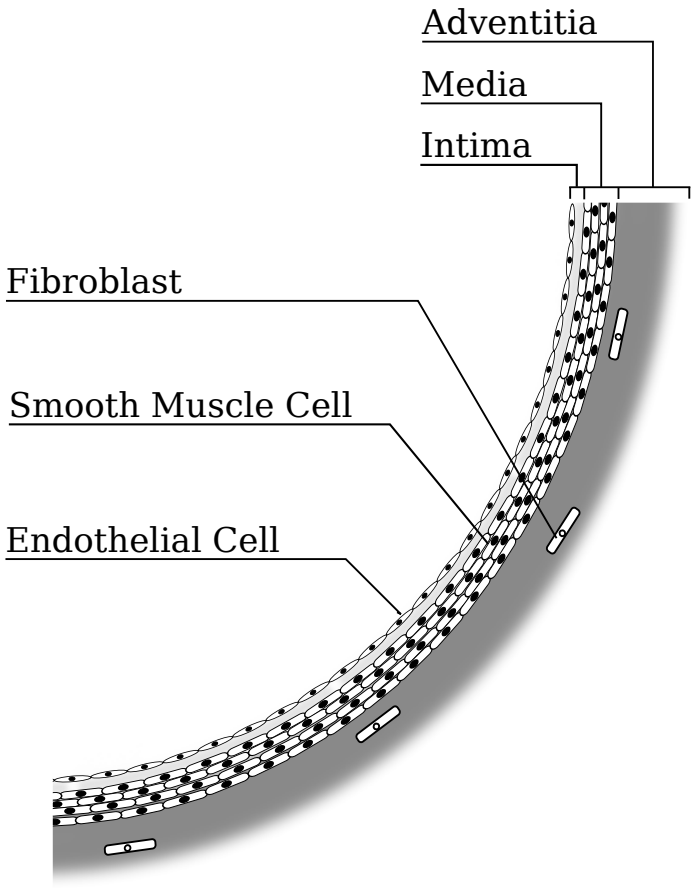

Figure 1.1: Anatomy of the arterial wall.

Arteries are constantly subjected to mechanical forces. The pressure of the flowing blood causes hoop stresses and compressive stresses in the arterial wall and the flexing of the artery may also cause a longitudinal stress. A much smaller shear stress in the direction of the flowing blood is also applied to the wall of the artery. It is clearly extremely important that arteries remain able to withstand these stresses throughout the life of an individual.

To properly perform their challenging physiological function arteries are biologically active and continuously adapt to both acute and chronic changes in their mechanical environment through complex biologically regulated feedback mechanisms. For example, the thicknesses of the medial and adventitia layers may change depending upon the flow rate and pressure in an artery and the lumenal diameter of an artery is known to change depending on the flow rate within an artery [94; 137].

To adapt to changes in the flow rate arteries must sense the mechanical forces applied to them by the blood. Whilst many factors are important in determining the pressure in a particular artery, the wall shear stress (WSS) applied by the flowing blood is closely related to the local flow rate, particularly if the flow is laminar and the geometry of the blood vessel is regular. Therefore WSS is the most likely stimulus for causing arteries to respond to changes in flow rate. As ECs line the inside of arteries they are ideally placed to transduce the WSS applied by flowing blood. It has been shown that arteries remodel in response to changes in flow rate in such a way that the WSS experienced by the ECs returns to the same level that it was at before the change in flow rate. ECs are believed to be largely responsible for this flow dependent mechanotransduction in arteries, as remodelling on both long and short time scales has been shown to depend on an intact endothelium [36; 94].

1.1.2 Atherosclerosis

Atherosclerosis is a disease of the arterial wall characterised by abnormal hardening and thickening. Atherosclerosis is the leading cause of morbidity and mortality in the developed world [177] and is likely to become the leading cause of death in the world in the future [116].

Clinical problems as a result of advanced atherosclerosis can arise chronically due to a reduction in blood flow, or ischemia, caused by occlusion of too great a proportion of the artery supplying a particular organ. If left untreated this can ultimately lead to gangrene and the loss of the affected organ. Surgical intervention is usually required to remove the blockages due to advanced atherosclerosis. These interventions pose a risk to the patient and place a considerable burden on global health services [134]. More acute consequences include strokes, critical acute limb ischemia and myocardial infarction. These occur when a thrombus forms on the tip of an advanced atheroma, becomes detached (forming an embolus) and is carried downstream by the flowing blood. The embolus can then either fully or partially occlude a downstream artery, leading to sudden, dramatic loss of blood flow to the organ supplied by the occluded artery. This can potentially cause permanent damage to the organ supplied and, depending on the extent of the damage, the death of the individual.

Atherosclerotic lesions, or atheroma, can be categorised based on their severity [147; 148]. Initial, type I, lesions consist of microscopic patches where small numbers of lipids and circulating cells have passed through the endothelium. These lesions are present in most infants and are always asymptomatic.

The first macroscopic changes to the arterial wall are termed type II lesions, or fatty streaks. Fatty streaks occur when circulating cells pass through the endothelium and then differentiate into macrophages, which then consume lipids to become foam cells [68]. It is these foam cells that give early lesions their 'fatty' appearance. These lesions are particularly prevalent in individuals with hypercholesterolimia as this condition increases the likelihood that lipids will pass through the endothelium, inducing ECs to express adhesion molecules such as VCAM-1 [68; 101] that cause circulating cells to adhere to and then pass through the endothelium. Fatty streaks are present in most

individuals from early adulthood and they do not cause clinical problems [148].

At the later stages of atherosclerosis the plaque may be termed a type III, or intermediate, lesion. At this stage the cells within the lesion begin to express chemoattractant factors, causing the recruitment of SMCs from the media into the intima. There will also be more intracellular and extracellular lipids and the plaque will begin to produce extracellular matrix (ECM) [148].

If the lesion progresses further then more SMCs will be recruited into the lesion and they will proliferate and produce more ECM. This leads to the formation of a fibrous cap on top of the lesion. The fibrous cap is important in determining the ultimate fate of an atheroma as it has a significant influence on the likelihood that a plaque will rupture [120].

At this stage the atheroma is termed a complex or type IV lesion. It is possible that the cells in the middle of the lesion may die, mostly by necrosis but also through apoptosis. These dead cells can form a necrotic core in advanced lesions [142]. Clinical symptoms as a result of the plaque are unlikely to be observed until the plaque progresses to this stage.

The tip of complex lesions is subjected to abnormally high WSS because the reduced lumenal area causes an increase in blood velocity. This can cause the tip of the lesion to rupture. If this occurs then blood comes into contact with the pro-thrombotic surface of the underlying plaque. This causes a thrombus to form from circulating platelets, which is likely to grow at a much faster rate than the lesion itself [69]. After the formation of a thrombus clinical consequences due either to ischemia of the organ supplied by the affected artery or the detachment of the thrombus and subsequent blocking of a smaller artery become increasingly likely. This can cause a potentially fatal myocardial infarction, stroke or pulmonary embolism. These events are the most

frequent causes of death due to atherosclerosis [120].

The particularly high incidence of clinical problems caused by atherosclerosis in the developed world is largely due to the prevalence of obesity and other cardiovascular risk factors such as smoking, sedentary lifestyle and advancing age [134]. However, despite the systemic nature of all the common risk factors, it has long been known that atheroma preferentially locate to particular areas of the vasculature, for example; [132]. It has been hypothesised that this focal distribution may be due to variations in mechanical forces in different areas of the vasculature [18; 57]. The following section will discuss the evidence for this hypothesis and the potential role of mechanical forces in promoting or reducing atherogenesis.

1.1.3 The Role of Mechanical Forces

1.1.3.1 Localisation of Atheroma

The lumenal surface of blood vessels is constantly subjected to mechanical forces by flowing blood, as shown in figure 1.2. Pulsatile circumferential stress, or hoop stress, is applied to the cells because of the variations in pressure over the cardiac cycle. WSS is applied due to the viscosity of the flowing blood. In normal arteries the average magnitude of WSS is approximately 1.5Pa [63]. However, the WSS applied to the vascular wall is a strong function of both the flow rate, flow waveform and the local vascular geometry. Therefore there are strong spatial and temporal variations in WSS within the arterial system, with localised regions of much lower and much higher WSS. It has been hypothesised that the focal distribution of atherosclerosis is due to these variations in WSS [18; 19; 57]. It was initially hypothesised that damage to the endothelium caused by high WSS was responsible for the localisation of atheroma, and evidence

from studying the distribution of the disease in laboratory animals supported this hypothesis [57]. However, evidence obtained from human arteries at autopsy showed a contradictory distribution [18; 19] and low and oscillating WSS are now widely believed to be important in the development and progression of atherosclerotic plaques [30; 168].

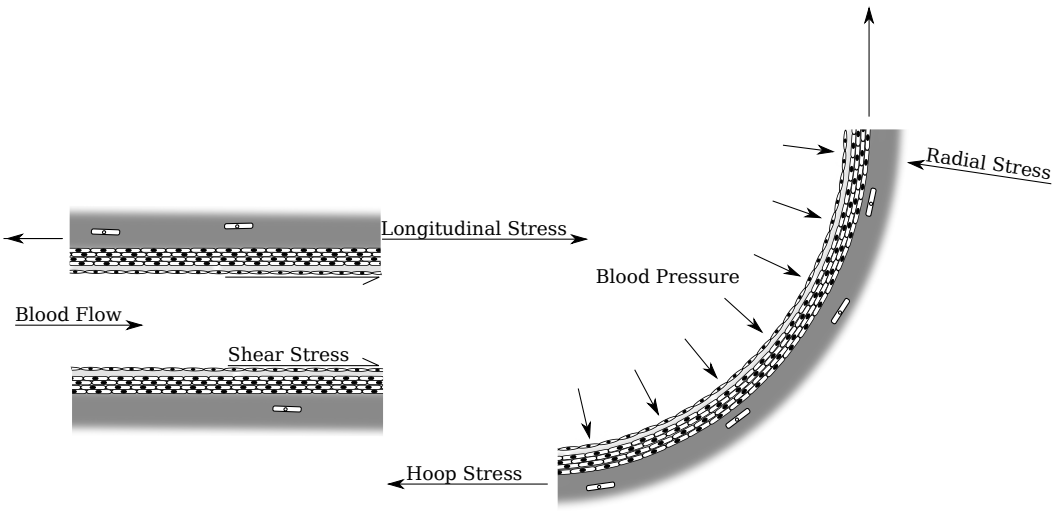

Figure 1.2: Diagram of the stresses experienced by the arterial wall.

Much of the initial evidence in favour of this hypothesis was derived from autopsy studies describing the distribution of atherosclerotic plaques around the vasculature. Initial observations showing that atheroma localise to parts of the vasculature where WSS is low were presented by Caro *et al* [18; 19]. In these papers a correlation between areas where low WSS was expected based on experimental work and theoretical estimations and the development of early atheroma in several human subjects was observed. The locations shown to be particularly prone to the development of atheroma

included the posterior wall of the curved descending thoracic aorta or the outside 'hips' of a bifurcation. These papers were the first to show the correlation between low WSS and development of atheroma. In them the investigators conjectured that the localisation was due to shear dependant mass transfer phenomena. This hypothesis is still being actively researched today, although alternative hypotheses have also been proposed [152; 164; 165; 167].

The seminal works of Caro and co-workers were able to show qualitative evidence that atheroma develop preferentially in areas of low WSS. However, because they were not able to accurately quantify the WSS in the arterial geometries studied they were unable to perform statistical analysis to establish the strength or significance of the observed correlation. Later investigations have been able to quantify the WSS applied by physiologically realistic flow waveforms to the endothelium by the flowing blood and thus find quantitative correlations between mechanical parameters and plaque thickness. Ku *et al* performed one such study using laser doppler velocimetry to find the WSS distribution in a model carotid bifurcation. Comparison was then made between the WSS distribution and intimal thickness in 12 human carotid bifurcations obtained at autopsy [93]. Significant correlations (all $p < 0.001$) were found between the intimal thickness and the inverse of maximum and mean WSS and an oscillatory shear index (OSI) defined as a quantitative measure of WSS reversal using the following equation:

$$OSI = \frac{\int_0^T |\tau_w| dt}{\int_0^T |\tau^*| dt} \tag{1.1}$$

where τ_w is the WSS vector and τ^* is the component of the WSS vector that acts in either the opposite direction to the mean WSS or at 90 degrees to the mean WSS. Although the geometry was not exactly the same between the model and the specimens,

the model geometry was obtained physiologically and it is reasonable to expect that the variations in WSS distribution would not have affected the conclusions.

Further studies have compared the distribution of intimal thickening and atherosclerosis, with very few studies dissenting from the view that there is a strong correlation between low WSS and atherosclerosis [4; 86; 130; 188]. One study which did contradict the view that low WSS is important in atherogenesis studied the flow patterns and intimal thickness in four human right coronary arteries and showed a correlation between low WSS and intimal thickness for one but not the other three [86]. This study did find a correlation between WSS and intimal thickness for the other three arteries when the co-dependence of WSS and axial and radial location was ignored, but this correlation disappeared after taking into account the dependence of intimal thickness on axial and radial position.

Strong evidence supporting the hypothesis that atheroma preferentially locate to areas of low shear and disturbed flow was provided by Ravensbergen *et al* [130]. This study showed that the correlation between intimal thickness and low WSS observed in bifurcations is also observed in the vertebrobasilar junction. As this is a confluence of arteries the flow pattern is quite different to that observed in a bifurcation. However, even in this altered flow regime a similar correlation between locations of low WSS and intimal thickness was observed [130].

In addition to correlations between atheroma location and WSS values observed at autopsy it has also been shown that long term changes in arterial diameter are significantly correlated with low WSS values, suggesting that low WSS is important in both the development and progression of atheroma [60].

Surgical interventions to restore the flow in an occluded artery frequently fail due to neointimal hyperplasia. Neointimal hyperplasia often involves intimal thickening

happening at a much higher rate than in normal atherogenesis due to the injury sustained by the arterial wall during surgery. A correlation between locations of intimal hyperplasia and low WSS has also been observed [80; 90]. This suggests that low WSS works in conjunction with the injury to the arterial wall to promote inflammation.

Given the observed correlation between disturbed flow and the development of atheroma it has been hypothesised that having an arterial geometry which is likely to promote disturbed flow may be a risk factor for atherogenesis [55; 176; 190]. Wood *et al* [176] showed that the superior femoral artery (SFA) is more curved in men than in women and that this leads to flow patterns which are more likely to promote atherogenesis in the SFA of men than women. The investigators conjectured that the hemodynamic differences between men and women may explain their difference in the prevalence of peripheral arterial disease [33; 176].

A similar correlation between locations of atheroma and low WSS has been observed in some laboratory animals [158]. A causal link between low and oscillatory WSS and the development of atheroma has also been observed in mice [24]. In this study the investigators surgically altered the geometry of mouse carotid arteries to induce areas of low, oscillatory and high WSS. It was found that atheroma developed significantly more in areas of low and oscillatory WSS compared to areas of high WSS and sham operated controls.

Although the relationship between low WSS and atherogenesis has gained widespread acceptance in the literature it is worth noting that a recent systematic review performed by Peiffer *et al* concluded that the correlation is not as strong as is widely believed [123]. This review concluded that whilst the correlation appeared to be strong when visual comparisons were made between the distributions of atheroma and locations of disturbed flow (and consequently low/oscillatory WSS), more rigorous methods which

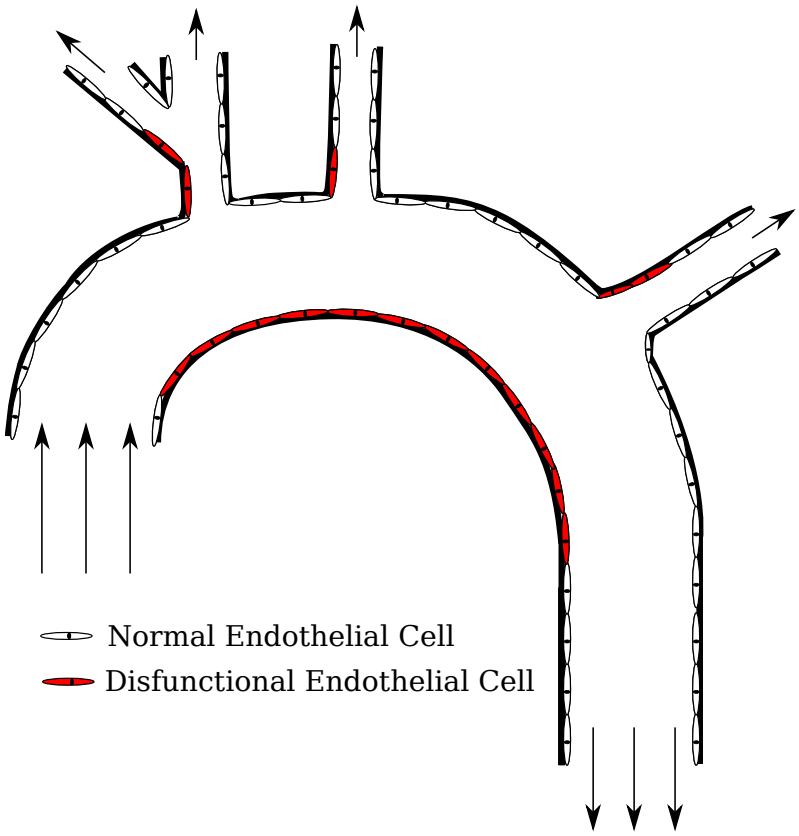

Figure 1.3: Locations in the human and mouse aorta that are most prone to atherosclerosis. In these locations flow separation is more likely to occur, causing the endothelium to experience an altered shear environment. Atheroprone locations taken from [158]

made point-by-point comparisons between the two distributions were unable to find a statistically significant correlation.

Only five studies meeting the criteria for inclusion in the systematic review by Peiffer *et al* produced point-by-point comparisons between WSS and the location of disease [5; 61; 86; 149; 169]. None of these studies found a statistically significant correlation between the location of atheroma and low or oscillatory WSS. However, it should be noted that the level of significance depended on the way in which the sta-

tistical analysis was performed, as Joshi *et al* [86] observed a statistically significant correlation if normalisation of the intimal thickness at each cross section was not performed, although this correlation disappeared in all but one of the four arteries they studied if normalisation was performed. Similarly, Wentzel *et al* [169] observed a significant correlation if the data were averaged in the axial direction but not if averaging was not performed. Therefore it is important to determine what type of data reduction is appropriate to correct for the variations in intimal thickness in healthy arteries.

As the level of correlation between low and/or oscillatory WSS and intimal thickening remains controversial it has been postulated that other mechanical parameters, which could frequently co-localise with low WSS, may be important in promoting atherogenesis. These parameters include high SWSSG [97] and directional oscillatory WSS [20]. Both of these parameters are likely to be observed at the regions exposed to disturbed flow where atheroma are believed to preferentially locate. Further work investigating the relationship between different mechanical parameters and the location of atheroma is therefore necessary to elucidate the role of mechanical forces in atherogenesis.

1.1.3.2 Arterial Fluid Mechanics

The complex geometry of arteries and the pulsatile nature of blood flow leads to significant variations in flow patterns and WSS throughout the arterial system. The link between atherosclerosis and WSS has led to an interest in quantifying the fluid mechanical environment expected to be experienced by ECs *in vivo*, particularly at locations where disturbed flow is expected. This can be achieved using either experimental or computational models.

Early studies examining the link between localisation of atheroma and fluid me-

chanical forces obtained data on the distribution of WSS using idealized models of arteries [18; 93]. Depending on the flow visualisation method employed these methods obtained either qualitative [18] or quantitative data [93]. These studies were able to gain extremely valuable insight into the localisation of atherosclerosis. However, due to the significant variation in arterial geometry observed between individuals there has been interest in quantifying the WSS and pressure distribution in patient-specific models of human arteries [153].

Obtaining reliable data on the *in vivo* fluid mechanical environment is challenging because of the pulsatile, non-Newtonian nature of the flow and the potentially complex, compliant geometry of arteries. Several studies have used physical models of arteries and flow visualisation techniques to study the flow patterns within arteries [111]. Advances in computational fluid dynamics (CFD), increases in the available computational resources and improvements in medical imaging have also made it possible to produce accurate, physiologically realistic CFD models of blood flow in an individual's arteries.

The shear environment in the relatively atheroprotected superior mesenteric artery (SMA) was characterised by Jeyes *et al* in a patient specific compliant geometry. The WSS distribution was found to be fairly unidirectional, as indicated by low OSI, for the majority of the arterial wall. However, close to the bifurcation a region of high OSI was observed. This location is coincident with clinical observations of atheroma in the SMA. The evolution of WSS in the region of high OSI was shown to be highly two dimensional, with similar magnitude of shear observed in the transverse and axial directions [85]. Similar characterisations have been performed for other arteries of interest, including the carotid [34], coronary [91] and femoral [176] arteries.

Potential applications of patient specific modelling of haemodynamics include re-

search into the fluid mechanical environment which causes arterial diseases, designing tissue engineered or artificial bypass grafts and planning vascular interventions to optimise the fluid mechanical environment [181] and predicting the likely vulnerability of observed pathologies such as aneurysms and vulnerable atheroma [153]. Predicting aneurysm vulnerability would be particularly clinically useful as surgical intervention carries significant risks which may outweigh the benefits for low risk aneurysms, making it unclear whether or not an operation is justified. For these applications to be effective clinically it is necessary to characterise which mechanical parameters are most important in the development of different vascular pathologies. The clinical effectiveness of patient specific CFD modelling may also be improved by the development of CFD platforms that can reliably produce computational meshes from medical images and produce accurate flow fields with minimal user input. The lattice Boltzmann method (LBM) may therefore be a promising candidate for use in patient specific blood flow modelling thanks to its easy mesh generation and relatively low computational cost [113]. However, it should be noted that LBM is still an emerging technology and other, more established and widely used CFD models which are capable of simulating blood flows in physiologically realistic geometries also exist, and it may be preferable to use such models, for verification purposes. Validation of the results of conventional CFD analysis on physiologically relevant blood flow models has been performed, showing that well performed CFD analysis is capable of accurately reproducing experimentally observed flow patterns [71; 179].

Morphological changes in ECs are believed to correlate with the WSS distribution [14]. Therefore the morphological response of ECs has been used to infer the local WSS patterns in rabbits and mice of different ages [14]. This study was able to show correlation between the local morphological features of ECs and localisation of

atheroma . However, it should be noted that this study showed a correlation between areas of high WSS and atheroma development, in contrast to the findings of other studies on the localisation of atheroma [18; 24; 93]. This discrepancy suggests that the localisation of atheroma may depend on more complex WSS related parameters such as OSI, TWSSG or SWSSG rather than simple low WSS, although it should also be noted that the species difference may explain this unexpected finding as other studies have also shown that atheroma localise towards areas of high WSS in cholesterol-fed rabbits [122]

1.1.3.3 Endothelial Cell Mechanotransduction

The physiological location of ECs makes them uniquely well placed to sense the WSS applied to the vessel wall by the flowing blood. A large body of evidence supports the hypothesis that shear stress has a controlling influence on various arterial processes including development, normal physiology and pathologies [30; 66]. There is a large body of evidence suggesting that ECs are able to transduce mechanical forces in a variety of different ways [27]. Various potential mechanotransducers have been suggested as mechanisms by which ECs sense WSS. These include the glycocalyx and the primary cilia, which reside on the lumenal side of ECs and may transduce the shear forces applied directly, and the cytoskeleton, cell-matrix adhesion molecules and cell-cell adhesion molecules, which may transduce the stresses caused by the application of the WSS to the lumenal side of the EC.

Endothelial cells have been shown to be covered by a dense glycocalyx attached to the lumenal plasma membrane [144; 161]. As the outermost part of an EC this glycocalyx is ideally placed to directly transduce WSS. An important role for the glycocalyx in EC mechanotransduction has been suggested by studies which have shown

EC responses to WSS to be significantly inhibited when part of the glycocalyx is enzymatically digested [166]. However, it is possible that the enzymatic digestion may have also affected other potential mechanotranducers, so the inhibition of the responses to WSS may not have been entirely due to the damage to the glycocalyx.

Primary cilia are thin microtubule containing rods which protrude from the outer surface of many different cell types. Whilst arterial ECs do not typically express detectable primary cilia it has been shown that ECs cultured in static conditions do express a primary cilium, which is disassembled in response to the application of WSS [83]. A small proportion of ECs at locations of the vasculature where WSS is low and atherosclerosis is more likely to occur have also been shown to express a primary cilium in ApoE$^{-/-}$ mice [76]. These results suggest that whilst the primary cilia have no role in the transduction of WSS in the range that ECs usually experience in arteries, they may have a role in transducing smaller WSS values which could not be adequately detected by other mechanotransducers. The production of a primary cilium when WSS is low highlights the importance of shear stress stimuli in EC biology.

EC mechanotransduction has been shown to be inhibited by disruption of the cytoskeleton [81; 139]. These results could either suggest a role for the cytoskeleton in direct mechanotransduction or that the cytoskeleton is necessary for other mechanotransducers to function effectively. Adhesion receptor dependent mechanotransduction mechanisms have been also discovered [156].

In vivo ECs are subjected to both WSS and cyclic stretch. Despite the fact that the stress applied by the cyclic stretch is likely to be at least two orders of magnitude greater than that applied by the shear [89] it appears that WSS is the dominant mechanical stimulus in determining the response of ECs [30]. This suggests that mechanoreceptors on the lumenal side of the EC are best placed to detect WSS stimuli as any

stress caused by shear in the cytoskeletal proteins and adhesion receptors is likely to be much smaller than that caused by the cyclic stretching.

1.1.3.4 Effects of Fluid Forces on Vascular Cells

The relationship between shear stress and the development of atheroma has led researchers to study the response of ECs to WSS, both *in vitro* and in animal models. This work has achieved considerable success in characterising the response of ECs to WSS and it has been shown that many of the properties of ECs are regulated by WSS, including morphology and cytoskeletal alignment [40; 54; 58], expression of vasodilators [32; 183], permeability [165; 167] and gene expression [38]. This section will summarise the findings of this research and discuss its relevance to the development of atherosclerosis.

The most obvious change that occurs as a result of application of physiological WSS to cultured ECs is a change in their morphology. Unstimulated ECs show a 'cobblestone' morphology with no clear alignment or elongation. ECs exposed to physiologically relevant WSS have been shown to elongate and align with the direction of the WSS within 4-6hrs of its application [58]. ECs also reorganise their cytoskeleton in a time dependant manner in response to the application of steady WSS [54; 58]. *In vivo* ECs have also been shown to realign in the direction of flow in a manner that depends primarily on the mean WSS value [14; 119]. The morphology of EC nuclei has also been studied, with a similar response change in morphology observed for the nucleus to the entire cell [14].

EC morphology is important because ECs at locations *in vivo* where atheroma are more likely typically show more rounded morphology than those at atheroprotected sites [30]. It is important to study the effects of WSS on EC morphology as an aligned,

elongated morphology shows that the ECs exposed to physiological levels of WSS *in vitro* are responding in a similar way to ECs *in vivo*. It has been shown that an elongated, aligned morphology predisposes ECs towards an anti-inflammatory phenotype, with lower monocyte adhesion and VCAM-1 expression but higher KLF2 expression [159]. These results were found irrespective of whether the morphological changes were induced by application of atheroprotective WSS or by micropatterning of the cell culture surface.

Arteries are known to dilate and contract so as to keep the WSS at a constant level, in a process which depends on an intact endothelium [94]. ECs have been shown to secrete the visodilator nitric oxide (NO) in response to the application of WSS both *in vivo* and *in vitro* [32; 52; 183]. Shear dependant vasodilation controls the blood flow through an artery. For this response to be effective it is important that the WSS experienced by the ECs is a reliable indicator of the flow rate through the artery. In a relatively straight artery this is always likely to be the case, with the WSS linearly proportional to the flow rate and inversely proportional to the third power of the diameter of the artery. However, if the flow is disturbed then this relationship will no longer hold. This may cause the artery to inaccurately regulate the blood flow through itself.

The turnover rate of ECs has also been shown to be affected by WSS, with ECs exposed to physiological WSS showing a reduced rate of proliferation relative to static controls [1]. A similar effect has also been observed *in vivo*, with areas of normal laminar WSS showing lower proliferation rates than areas of disturbed WSS in laboratory animals [178; 182]. It has been hypothesised that EC turnover is important in the development of early atherosclerotic lesions because EC barrier function is weaker during mitosis than during the other phases of the cell cycle, potentially allowing more of the circulating molecules which cause early lesions to pass through the endothelium.

WSS related changes in morphology, turnover and other endothelial functions are controlled by extremely complex molecular signalling pathways [107; 189]. Research into the effects of WSS on these signalling pathways has shown that many of them are extremely sensitive to WSS and that high, unidirectional WSS and low and/or oscillatory WSS often have opposite effects. For example, it has been shown that a sinusoidal waveform with a pulse amplitude of 0.4Pa and a mean value of 1.2Pa significantly upregulates the transcription factor KLF2 whilst an oscillatory WSS waveform with the same pulse height significantly inhibits KLF2 [163]. These findings were in agreement with data obtained on the KLF2 expression at different locations in the endothelium of both normal and surgically altered rat arteries. KLF2 is believed to have an atheroprotective effect through suppression of inflammation [62].

Research into the effects of WSS on the molecular biology of ECs is important because it provides insight into the pathology of atherosclerosis. This information can be extremely valuable in identifying targets for novel drugs and for assessing the potential of drugs which have been developed [187]. In addition to its importance in the development of atherosclerosis, WSS has been shown to significantly affect the response of ECs to certain drugs, reducing their effectiveness at locations which are prone to atherosclerosis but increasing their effects at atheroprotected sites [2; 135].

1.1.3.5 Effects of Different Fluid Mechanical Parameters on Vascular Cell Response

The majority of the work on the effects of WSS on EC performed to date investigated the effects of relatively simple WSS waveforms, typically either a steady WSS or a non reversing sinusoidal waveform to mimic normal, atheroprotective WSS and either a low or an oscillatory WSS to approximate an atheroprone waveform. *In vivo* cells

experience a complex flow environment which applies two dimensional WSS waveforms with higher frequency oscillations and high T/SWSSG in addition to the WSS and oscillatory flow stimuli. Many innovative experiments have been performed to elucidate the different effects of these parameters. However, there is still considerable uncertainty regarding the different contributions of these stimuli and the importance of properly mimicking the physiological WSS environment when subjecting ECs to WSS. This section will describe some of the experiments performed to date and discuss the questions which are still open regarding the response of ECs to complex fluid mechanical stimuli.

Cultured ECs have been shown to respond differentially to laminar and turbulent flow, with turbulent flow significantly increasing EC proliferation, causing a different gene expression profile to laminar flow applying a similar mean WSS value. ECs exposed to laminar flow also showed realignment in the direction of the flow, while ECs exposed to turbulent flow did not [37; 59]. Other studies exposing cells to laminar and turbulent flow have shown that certain biological responses of ECs are significantly different depending on whether the flow is turbulent of laminar, whilst other responses are qualitatively similar between the two types of flow [59; 106].

Turbulent flow is inherently unsteady and spatially non uniform. Therefore a turbulent flow is likely to apply gradients in WSS in both space and time, which are likely to be experienced by cells at atheroprone sites *in vivo*. However, as turbulence rarely occurs *in vivo* the frequency of the oscillations under turbulent flow are likely to be much higher than the oscillations caused during the normal cardiac cycle. The magnitude of the T/SWSSG applied under turbulent flow are also likely to be different to those experienced by cells *in vivo*. Therefore, whilst studies applying turbulent flow are able to demonstrate that ECs have extremely sensitive mechanotransducers which

are able to sense and respond to both the time averaged WSS value and fluctuations about it, the model is not suitable for mimicking the WSS environment present *in vivo* or for separating the different effects of OSI and T/SWSSG as these parameters cannot be individually controlled.

To mimic the frequency of the WSS oscillations and the TWSSG experienced *in vivo* many investigators have exposed cultured ECs to physiologically realistic WSS waveforms [9; 16; 34; 184]. Dai *et al* exposed cultured HUVECs to WSS waveforms typical of either atheroprone or atheroresistant areas of the carotid artery. The WSS waveforms were derived from a CFD simulation using a physiologically measured arterial geometry and flow waveform as boundary conditions. Microarray analysis clearly showed that the two waveforms evoked different phenotypes in the cells, with the atheroprone waveform upregulating genes relating to proliferation and atherogenesis whilst the cells exposed to the atheroprotective waveform upregulating genes known to slow or prevent atherogenesis, including KLF2.

Experiments subjecting ECs to physiological WSS waveforms are able to more closely mimic the *in vivo* flow environment than experiments using either turbulent WSS or simple, non physiological waveforms. However, it is not clear how sensitive ECs are to the precise details of the WSS waveform to which they are subjected.

To elucidate the different effects of the different mechanical parameters that ECs experience *in vivo* many investigators have subjected cells to well defined laminar flow profiles which apply TWSSG or SWSSG either individually or in combination. Helmlinger *et al* studied the calcium signalling response of ECs from bovine aorta subjected to different shear patterns [77]. WSS was found to increase intracellular free Ca^{2+} in a manner which depended primarily on the average WSS magnitude. This increase was not observed when the flow was purely oscillatory but pulsatile WSS with a re-

versing component produced a similar response to a steady flow of a similar average magnitude. Altering the frequency of the oscillations in pulsatile flow did significantly affect the results, suggesting that the mean WSS was the most important factor in determining the peak amplitude of the response, although pulsatile reversing and pulsatile non reversing WSS conditions did alter the time course of the response compared to steady WSS. It should be noted that this study investigated the response of ECs over very short timescales (<15 mins). Therefore, whilst it clearly demonstrates that EC mechanotransducers are capable of discriminating between different flow patterns when responding to an acute change in their mechanical environment it is difficult to speculate on the long-term physiological effects of the different WSS waveforms based on the results of this study.

Yee *et al* subjected human umbilical vein endothelial cells (HUVECs) to both physiologically realistic pulsatile, non-reversing WSS and a steady WSS of the same average magnitude and examined the gene expression profiles that resulted. This study showed that of the genes which were regulated differently between mechanically stimulated cells and static controls the majority (928) were regulated in a similar manner by both mechanical stimuli. However, 343 genes were differently regulated by the two stimuli [183].

A number of studies in the Frangos laboratory have demonstrated that ECs respond differently to steady WSS, TWSSG and SWSSG [6; 7; 174; 175]. These studies showed that TWSSGs were able to significantly enhance EC proliferation whilst steady WSS reduced proliferation. SWSSGs were also found not to enhance EC proliferation, although the combination of TWSSG and SWSSG did cause a significant increase in proliferation. In these studies TWSSG were applied by WSS waveforms which either stepped between zero to a maximum WSS of 1Pa at a frequency of 1Hz or with one

single impulse stepping the WSS from 0 to 1Pa. However it should be noted that many of the experiments were quite short term (10 mins - 4 hrs) and so the results observed may not represent the steady state response of cells to the mechanical parameters investigated. It should also be noted that the sudden onset flow is a non-physiological waveform likely to generate TWSSG which are much higher than those expected *in vivo*. Despite these limitations, these experiments clearly showed that ECs can sense and respond to different gradients in WSS.

Further studies investigating the response of ECs to SWSSG at various levels have been performed. The effects of very high SWSSG (4 - 34Pa/mm) due to impinging flow were investigated by Sakamoto *et al* [138]. At these high levels it was shown that SWSSG either reduced or completely prevented the alignment in the direction of flow and elongation of HUVECs that was observed when applying the same mean WSS value to the cells without the SWSSG. The very high SWSSG applied in this study are only likely to occur *in vivo* in highly localised regions close to the apices of bifurcations.

The effects of more physiological SWSSGs, and the different effects of accelerating and decelerating SWSSG, have been studied by Dolan *et al* [43]. This study showed that an accelerating SWSSG of approximately 10Pa/mm induces EC turnover through proliferation and apoptosis whilst decelerating SWSSG has the opposite effect. Similar effects were also observed on EC morphology, with accelerating SWSSG inhibiting EC alignment in the direction of flow whilst decelerating SWSSG increased EC alignment. The results showing a reduction in EC alignment when they are exposed to an accelerating SWSSG are in agreement with Sakamoto *et al* [138].

In addition to WSS, ECs *in vivo* are also subjected to a cyclic 'hoop' stretch, which is of a much higher magnitude than the WSS. Although WSS appears to be the domi-

nant factor in determining the location of atheroma [30; 105] it has been hypothesised that cyclic stretch may also be important in determining the response of ECs [25]. There have been a limited number of attempts to elucidate the effects of cyclic stretch and WSS on ECs *in vitro*. For example Breen *et al* subjected cultured HUVECs to combinations of physiologically realistic WSS and cyclic stretch waveforms, with a significantly more ICAM-1 and VACM-1 expression observed in stretched samples when compared to unstretched samples [16].

The majority of efforts to quantify the effects of different mechanical parameters on EC response have been *in vitro* studies. This is likely to be because the fluid mechanical environment is considerably easier to quantify and manipulate *in vitro* than *in vivo*. However, Cheng *et al* have developed a model that alters the mechanical environment experienced by the vascular cells in ApoE$^{-/-}$ mice [24]. This model introduces a cuff onto the outside of the carotid artery of a mouse, causing a converging region in the artery followed by a sudden expansion. Three distinct regions are therefore created, with a region of lowered shear upstream from the cuff due to the reduced flow rate and increased vessel lumen, a region of high WSS and SWSSG in the converging region of the cuff and a region of disturbed, oscillatory flow caused by the sudden expansion downstream from the cuff. After 6 weeks atheroma were found to develop in both the lowered shear and the oscillatory shear regions, but not in the high WSS regions. Additionally, the low shear stress region showed more plaques than the oscillatory region and these plaques showed a more vulnerable phenotype than those in the oscillatory region. This model is a valuable tool for the *in vivo* study of different mechanical environments. However, it should be noted that it is difficult to decouple the effects of the mechanical injuries, increased strain at the arterial wall and pressure variations caused by the cuff implantation from its effects on WSS. In particular, both

the low and oscillatory shear regions are subjected to high strain at the arterial wall, which may disrupt the endothelium. This may have an independent atherogenic effect in addition to the effects of altered WSS. Therefore it is important to combine studies using this model with *in vitro* experiments in which the mechanical environment can be more precisely controlled.

Although significant progress has been made in determining the different effects of WSS and other mechanical stimuli on ECs it is still not clear which parameters are most important in the development of atherosclerosis. Therefore further research into the response of ECs to complex mechanical environments is necessary. Specifically, it is important to determine the long term effects of physiologically realistic combinations of WSS, TWSSG, OSI and SWSSG on ECs. The effects of the two dimensional WSS environment that ECs experience *in vivo* [85] are also currently unknown. This research may have a range of different applications including improved models for studying the effects of atheroprotective drugs on ECs and improving the predictions made by patient specific computational models [2; 153].

1.1.4 Flow Systems for Subjecting ECs to Fluid Mechanical Forces

As discussed in sections 1.1.3.4 and 1.1.3.5, significant progress has been made in our understanding of the effects of mechanical forces on ECs. The design of flow systems employed was critically important in facilitating these advances. For all cell culture studies it is clearly crucial to maintain a stable, sterile environment to provide the cells with sufficient nutrients at the correct temperature, pH and oxygen saturation. In addition to these requirements it is vitally important that flow systems used for studying the effects of WSS on ECs are able to apply accurate, repeatable mechanical stimuli

to the cells for the desired length of time. If more complex mechanical parameters are to be applied to the cultured cells then innovative flow system designs may be required to accurately produce the required forces. Table 1.1 summarises some of the flow systems which have been developed to date and their capabilities. This section will further discuss some of the designs of flow system that have been produced for applying different types of mechanical forces to cultured ECs.

Table 1.1: Flow systems for subjecting ECs to mechanical forces

Reference	**TWSSG**	**SWSSG**	**OSI**	**Physiological waveform**	**Enabling features**
Frangos 1988 [53]	No	No	No	No	Simple, reusable PPFC
Moore 1994 [115]	Yes	No	Yes	No	Combination of WSS and cyclic stretch
Blackman 2000 [11]	Yes	No	Yes	Yes	Programmable for user-defined waveforms
Conklin 2000 [31]	Yes	No	Yes	Yes	Cam system for subjecting *ex vivo* vessels to WSS and cyclic stretch
Peng 2000 [125]	Yes	No	Yes	No	Pulsatile WSS and cyclic stretch
White 2001 [175]	Yes	Yes	Yes	No	Uses different flowchambers for SWSSG and steady WSS
Bergh 2005 [8]	Yes	No	Yes	Yes	System to subject *ex vivo* vessels to WSS and cyclic stretch

Dardik 2005 [35]	Yes	Yes	Yes	No	Simple and repeatable
Song 2005 [145]	Yes	No	No	No	Microfluidic device
Breen 2006 [15]	Yes	No	Yes	Yes	Combination of WSS and cyclic stretch. User defined waveforms
Yee 2006 [184]	Yes	No	No	Yes	Programmable for user-defined waveforms
Punchard 2007 [127]	Yes	No	No	No	Mimic physiological pressure, WSS and stretch
El Kurdi 2008 [45; 46]	Yes	No	Yes	Yes	System to subject *ex vivo* vessels to WSS and cyclic stretch
Nakadate 2008 [117]	Yes	No	Yes	No	Mimic physiological pressure and WSS
Farcas 2009 [49]	No	Yes	No	No	ECs cultured in physiologically realistic geometry
Shao 2009 [143]	Yes	No	Yes	No	Microfluidic device
Chau 2009 [22]	No	No	No	No	Microfluidic device for simultaneous application of a range of WSS values
Van Doormaal 2009 [44]	No	Yes	No	No	Separates areas of high residence and low shear
Dolan 2011 [43]	No	Yes	No	No	Steady SWSSG
Estrada 2011 [48]	Yes	No	Yes	Yes	System to subject ECs to cyclic stretch and WSS
Srigunapalan 2011 [146]	No	No	No	No	Cells are cultured on a membrane which allows nutrient delivery from below

Wang 2012 [162]	No	No	No	No	Changes flow direction gradually during application

1.1.4.1 Systems for Applying Uniform WSS

Early work on the effects of mechanical forces on ECs focussed solely on the effects of steady WSS. This was frequently achieved using a steady flow of culture medium through a parallel plate flowchamber (PPFC), as shown in figure 1.4. A popular design of flowchamber which is well characterised and has been widely used is the Cytodyne flowchamber (CytoDyne, La Jolla, CA) [53]. This is a simple, reusable device which applies WSS to cells cultured on a standard glass microscope slide. Further studies have produced modified PPFCs which allow novel investigations which could not be achieved using the Cytodyne flowchamber, for example into the effects of WSS on EC monolayer permeability [143; 146] or the simultaneous application of a wide range of WSS values to different monolayers using the same system [22]. Other commercial systems have also been developed which may improve convenience, for example through miniturisation of the flow circuit and the use of disposable flow chambers [129].

Other flow system designs capable of applying steady WSS to cultured cells include the cone and plate viscometer [40] and the EC lined tube [115; 127] as shown in figure 1.4

1.1.4.2 Systems for Applying Simple TWSSG

As discussed in section 1.1.3.2 the WSS experienced by ECs *in vivo* varies throughout the cardiac cycle. This has led to the development of flow systems which apply a

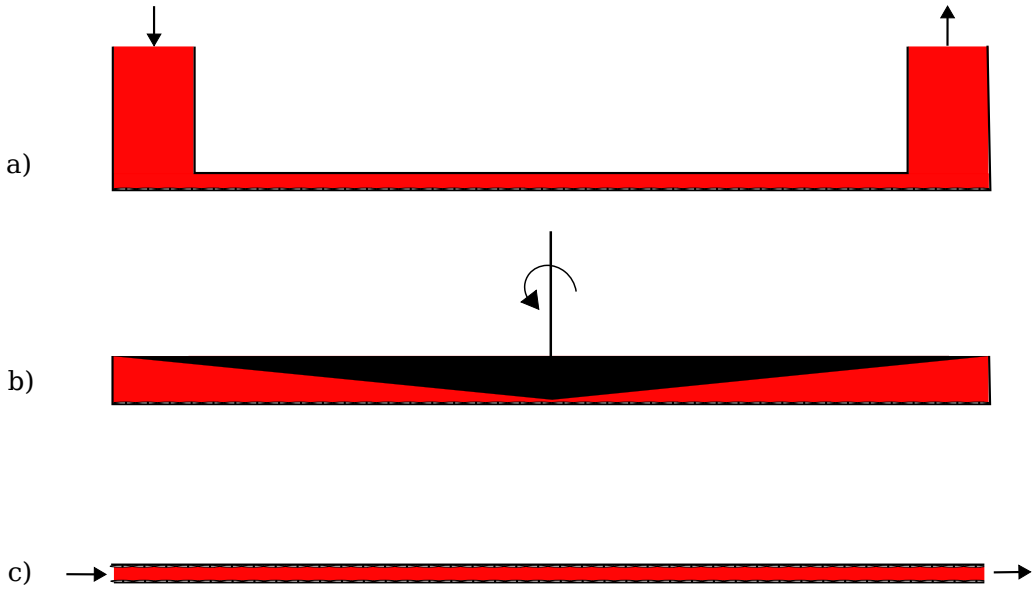

Figure 1.4: Diagram of different designs of flow systems to subject ECs to WSS. Parallel plate flowchamber (a), cone and plate viscometer (b) and EC lined capillary (c)

temporally varying WSS to cultured ECs. For PPFCs and EC lined tubes the WSS is proportional to the flow rate through the chamber. Therefore TWSSG can easily be applied by altering the pump such that it is able to produce pulsatile flow instead of steady flow.

A simple model for applying TWSSG to cultured ECs was developed in the Frangos laboratory. This model applied TWSSG by culturing cells in a PPFC (Cytodyne) and varying the flow rate using a programmable syringe pump [7; 174; 175]. This simple model permits the application of non physiological flow waveforms which either apply high or very low TWSSG. It allowed the investigators to show that TWSSG affects ECs independently of the mean WSS on short time scales. However this model suffers from the limitation that the media is not recirculated, thus limiting its use to

either short term studies or studies in which the mean flow rate is very low. Although short term studies can show in principal that ECs respond differently to different mechanical stimuli it is difficult to predict the response of ECs *in vivo* from results of short term studies as acute and chronic mechanical stimuli on cells may exert different, even opposite, effects [165].

For longer term studies many investigators have used pumps which produce sinusoidal flow waveforms [117; 163] although other waveforms have also been employed [127]. Pulsatile flow setups can vary between those that use a single pulsatile pump, e.g. [127] and those that use a combination of a steady flow pump and a zero displacement pulsatile pump, e.g. [163]. The combination of a steady and pulsatile pump increases the complexity and cost of the system but allows greater flexibility as the pulse amplitude and the mean WSS can be changed independently.

1.1.4.3 Systems for Applying SWSSG

In addition to the temporal variations in WSS caused by changes in blood flow rate over the cardiac cycle the non uniform geometry of arteries can create significant SWSSG. To introduce spatial variations in WSS on a monolayer of cultured cells it is typically necessary to use a flowchamber with a different geometry to those used for steady flow. Some flow system designs which permit the application of SWSSG to cultured ECs are shown schematically in figure 1.5. Many investigators have produced SWSSG by producing a backward facing step in a PPFC ('a' in figure 1.5) [163; 175]. This model produces high SWSSG at approximately physiological levels near the reattachment point. However the SWSSG are highly non uniform and are only applied to the cells at an area of relatively low WSS. Converging flowchambers have been designed to overcome these limitations [43; 157]. These designs apply a uniform SWSSG pro-

portional to the flow rate across a wide range of WSS values, permitting the study of cells exposed to simultaneous high WSS and SWSSG similar to the forces experienced by cells near the apex of a bifurcation.

Very high SWSSG values can be achieved through the use of a 'T' shaped flowchamber [138], although this model also suffers from the limitation that the SWSSG applied are highly non uniform.

A different model for applying physiologically realistic SWSSG was developed by Farcas *et al* [49]. This model cultures ECs on the inside of physiologically realistic silicon casts of arteries, ensuring that the WSS and SWSSG profiles closely resemble those expected *in vivo*.

The models described above have made significant improvements in our understanding of the effects of WSS and WSSG on ECs. However, due to their large size and reagent consumption they are mostly relatively low throughput. A very simple model which applies a combination of WSS, TWSSG and SWSSG, with potentially much higher throughput than the models described above, was described by Dardik *et al* [35]. This model consists of cells cultured in a standard 6 well plate and then placed on an orbital shaker. This causes a wave to travel around the culture dish, applying high, unidirectional WSS near the edges of the plate and low, oscillatory WSS near the middle. Although the WSS waveforms applied using this model are non physiological the WSS applied is at an approximately physiological level, with a unidirectional WSS of approximately 1.1Pa near the edge (similar to in magnitude atheroprotected sites *in vivo*) and an oscillatory WSS of approximately +/- 0.4Pa in the middle of the well (similar to that at atheroprone sites). This model presents a potentially attractive way to study the effects of WSS and WSSG on ECs. However, validation of the results it produces against more physiologically realistic models and *in vivo* results is needed to

improve confidence in its predictions.

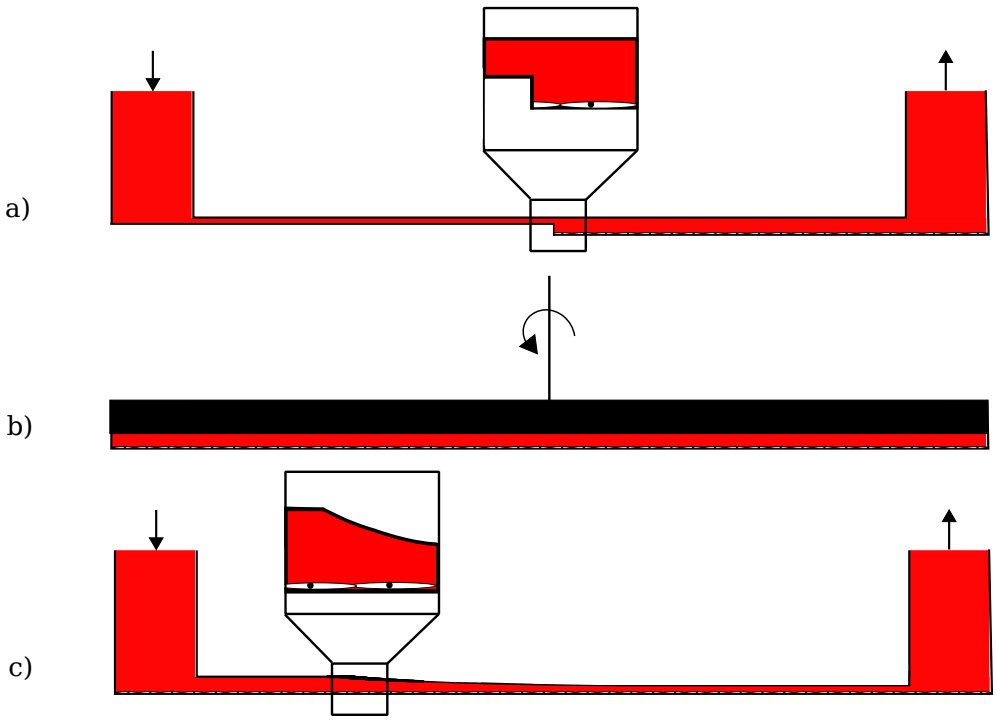

Figure 1.5: Diagram of different designs of bioreactor to subject ECs to SWSSG. Parallel plate flowchamber with backward facing step (a), rotating flat plate (b) and converging flowchamber (c)

1.1.4.4 Systems to Replicate Physiological WSS Profiles

Although appropriately defined sinusoidally varying WSS waveforms are able to approximate mean and the range of WSS values experienced by ECs *in vivo* the TWSSG applied may be up to an order of magnitude lower [125]. This has led to interest in developing flow systems which are capable of applying physiologically realistic WSS waveforms, which mimic both the TWSSG and the degree of WSS reversal expected *in vivo*, to cultured ECs. There has also been interest in further extending these systems

to incorporate additional physical stimuli which EC are subjected to *in vivo*, such as pressure and cyclic stretch.

Many different designs of flow system capable of reproducing physiologically accurate WSS waveforms have been developed, although none have gained widespread use. This section will discuss the various designs used.

The cone and plate viscometer shown in figure 1.4 has been used to subject ECs to steady WSS [40]. Cells are seeded on the plate and the gap between the cone and the plate is filled with culture medium of known viscosity. The cone is then rotated about its central axis, causing the culture medium to flow in a circumferential direction around the device. Providing the Reynolds number (*Re*) is kept sufficiently low this subjects the cells to a uniform WSS proportional to the angular velocity. The standard cone and plate viscometer has been modified by using a computer-controlled stepper motor to drive the rotation of the cone. This allows the user to define any desired rotation (and therefore WSS) profile within the limits of the stepper motor's frequency response, which includes physiologically realistic WSS waveforms [11; 12; 141]. As the velocity of the cone is not constant, start up effects can no longer be ignored when determining the WSS experienced by the cells because the flow velocity is constantly changing and the flow cannot be assumed to be temporally developed. Therefore it is necessary to use CFD analysis to ensure that the cells experience the desired WSS [15].

Whilst the cone and plate viscometer is able to accurately apply physiologically realistic WSS waveforms to cultured ECs it has some limitations. For example it is not possible to study the effects of pulsatile pressure or cyclic stretch using the standard cone and plate viscometer. Whilst the system can be modified to produce SWSSG through the use of a second flat plate in place of the cone [131], these SWSSG are

likely to be fairly low magnitude.

Flow systems for producing flow waveforms proportional to physiological WSS waveforms have also been developed. These systems have the advantage that they are modular in their design, permitting the use of flowchambers with different geometries to vary the mechanical stimulus applied to cells by a given flow waveform. They also have the advantage that the same system can be used for a range of experiments beyond the study of EC response *in vitro*, for example preconditioning of tissue engineered vascular grafts [67] or the culture and mechanical stimulation of *ex vivo* vessels [8; 9; 31; 184].

The complexity, cost, capabilities and accuracy of the different flow systems varies significantly. A simple flow system for the perfusion of *ex vivo* vessels was developed by Conklin *et al* [31]. This system consists of a peristaltic pump to produce a steady flow and a cam-driven pulsatile pump to superimpose the pulsatile component of physiologically realistic flow waveforms on top of the steady flow. This system is very simple, is expected to be relatively cheap to set up and it produces highly repeatable waveforms. However, the accuracy of the reproduction of the flow waveform is compromised if the target waveform requires too high an acceleration and so the cam is slowed down for part of the rotation. This system was designed for the perfusion of *ex vivo* vessels, and results showed that viable vessels could be maintained for at least 24 hrs. Although the flow system was designed for use with ex vivo vessels, it is expected that a similar system could be combined with a PPFC to study the effects of WSS on cultured ECs.

Alternative, more complex systems have been designed [8; 45; 46; 184]. El-Kurdi presented a system capable of precisely and simultaneously regulating the flow/WSS and pressure in *ex vivo* vessels. This system consists of a peristaltic pump to create a

steady flow and a computer-controlled piston and cylinder device to create the pulsatile component of the flow waveform. Several feedback control systems ensured that the WSS and pressure values obtained were close to the user defined target values. A system with similar capabilities was also presented by Bergh *et al* [8], although this system allows less independent variation of the flow and pressure stretch waveforms. These systems are highly capable, although they are highly complex and expected to be relatively expensive to set up.

Most investigators have focused on the effects of WSS and WSSGs on ECs, due to the localisation of atheroma to locations in the vasculature where flow is expected to be disturbed. However there have also been efforts to better mimic the *in vivo* mechanical environment of ECs by subjecting them to both cyclic stretch and WSS. This has typically been achieved by subjecting ECs cultured on a compliant membrane to a known flow and pressure waveform, e.g. [48; 115]. However an alternative design employs a stepper motor controlled cone and plate viscometer to generate the WSS profile and a second stepper motor to directly stretch the elastic substrate on which the cells are cultured [15]. Both of these designs are capable of applying a very wide range of mechanical stimuli to cultured ECs. However the flow, and therefore WSS, is likely to be affected by the motion of the wall in all of these designs. Detailed and careful analysis of the flow characteristics is therefore necessary to quantify the mechanical forces experienced by the cells.

1.1.4.5 The Role of Computational Modelling

Computational modelling has been widely used to elucidate the mechanical environment experienced by ECs *in vivo*. Direct measurement of the mechanical forces produced by *in vitro* bioreactor systems is not typically possible. It is therefore necessary

to use either analytical methods or CFD to quantify the forces that ECs experience within the bioreactor systems. The design of the bioreactor system can have a significant impact on the type of analysis required to achieve this.

Early work subjecting ECs to WSS was typically performed using a PPFC. In this device the WSS is usually calculated analytically, using the following formula to obtain the WSS from the flow rate:

$$\tau = \frac{6\mu Q}{bh^2} \tag{1.2}$$

where μ is the viscosity of the flow medium, Q is the volume flow rate and b and h are respectively the width and height of the flowchamber. This approach obviates the need to use computational modelling. However, it is valid only if the assumptions used when deriving equation 1.2 are appropriate. The assumptions used in this calculation are as follows:

- The fluid must be Newtonian.
- The flow domain is assumed to be two dimensional. Therefore the side walls of the PPFC must have negligible effect.
- The flow must be laminar.
- The flow must be fully developed in both time and space.
- The inlet flow to the parallel plates must be uniform across the width of the chamber.

Taking a popular commercial flowchamber [53] as an example it is possible to test whether or not these assumptions are satisfied for an experiment applying a constant, relatively high physiological WSS of 3Pa.

Culture medium is known to be Newtonian [136]. Therefore the first assumption is satisfied. The assumption of a two dimensional flow domain is clearly not satisfied in the region close to the side wall of the PPFC. However as the width to height ratio in this flowchamber is approximately 80:1 the assumption of a two dimensional flow domain is valid for >90% of the chamber. The flow in a PPFC is typically assumed to be two dimensional as long as its width to height ratio is greater than 10:1.

Laminar flow can be expected if the Reynolds number, *Re*, of a flow is <1000. *Re* can be calculated from the formula:

$$Re = \frac{\rho u l}{\mu} \tag{1.3}$$

Given the flowchamber dimensions of $b = 20mm$ and $h = 0.25mm$ and assuming a fluid viscosity of $\mu = 0.001Pa.s$ one can calculate the required flow rate of $Q = 6.25 \times 10^{-7}m^3/s$ to get a WSS of $3Pa$. This would cause an average flow velocity of $0.125m/s$. Substituting this value into equation 1.3, assuming $\rho = 1000kg/m^3$ and taking h as the characteristic length scale gives $Re = 31.25$. Therefore the assumption of laminar flow is valid even at this relatively high WSS.

For a steady flow start up effects will quickly dissipate, and so the flow can be assumed to be temporally developed after the first few seconds of an experiment. The entrance length, defined as the length of flow required for it to become spatially developed, was calculated for laminar flows between parallel plates by Schlichting [140] as

$$L_e = 0.01h.Re \tag{1.4}$$

The entrance length in this flowchamber when the WSS is $3Pa$ is 0.078mm, which

is a negligible proportion of the overall chamber length. Therefore the flow can be assumed to be spatially developed for almost the entire length of the chamber.

The final assumption is most difficult to justify analytically and for many flowchambers it is likely that it will not be satisfied, although if *Re* is small then it may be justifiable to assume that the effects of a slightly non uniform flow distribution along the inlet width of the flowchamber will dissipate a short distance downstream from the inlet. However, caution is clearly required when assuming a constant flow profile along the width of the inlet and at higher *Re* it is almost certainly not justifiable to make this assumption. In this case CFD or other analysis would be required.

Although under certain circumstances it is possible to determine the shear stress experienced by the majority of the cells in an experiment simply by analytical calculation, more complex flow experiments may require CFD to accurately quantify the mechanical environment. For example if TWSSG are to be applied to cells then the flow cannot be assumed to be temporally developed unless the Womersley number is calculated to be very small (<1). Womersley number (Wm) can be calculated from the following formula:

$$Wm = l\left(\frac{\omega\rho}{\mu}\right)^{1/2} \tag{1.5}$$

Therefore flow systems which produce physiologically realistic flow waveforms, which contain higher frequency components than sinusoidal waveforms with the same dominant frequency, are more likely to require CFD modelling to determine the WSS applied to the cells.

CFD modelling has been successfully applied to flow systems for subjecting ECs to mechanical forces. It has facilitated the study of various mechanical stimuli which

could not be quantified using analytical calculations alone. For example the model employed by White *et al* [175] to study the simultaneous application of SWSSG and TWSSG to ECs required either sudden or ramped onset of flow in a PPFC modified to have a backward facing step. Without the application of CFD modelling it would not have been possible to identify which cells were subjected to SWSSG and which were not. Similar models to this have had considerable success in studying the response of ECs to complex fluid flows [103; 114; 126]. This would not have been possible without the application of CFD modelling.

Another useful application of CFD modelling is to optimise the mechanical environment within a flow system to achieve the best possible reproduction of the desired mechanical environment. For example Breen *et al* employed an iterative approach to improve the reproduction of a desired WSS waveform within a cone and plate viscometer system and van Doormaal *et al* designed a novel helical cell culture device to separate areas of high fluid residence time and low WSS [16; 44]. Both of these applications of CFD extend the range of mechanical stimuli which can be quantifiably applied to cultured EC and thus improve our understanding of EC mechanobiology. Many more examples of CFD being applied to quantify the forces applied to ECs by complex flow conditions exist, e.g. [127; 175].

CFD modelling has achieved considerable success in quantifying the mechanical environments within flow systems. However, it should be noted that caution is required when performing and interpreting CFD simulations as the results obtained have been shown to be operator specific and poorly performed simulations can give highly misleading results [71]. To ensure that results obtained from CFD modelling are accurate it is important to validate the CFD model used, ideally against experimental data [51; 179]. Whilst it is not typically possible to obtain experimental data within flow

systems it is useful to validate the method used against a similar flow condition for which experimental data are available.

1.1.4.6 Flow System Design Considerations

There is a significant body of experimental work studying the effects of mechanical forces on ECs and there is considerable variation in the experimental parameters studied by different investigators [30]. The flow system employed has considerable influence on the range of studies that can be performed. This influence covers the range of mechanical environments that can be studied, the throughput of the experiments, the consumption of potentially expensive reagents and the type of biological responses that can be studied. When designing a flow system it is therefore important to include as much versatility as possible in the design so as to permit the largest possible range of experiments to be performed within it. This may be achieved by using a modular design which allows the *post hoc* incorporation of new features.

It has been argued that microscale systems represent the best way to optimise the design of flow systems for EC biology [185]. Microscale systems consume smaller quantities of reagents than macroscale systems and can achieve potentially higher throughput making them clearly superior for performing experiments which require expensive reagents to be introduced into the circulating medium. However, it should be noted that many of the biological assays in common use today require a relatively large number of cells to function accurately, which may necessitate the use of a macroscale system. Macroscale systems may also partially compensate for their lower throughput by allowing the study of multiple experimental end points. Therefore the choice of the scale of the flow system to employ varies dramatically based on experimental requirements.

1.2 Aim and Objectives

As discussed in section 1.1.3.5 there is a need for further research into the effects of different mechanical parameters on EC response to determine their different and combined effects in atherogenesis. The overall aim of this project is therefore to quantitatively analyse the effects of mechanical forces on ECs, with particular emphasis on studying the effects of different mechanical parameters at physiologically realistic levels.

To achieve the stated aim of the project it will be necessary to provide various enabling technologies and to perform various analyses, as summarised in the objectives below.

The first objective of this project is to develop a versatile flow-bioreactor system (F-BS) which can apply different combinations of the required mechanical parameters, at physiological levels. To enable the required work this system must have the following characteristics:

- The system must be capable of maintaining cells under sterile conditions for sufficiently long that they can reach an approximately steady state response (at least 24 hrs).
- The system must provide an environment which is suitable for maintaining healthy cell cultures.
- The system must be able to independently vary the time-averaged WSS, the TWSSG, the SWSSG and the OSI.
- The fluid mechanical parameters applied to the cells must be quantifiable.

- The system must contain a sufficient population of cells to perform biologically relevant assays. As far as possible, this population must be subjected to an homogeneous mechanical environment.

Quantification of the mechanical environment which cells experience within the bioreactor system is important to ensure that the cells are subjected to physiologically relevant levels of the mechanical stimuli of interest. As it is likely to be impossible or impractical to experimentally determine the flow pattern within the F-BS with sufficient accuracy computational modelling will be required to quantify the forces experienced by cells within the F-BS.

CFD analysis is typically performed using the finite volume method (FVM), using a commercial software package. Alternative methods have also been developed which have some potential advantages over FVM. The lattice Boltzmann method (LBM) is one such alternative. As discussed in section 1.1.3.2 this method is able to perform computations quickly on cartesian meshes, which can be generated with minimal user input. These advantages may make LBM a potentially promising candidate for application in patient-specific CFD models. However, it should be noted that the Cartesian nature of the computational grids used in LBM is a potential disadvantage when compared to FVM as grid refinement can only be performed simultaneously in all spatial directions. It should also be noted that as LBM is less widely used than FVM the method is not as well validated. To determine which method for performing CFD simulations was the optimal choice it is necessary to perform a validation of both LBM and FVM, comparing their results with those obtained experimentally.

The second and third objectives of this project are therefore to validate either FVM or LBM against physically measured flow data and then to analyse the mechanical environment within the bioreator system using the validated method.

To quantitatively determine the response of cells to a given mechanical environment it is necessary to develop methods to quantitatively assess the response of ECs. Specifically, to quantitatively determine the morphology of a monolayer of ECs it is necessary to develop an image processing routine to automatically and accurately extract morphological data from images of the ECs. the fourth objective of this project is to produce an image processing routine capable of automatically extracting morphological data from images of the ECs.

Once these enabling technologies are established the final objective of this project is to assess the response of ECs to various mechanical parameters.

1.2.1 Expected Benefits

The objectives described above can be summarised as follows:

- Develop a versatile F-BS to apply physiologically realistic WSS, T/SWSSG and OSI to cultured ECs.
- Compare CFD results obtained using LBM and FVM with experimental data to determine which method performs best.
- Apply the chosen CFD method to quantify the mechanical environment experienced by cells within the F-BS.
- Develop a method to quantitatively analyse images of cells and determine their morphological features.
- Quantitatively analyse the morphological response of cultured ECs to different fluid mechanical stimuli.

It is anticipated that achievement of the first objective will enable ECs to be subjected to experimental conditions which were not possible using the previously existing flow systems which were described in section 1.1.4.

Achievement of the second and third objectives is likely to significantly improve the confidence with which the mechanical environment in the F-BS can be quantified. In addition to this the comparison between LBM and FVM may help to elucidate the different benefits of the two methods for use in future investigations. This may be particularly important for LBM as it has not yet gained the widespread use enjoyed by FVM.

The fourth objective is expected to deliver a computer programme which is capable of repeatably, automatically and accurately segmenting images of ECs exposed to fluid mechanical stimuli. This programme will be able to generate large amounts of morphological data from images. Further development of this programme could enable its use in quantitatively determining the level of a stain of interest in various images.

Finally, the fifth objective will biologically validate the F-BS developed in the first objective and also further our knowledge about the response of ECs to complex fluid mechanical stimuli.

Chapter 2

Flow system for subjecting ECs to physiological WSS waveforms

2.1 Introduction

As discussed in section 1.1.4 many sophisticated flow systems have previously been developed for subjecting ECs to mechanical forces. However, none of the systems developed to date are able to meet all of the requirements that were set out in section 1.2 as no currently available system is able to combine physiologically realistic TWSSG and SWSSG without further modification. However, many of the systems designed to date could be modified to meet this requirement provided that they were designed in a modular fashion which allowed certain parts to be changed depending on the requirements of the experiments being performed.

For example the cone and plate viscometer has been widely used to apply physiological levels of WSS and TWSSG, to large populations of cultured ECs [16; 34]. The device could be modified to produce SWSSG as well if the cone were replaced

with a rotating disk. This modification would allow a single device to apply either a spatially constant WSS or a WSS varying at a known rate to a monolayer of ECs. Such a modified cone and plate viscometer would therefore meet the requirements set out in section 1.2 and be suitable for use in this project.

Other systems which could be modified to produce physiologically realistic combinations of WSS and SWSSG include the flow systems produced by Bergh, El-Kurdi and Conklin, among others [8; 31; 45; 46]. These systems are all capable of producing physiologically realistic flow waveforms, and they can be used to apply physiological WSS waveforms to cultured ECs when combined with a PPFC [9]. They could also be used to combine physiological TWSSG and SWSSG by coupling them with a flowchamber which has a non-uniform geometry to create SWSSGs. Some examples of such flowchambers include the converging flowchamber [43; 157], the 'T' shaped flowchamber [138], the backward facing step [163] or more complex geometries [49]. These combinations would also be able to meet all of the criteria set out in section 1.2.

The designs which have been identified as potentially suitable for use in this project can be broadly categorised as either a modular F-BS consisting of a flow system for producing physiological WSS waveforms and two or more flowchambers, or a modular rotating cone/disk device. It was decided that a flow system combined with a choice of flowchambers offered a greater degree of flexibility, and potentially lower cost, than a rotating disk/plate system as flowchambers can be designed to apply various different mechanical stimuli and to produce physiologically realistic WSS distributions [49]. Such a system would have the further advantage that it could be adapted for other purposes relating to EC biology, for example the culture of *ex vivo* blood vessels [8] or the mechanical preconditioning of tissue engineered vascular grafts [67]. However, it should be noted that when flow chambers which have complex geometries are em-

ployed it is highly unlikely that an analytical solution describing the characteristics of the flow and WSS expected within the device. CFD is therefore required to determine the mechanical environment which the cells experience.

A wide variety of different flow systems have been established for applying physiological WSS waveforms to cultured ECs or *ex vivo* vessels. For example Bergh *et al* established a system which can be used to subject either cultured ECs in a PPFC [9] or *ex vivo* vessels to physiologically realistic flow and pressure waveforms. This sophisticated system uses a combination of computer controlled pumps and valves to achieve the desired flow and pressure waveforms. This system is highly versatile as its computer-controlled nature allows the user to input almost any physiological flow waveform. However, it should be noted that the high complexity of the system may be a disadvantage as establishing a similar system may be relatively difficult and costly.

El-Kurdi *et al* also established a computer-controlled flow system for producing physiologically realistic flow and pressure waveforms [45; 46]. Although this system has so far only been used for the culture of *ex vivo* vessels it appears that it could be modified for use with cultured ECs. The system uses a peristaltic pump to generate steady flow and a piston and cylinder device connected to a computer-controlled linear motor to generate pulsatile flow. This system has the advantage that it can produce almost any physiological flow and pressure waveform, and waveforms can be produced with higher frequency components than the system produced by Bergh *et al*. However it also has the disadvantage that it is highly complex and is expected to be relatively costly to establish.

A simpler system for subjecting *ex vivo* vessels to physiological flow and pressure waveforms was developed by Conklin *et al* [31]. This system produces the steady component of the flow waveform using a peristaltic pump and a cam driven pulsatile pump

superimposes the pulsatile component on top of this. The amplitude of the pressure waveform can be varied by altering the resistance and capacitance placed downstream from the vessel. Although this system is very simple it can be used to create almost any flow waveform, and the mean pressure and the pulse amplitude of the pressure waveform can be varied without affecting the flow. However, the reproduction of the flow waveforms appears to lose accuracy when there is a large acceleration in the required flow rate. This is likely to be because the cams did not turn at constant angular velocity throughout the cycle. As the flow waveforms are defined by the shape of the cams a new cam has to be machined whenever a different flow waveform is required.

Estrada *et al* also produced a similar model for producing pulsatile flow and pressure waveforms [48]. However, this system used a pneumatically driven chamber to generate pulsatile flow which offers less flexibility than the cam driven pulsatile pump. Although the system produced by Estrada *et al* is able to produce flow and pressure waveforms which appear physiological, comparison was not made with flow or WSS waveforms measured *in vivo*.

The features of the systems mentioned above, along with several other systems developed for studying the biomechanical responses of ECs, are summarized in table 1.1. It appears that the system established by El-Kurdi *et al* offers the best flexibility whilst the system produced by Conklin *et al* is able to offer similar features with considerably reduced complexity. The limitations of the system produced by Conklin *et al* compared to that produced by El-Kurdi *et al* are principally that the accuracy of the waveform reproduction appears to be worse, the frequency response is lower and a new cam has to be machined when a new flow waveform is required. However, the system produced by Conklin *et al* has the advantage that a single cam system and peristaltic pump can have several channels, allowing experiments with different flow conditions to take place at

the same time without duplicating the system. It was also expected that the inclusion of a feedback control system to keep the angular velocity of the camshaft constant throughout the cycle would improve the accuracy of the flow waveform reproduction. The frequency response of the system produced by Conklin *et al* was also thought to be sufficient for studying physiologically relevant flow waveforms. Therefore it was speculated that the limitations of the system produced by Conklin *et al* could either be overcome with slight modifications or would not be significant in this project. It was therefore decided to base the design of the flow system used in this project on that established by Conklin *et al*.

The flow system established by Conklin *et al* was designed for use with *ex vivo* vessels. Further modification is therefore required to make it suitable for applying mechanical stimuli to monolayers of cultured ECs. In particular, flow chambers must be established which apply WSS and/or SWSSG proportional to the flow rate to cells cultured therein. It was decided that a properly designed PPFC would be suitable for subjecting cells to WSS proportional to the flow rate, whilst the converging flowchamber established by Dolan *et al* [43] would be a promising candidate for applying a combination of SWSSG and WSS to cultured ECs. The design and characterisation of these flowchambers will be described in detail in Chapter 4.

2.2 Materials and Methods

2.2.1 Target Flow Waveforms

As discussed in section 2.1 the proposed F-BS is expected to be capable of reproducing any physiologically realistic flow waveform. However, for each flow waveform a

specific cam has to be machined. Therefore, before establishing the system it was important to identify the flow waveforms that would be required. When cells are cultured in a PPFC the flow waveform passed through the PPFC is directly proportional to the WSS waveform experienced by the cells. In non uniform geometries the relationship between flow and WSS is more complex.

Five different WSS waveforms were identified to be applied to cultured cells by the flow system. Three of these were proportional to flow waveforms which had been measured physiologically at different locations in the vasculature [50; 87; 108] whilst the other two were proportional to WSS waveforms obtained at different locations in patient specific CFD modelling of the human carotid artery [34]. The target WSS waveforms are shown in figure 2.1. It should be noted that the flow waveforms required to produce these WSS waveforms are in direct proportion to the WSS waveforms but depend on the dimensions of the flowchamber that the cells are cultured in and the viscosity of the flow medium. A constant K can be defined which relates the WSS experienced by cells in a flowchamber to the flow rate through the flowchamber (for a PPFC, $K = 6\mu/bh^2$, $\tau = KQ$). This constant can be freely chosen, although practical considerations may dictate the optimal value for it to take. These considerations include ensuring that the *Re* within the flow chambers is sufficiently low that the flow is laminar and easily predictable and ensuring that the flow rate is of a magnitude that can be easily and accurately detected by the chosen flow measurement equipment.

2.2.2 Design of Flow Circuit

The F-BS is shown schematically in figure 2.2. The system works by using a peristaltic pump (A) to produce a steady flow. As the flow from a peristaltic pump has a

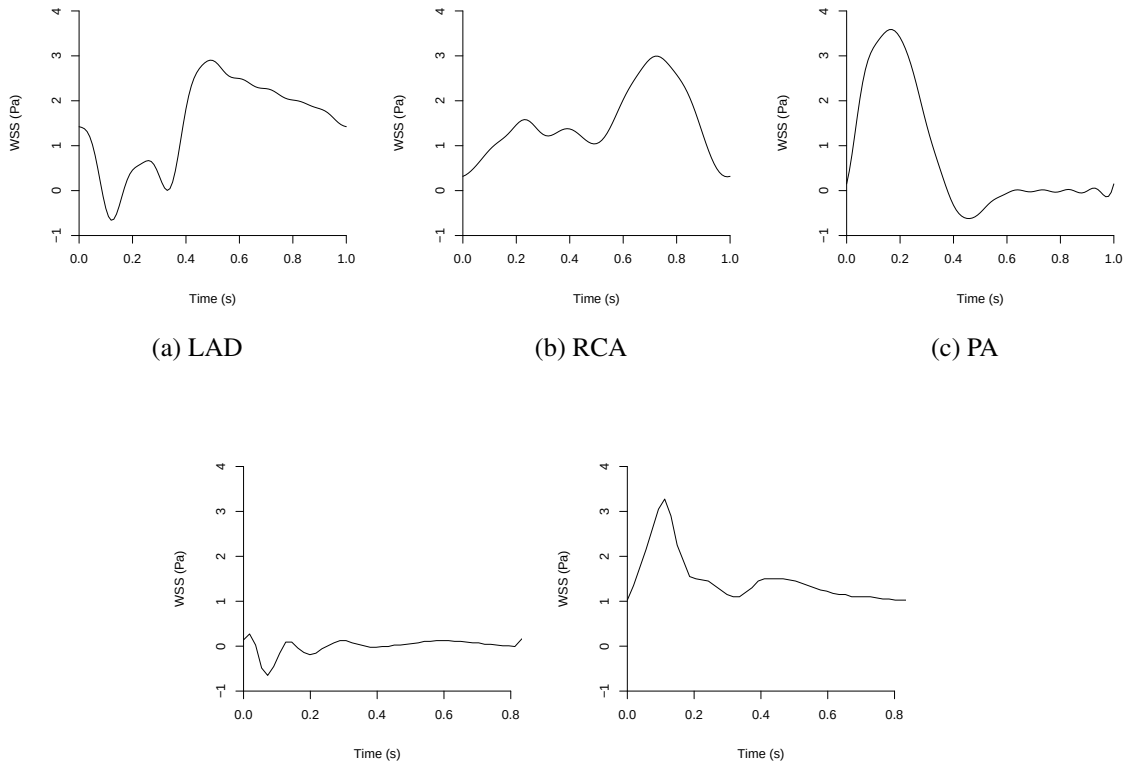

(a) LAD (b) RCA (c) PA

(d) Atheroprone (e) Atheroprotective

Figure 2.1: The five required WSS waveforms

small pulsatile component a compliance chamber (C) is also included to damp away these flow oscillations. The pulsatile component of the desired flow waveform is then superimposed on the steady flow via the cam driven pulsatile pump (B). A one way valve ensures that the pulsatile flow generated by this pump is not damped away by the compliance chamber. Flow medium is drawn from and returned to a reservoir (F) and passes through a test section where the cells are housed (E). If required, the pressure can be modified by changing the resistance provided by the resistance valve to alter the mean pressure and changing the value of the compliance provided by the downstream compliance chamber. If pressure modification is not required then the resistance valve

and downstream compliance chamber need not be included in the flow system. The flow and pressure can be quantified using flow and pressure sensors connected to analogue to digital converters (D). The design and specification of the components will be discussed in detail below.

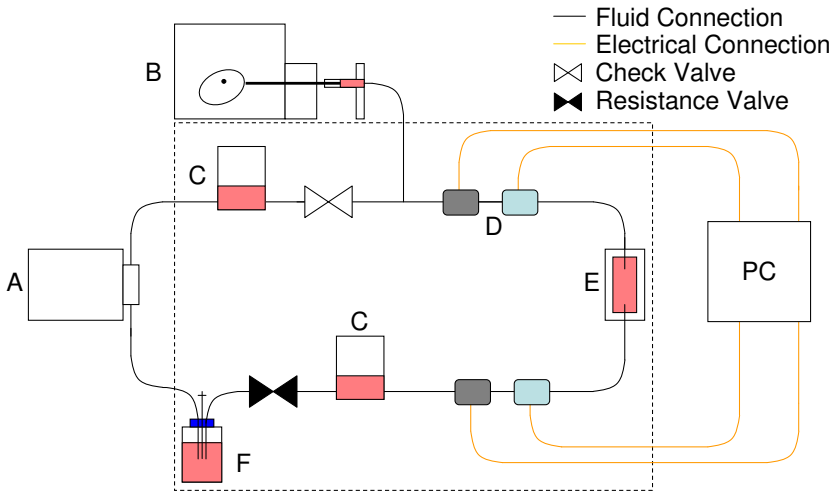

Figure 2.2: Schematic diagram of the entire flow-bioreactor system. Parts enclosed in dotted lines are housed inside the $C0_2$ incubator.

2.2.2.1 Equipment to Measure Flow and Pressure

As discussed in section 2.2.1 the mean flow rate required to produce the target WSS waveforms is dictated by practical considerations including the range of measurement of the flow sensor employed. Therefore it was necessary to specify the flow sensor to be used so that the value of the constant K, and therefore mean flow rate, could be decided before specifying the other components in the flow system.

To be suitable for use in this application the flow sensor needed to be capable of performing the following functions:

- Measure flow whilst maintaining sterility within the flow system.
- Record sufficient points to ensure that the higher frequency components of the flow waveforms produced could be accurately resolved.
- Sufficient resolution and accuracy in the flow measurements to give a confidence interval of $\pm$ 5% in the measured flow values.

The exact flow rate range required could be chosen based on the range of the flow sensor. However, to ensure laminar flow within the flow chamber and to reduce the amount of reagents consumed in each experiment it was considered optimal for the flow rate to be relatively low. Therefore flow sensors which produced good accuracy at the lowest possible flow rates were preferred.

Ultrasonic flow sensors are able to meet the requirements set out above. They have no impact on the sterility of the fluid as they only make contact with the outside of the tubing and they can provide good accuracy in their flow measurements at a sufficiently high frequency to resolve the flow waveforms that the system is designed to produce. Based on the requirements set out above, and economic considerations, a flow sensor was selected (Em-Tec clamp on flow transducer 6.8mm `www.em-tec.com/index.php?topic=produkte&subtopic=emtecProducts`), along with a flow computer for controlling the sensor (SonoTT Flowcomputer or BioProTT). This equipment is able to output 40 flow measurements per second with a resolution of 1ml/min. Although the specified accuracy of the equipment is ($\pm$ 7% + 70ml/min) is not sufficient for our purpose, testing of the equipment showed that in our setup it produced a much better accuracy of $\pm$ 5% for flow rates above 20ml/min, with further improvement observed when higher flow rates were used.

As the resolution of the flow measurements (1ml/min) and the accuracy of the equipment limited the confidence with which low flow rates (<20ml/min) could be measured it was decided that the mean flow values should be higher than 20ml/min to ensure the flow waveforms could be accurately quantified. Therefore it was decided that the constant, K which relates the WSS experienced by cells in a flowchamber to the flow through the flowchamber should have a value of 1/96 Pa/ml/min. This ensures that the flow rate measurements are accurate to within $\pm$ 5% for all WSS values below 0.208Pa.

Quantification of the pressure within the flow circuit was also required. It was vital that the pressure measurement did not compromise sterility. Sufficient frequency and resolution to capture the highest frequency components of the pressure waveform was also required. The pressure required within the system was between 0-200mmHg and the sampling rate for the pressure was required to be at least as high as for the flow. A suitable piezoelectric pressure sensor which measures pressure values in the required range without coming into contact with the fluid was identified (Physiological Pressure Transducer, AD Instruments catalogue no. MLT844). When combined with suitable signal amplification equipment (Bridge Amp, AD Instruments ML221) and an analogue to digital converter (PowerLab 4/25T, AD Instruments catalogue no. ML845) This transducer is capable of outputting pressure values to a PC loaded with suitable software (LabChart 6, AD Instruments) at a user defined measurement frequency of up to 100kHz.

2.2.2.2 Pulsatile Pump

The pulsatile pump is shown in figure 2.3. It consists of four cams attached to a shaft via grub screws. The shaft is connected to a motor (V5253, Rotalink, UK) at one end

and its rotation is constrained in a bearing at the other end. The motor is connected to a proportional-integral-differential (PID) control system which ensures that it maintains a constant angular velocity throughout the cycle (RedDrive 10A, Rotalink, UK). Push rods with carbon-filled PTFE followers are kept in contact with the cam surface using a spring. These push rods are connected to the plungers of syringes whose barrels are held steady. When the motor is turned on and the shaft rotates the syringe plungers are moved in and out of the barrels. The velocities of the plungers, and hence the flow rates out of the syringes, are defined by the shape of the cam and the angular velocity with which the shaft is rotated. The shaft is rotated at 60rpm to give a physiological pulse frequency.

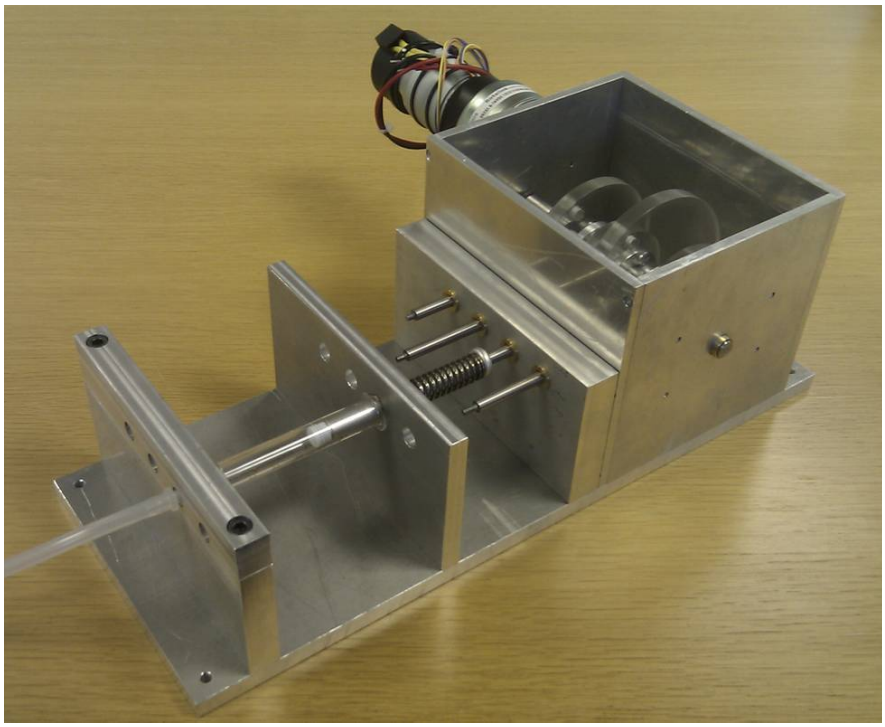

Figure 2.3: Photograph of the pulsatile pump

Cams are designed to produce a specific pulsatile waveform. Given a function $g(t)$

which defines the flow rate in a periodic waveform which has a period of T one can design a cam to produce the pulsatile component of the waveform using the following procedure:

1) Subtract the mean flow rate from $g(t)$ to get the pulsatile component:

$$g_{osc}(t) = g(t) - \frac{\int_0^T g dt}{T} \tag{2.1}$$

2) Determine $u(t)$, the required velocity profile of the syringe plunger based on the cross sectional area of the barrel of the syringe (a) and the oscillatory component of the flow rate

$$u(t) = g_{osc}(t)/a \tag{2.2}$$

3) Integrate $u(t)$ with respect to time to get $x(t)$, the required position of the plunger as a function of time with respect to an arbitrary datum.

$$x(t) = \int u(t) dt \tag{2.3}$$

4) Add a constant value, c to the position values calculated in the previous step.

$$x'(t) = x(t) + c \tag{2.4}$$

6) Define the angle through witch the cam turns on a cycle, $\theta(t)$

$$\theta(t) = 2\pi t \tag{2.5}$$

7) To produce the shape of the cam plot x' against θ in polar coordinates.

To ensure that the cam will work effectively it is necessary to ensure that the maximum pressure angle is below 20 degrees. The pressure angle can be decreased by increasing the value of c. Note that when performing this procedure computationally the waveforms are discretised. Therefore integration is performed numerically rather than analytically. The coordinates found from this procedure can be exported for CNC machining. A sample cam profile and plot of pressure angles is shown in figure 2.4.

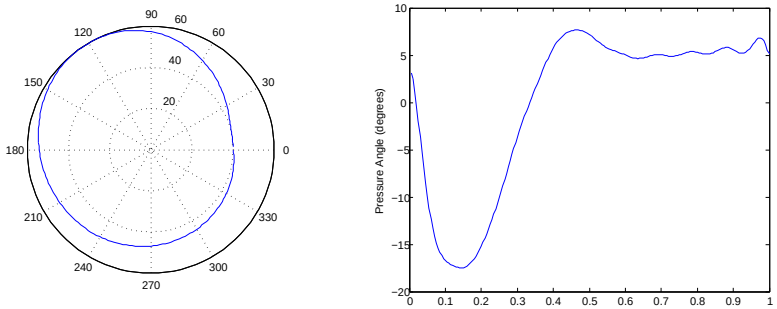

(a) Cam Profile (mm) (b) Pressure Angle

Figure 2.4: Cam profile and plot of pressure angle for the PA flow waveform.

2.2.2.3 Peristaltic Pump and Flow Circuit

As discussed in section 2.2.1, the constant, K which relates the WSS experienced by the cells in the test section to the flow through the test section was selected as 1/96 Pa/ml/min. As the mean WSS is determined by the flow rate produced from the peristaltic pump it was necessary to select a peristaltic pump which was capable of delivering sufficiently high flow rates to impose the highest required mean WSS from the target waveforms, approximately 3Pa, on cells in the test section. This required a flow rate of 288ml/min. It was also thought to be prudent to select a pump which could deliver even higher flow rates so that waveforms with a higher mean WSS could be

studied if future work requires it. We also required the pump to have at least four flow channels which did not come into contact with each other. Combined with the pulsatile pump which can produce four different pulsatile flow waveforms this permits up to four simultaneous experiments to be performed with the same equipment. Different flow patterns can be employed in each of the experiments, with the limitation that the flow waveform must have the same mean value and the pulsatile components must have the same frequency.

The pump selected for use in the flow system was a Masterflex LS 115/230 drive (catalogue no. RZ-07523-80) fitted to a 4 channel, 6 roller pump head (catalogue no. RZ-07535-04) obtained from Cole-Parmer inc. (`www.coleparmer.co.uk`). This pump satisfies the requirement regarding the flow rate and has four channels, with the possibility of adding more at a later date if required.

The tubing and connectors employed required sterilization before each experiment. Autoclaving was selected as the sterilization method of choice as it is reliable and convenient. Therefore the tubing and connectors had to be able to withstand repeated autoclave cycles without emitting any cytotoxic substances. Additionally the tubing was required to have dimensions and acoustic properties suitable for use with the flow sensors. Pharmed tubing with dimensions of 6.4mm external and 3.2mm internal diameter (Fisher Scientific catalogue no. HZ2025902025) was recommended by the manufacturer of the flow sensors as having suitable acoustic properties. It is also suitable for repeated autoclaving and is recommended by its manufacturer for use in cell culture applications. Therefore it was selected for use in the entire flow circuit. PVDF connectors were also obtained from Cole-Parmer.

2.2.2.4 Flowchambers

PPFCs were developed to apply WSS proportional to the flow rate to the cells. Converging flow chambers were also developed to impose SWSSGs. The detailed development of these test sections and the detailed CFD analysis of the mechanical environment that cells experience within them will be discussed in Chapter 4.

2.2.3 Characterisation of Material Properties

As the flow circuit was required to maintain healthy cultured cells the flow medium was culture medium (M199 containing 20% fetal calf serum (BioSera, UK), 30μg/ml endothelial cell growth factor, 30μg/ml Heparin, 2mM L-Glutamine, 100U/ml penicillin and 100μg/ml streptomycin) at 37 degrees C. To determine the WSS experienced in the flowchambers it was necessary to quantify the material properties of the culture medium used in the flow circuit.

Culture medium viscosity at 37^{o}C was determined using a vibro viscometer (A&D Vibro Viscometer SV-1A) and the density of the culture medium was determined by weighing a known volume of culture medium on a high precision balance. To ensure accuracy of the measurements the material properties of water at 20^{o}C were also determined using the same methods and compared with reference values obtained from [17].

2.2.4 Flow Circuit Characterisation

Before their first use the flow sensor and peristaltic pump were both recalibrated to ensure that they produced accurate results. Reference flow rates were calculated by timed collection of a steady flow over at least one minute. The pressure sensor was

also recalibrated, with a reference pressure value calculated from a static column of distilled water. All calibration data points were repeated at least three times.

The flow circuit was then set up as shown in figure 2.2, with the appropriate cam chosen for each waveform and a PPFC used as the flowchamber. The flow rate on the peristaltic pump was set to the desired mean flow rate and the motor for the cam system was set to turn the shaft at 60rpm. Flow data were sent to a PC via an RS232 interface and recorded using Windows Hyperterminal. Pressure waveforms were recorded in LabChart.

Recorded flow waveforms were compared with the target flow waveforms. Quantitative analysis of the disagreement between the measured and target waveforms was performed by calculating the mean squared error (MSE) normalised against the variance of the target waveform, as shown in equation 2.6.

$$MSE = \frac{\sum_{i=1}^{N}(Q_i - \overline{Q_i})^2}{N\sigma_Q^2} \tag{2.6}$$

In equation 2.6 Q_i and $\overline{Q_i}$ are respectively the measured and target flow rate at sampling point i, N is the number of sampling points and σ_Q^2 is the variance of the target flow waveform. This measure is often used to quantify the disagreement between predictions produced by a computational model and true values, e.g. [26]. It defines $MSE = 1$ for an approximation of a pulsatile waveform by a constant value equal to the mean of the waveform. The fit was considered good if MSE was less than 0.1 and excellent if MSE was less than 0.05.

The parameters in the control system were optimised to reduce MSE values and hence improve the agreement between the measured and target flow waveforms.

2.3 Results

2.3.1 Flow Circuit Characterisation

Initially the flow waveforms produced by all of the cams were quantified with the PID controller's default settings. The measured flow waveforms are shown in figure 2.6 along with the target flow waveforms.

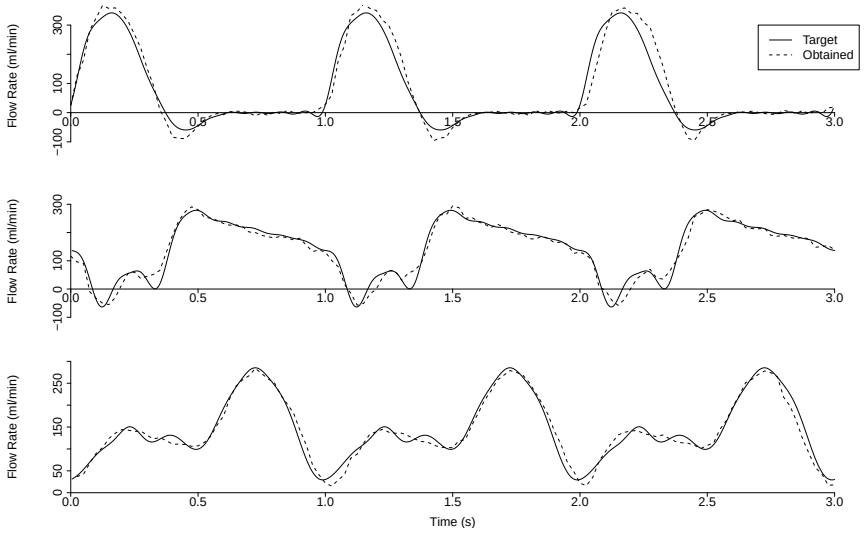

Figure 2.5: Measured vs target flow data for PA (top), LAD (middle) and RCA (bottom) flow waveforms.

The agreement between the target and measured flow waveforms as quantified by equation 2.6 is shown in table 2.1.

Table 2.1: MSE when comparing measured and target flow waveforms

Waveform	RCA	LAD	PA	Atheroprone	Atheroprotective
MSE	0.057	0.043	0.056	0.49	0.12

Minimal improvement was observed upon changing the parameters of the control

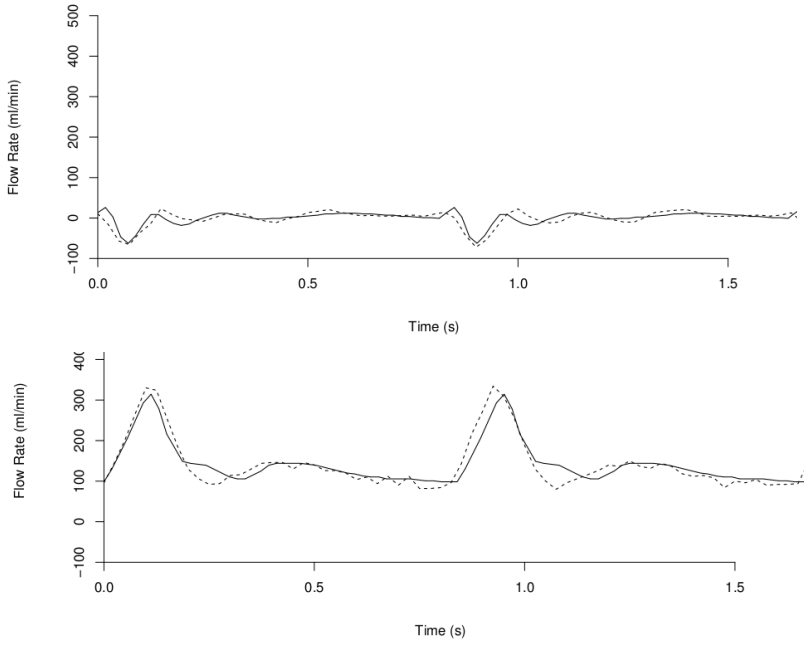

Figure 2.6: Measured vs target flow data for Atheroprotective (top) and Atheroprone (bottom) flow waveforms. Waveforms based on data from [34]

system. However, when the control parameters were set very low or the control system was not used the agreement was observed to be worse for some waveforms, increasing the MSE for the PA waveform from 0.056 to 0.22 for the PA waveform, as shown in figure 2.7. It should be noted that the poorer agreement observed for the atheroprone and atheroprotective waveforms are likely to be due to the higher angular velocity of the cam system when producing these waveforms (72rpm as opposed to 60rpm). Furthermore, errors are exaggerated in the MSE calculation for the atheroprone waveform because of the near zero mean flow and relatively low amplitude.

Although a new cam is typically required if a different flow waveform is to be produced a limited amount of modification of the waveforms is possible without the need to produce new hardware. For example, figure 2.8 shows how the the LAD waveform can be modified to have a higher mean flow rate, simply by increasing the flow rate

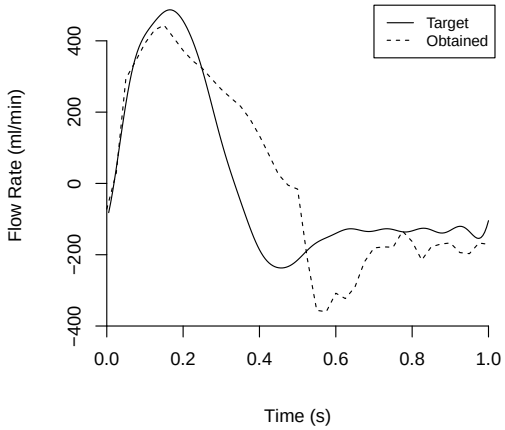

Figure 2.7: Accuracy of the reproduction of the PA waveform without the inclusion of the feedback control system

through the peristaltic pump, or can be scaled down by a factor of 2 by using a syringe with a capacity of 2.5ml rather than 5ml and halving the flow rate through the peristaltic pump.

As well as delivering physiologically realistic flow waveforms the system is also designed to produce pressure waveforms at physiological values. Modification of the pressure waveforms was performed by altering the resistance and compliance downstream from the test section. The mean pressure value is altered by changing the resistance and the amplitude of the pressure pulse is altered by changing the volume of air in the downstream compliance chamber. Figure 2.9 shows the modification of the pressure waveform for three of the flow waveforms described above to either a physiologically normal range of 120/80mmHg, a hypertensive range of 140/100mmHg or a waveform with increased pulse amplitude but normal mean pressure (130/70mmHg). Modification of the pressure waveform was achieved with no observable effect on the

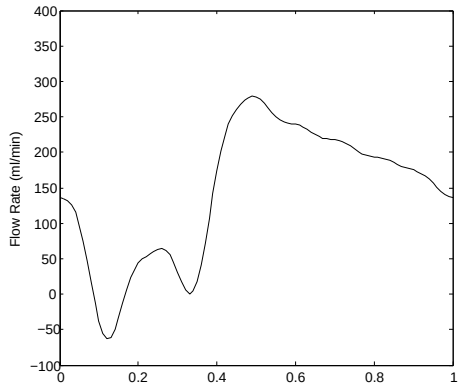

(a) Unmodified LAD waveform

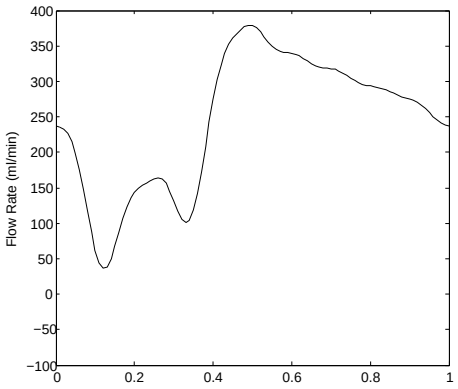

(b) LAD waveform with increased mean flow rate

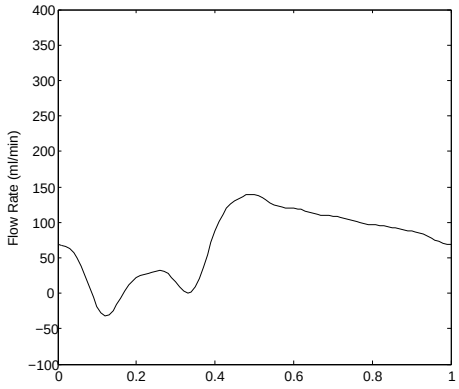

(c) Scaled down LAD waveform

Figure 2.8: Modification of the LAD flow waveform by either reducing the mean flow rate (top) or reducing the size of the syringe in the pulsatile pump (bottom)

flow waveform, as shown in figure 2.10.

2.3.2 Characterisation of Material Properties

The viscosity and density of culture medium at 37 degrees C, determined using respectively a vibro viscometer and a high precision balance are shown in table 2.2. The measured properties of distilled water at 20 degrees C are also shown, along with reference values for these quantities to confirm the accuracy of the equipment.

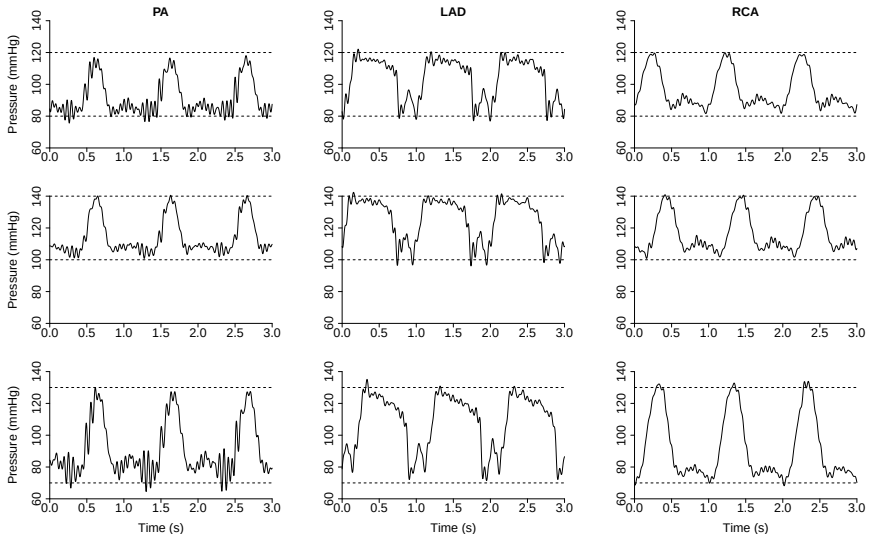

Figure 2.9: Pressure data for three physiological flow waveforms at 120/80mmHg (top), 140/100mmHg (middle) and 130/70mmHg (bottom).

Table 2.2: Viscosity and density of culture medium at 37^o C and distilled water at 20 degrees C. Values presented are the mean of three measurements, and minimal difference was observed between different measurements.

Fluid	Viscosity (mPa.s)	Density (kg/m^3)
Culture Medium	0.735	1030
Distilled Water	1.000	1000
Reference Values for Distilled Water from [17]	1.002	1000

2.4 Discussion

The F-BS was established to produce physiologically realistic flow waveforms which could be accurately monitored. Quantification of the flow waveforms showed that most of the waveforms that were produced showed very good agreement with the physiological target waveforms. However, the system was able to produce better agreement for some waveforms than others. The atheroprone and atheroprotected waveforms produced less good agreement than the PA, LAD and RCA waveforms. The three

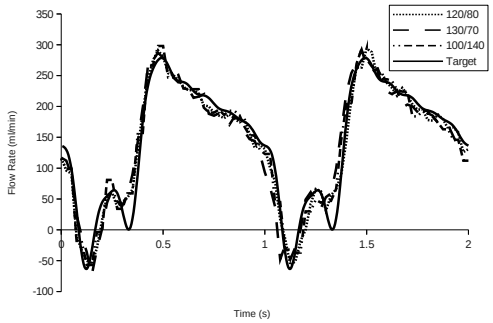

Figure 2.10: Flow data for the LAD waveform obtained at various pressure values.

waveforms which produce less good agreement all appear to have particularly sharp acceleration for part of the cycle. This may result in worsened agreement due to the control system not being able to deliver sufficient power to keep the camshaft turning at constant angular velocity during the sharpest accelerations. It is also possible that the check valve does not function as well for the waveforms with sharp accelerations in their flow rate, allowing some of the pulsatile component of the flow to be damped away by the compliance chamber.

The inclusion of the control system appears to improve agreement for some flow waveforms but not others. This may be because some cams placed a greater load on the motor than others and therefore the motor was able to maintain constant angular velocity without the aid of the control system for the cams which placed relatively low load, but not for those which imposed a higher load.

The agreement between the measured and target flow waveforms compares well with that observed in other studies. The flow results produced by the similar system established by Conklin *et al* appear to be slightly worse than observed here, although it is difficult to make quantitative comparison [31]. This apparent difference is likely

due either to the addition of the control system, differences in the hardware employed in the two systems or differences in the waveforms. Many studies presenting systems for producing physiological flow or WSS waveforms do not show the target waveform along with the measured waveform [8; 48]. However those that do present both the target and measured waveforms typically show agreement similar to that observed for the RCA, LAD and PA waveforms [16; 45; 184].

Good control of the flow environment has been demonstrated using this flow system. The flow waveform was the same when measured upstream and downstream of the test section, suggesting that compliance in the tubing and test section had no significant effect on the flow. However, it is important to note that the WSS waveform experienced by cells cultured within the flow system is a function of the geometry of the test section and the viscosity of the flow medium as well as the flow waveform. Therefore cells must be cultured in suitably designed flow chambers to ensure that they experience the desired mechanical stimuli. As discussed in section 1.1.4 PPFCs have been widely used for subjecting cells to WSS which is related to the flow rate under both pulsatile and steady flow. Typically investigators have assumed that the WSS experienced by the cells is directly proportional to the flow rate through the chamber, although further analysis is required to ensure that this is the case when the flow is pulsatile. However, PPFCs can be designed such that the WSS is proportional to the instantaneous flow rate under pulsatile flow [118; 184]. Therefore a suitably designed PPFC should allow the flow waveforms produced using the flow circuit described here to impose the required WSS waveforms.

Cells cultured in a PPFC experience spatially uniform WSS. If a pulsatile flow waveform with a reversed flow component is passed through the PPFC then the cells will experience a combination of WSS, TWSSG and OSI. However, cells cultured in a

PPFC cannot be exposed to SWSSG. Therefore flowchambers with more complex geometries are required to expose cells to SWSSG. Converging flowchambers have been developed to apply a constant SWSSG to cultured cells [43; 157] by reducing either the height or the width of a PPFC along its length. Combination of a suitably designed converging flowchamber with the flow system described here would, depending on the flow waveform selected, permit the application of a combination of WSS, TWSSG, OSI and SWSSG to cultured cells. The development and characterisation of a PPFC for applying spatially constant WSS proportional to the flow rate and a converging chamber, using a similar design to that produced by Dolan *et al* [43], for applying constant SWSSG to cultured cells will be described in Chapter 3.

A PPFC and a converging flowchamber permit the application of the combinations of WSS, TWSSG, OSI and constant SWSSG required to meet the objectives of this project. They also allow for individual control of the parameters so that their different effects can be studied. However, the flow system could also be combined with other flow chambers which have been presented in the literature to achieve different combinations of mechanical stimuli. For example Farcas *et al* developed a physiologically realistic model of the human right coronary artery lined with ECs for use as a flowchamber in studies of EC response to WSS [49]. Steady flow was passed through this model to study the morphological response to a physiologically realistic spatial (but not temporal) WSS distribution. Combination of this flowchamber with the flow system described here would permit the production of physiologically realistic temporal and spatial distributions of WSS to be applied to cultured ECs. However, the physiological geometry may have similar problems to *in vivo* experiments with the co-localisation of mechanical parameters to areas of disturbed flow. Therefore it was decided that flowchambers with simpler geometries were a better choice for this

project.

The flow system is capable of producing flow waveforms at different physiologically realistic pressure values, without affecting the flow waveform. Therefore the effects of cyclic stretch, in combination with other mechanical parameters, could be studied by combining the flow system with a flowchamber which cultures cells on a substrate which deforms with applied pressure, e.g. [48; 115; 127].

Several flow systems with similar capabilities to the one described here have been developed for studying the response of *ex vivo* vessels to mechanical forces [8; 31; 45]. *Ex vivo* vessels have the advantage that they retain the morphology of the entire vessel and can therefore show effects of cross-talk between the different cell types which are present *in vivo*. The flow system developed here could also be fairly easily adapted for this purpose if future experiments required it.

A limitation of the flow system compared to others that use computer-controlled hardware to produce user defined waveforms (e.g. [8; 45; 184]) is that if a new waveform is required then a new cam has to be machined. However, the machining of new cams can be fairly easily done in-house. Some modification of the flow waveforms is possible without producing new cams, as shown in figure 2.8. The pulsatile component of the waveform can be scaled by selecting a syringe which has a different cross sectional area and the mean flow rate can be modified to any flow rate that the peristaltic pump can produce. These modifications can have the effect of changing the TWSSG, mean WSS or OSI, potentially whilst keeping other parameters the same.

The waveforms chosen to be produced by the flow system include two which are derived from patient specific CFD modelling of the human carotid artery. These waveforms are obtained at a locations which are either prone or resistant to atherosclerosis and they have been shown to cause clear phenotypic differences in cultured ECs

subjected to both of them for 24 hrs [34]. The other waveforms are proportional to flow waveforms measured physiologically in different atheroprone arteries in humans [50; 87; 108]. Although the WSS experienced by cells in these arteries may not be directly proportional to the flow waveform throughout the artery, CFD modelling of similar flow waveforms in model bypass grafts showed that the WSS waveforms were approximately proportional to the flow waveforms at locations where the geometry was relatively uniform [179; 180; 181]. WSS waveforms at other locations can be approximated by changing either the mean flow rate, the pulse amplitude or both and hence can be obtained without the need to manufacture a new cam.

Chapter 3

Computational Fluid Dynamics - Theory and Validation

3.1 Introduction

Computational fluid dynamics (CFD) has been used widely to quantify fluid mechanical parameters in situations where it is impossible or impractical to determine the parameters of interest using experimental or analytical methods, including the flow of blood in arteries [85] and culture medium in flow experiments [127]. CFD is required in this project to determine the shear stress applied to the cells cultured in the different flowchambers.

Although CFD is an extremely powerful tool for quantifying fluid mechanical parameters it should be noted that it is often impossible to compare the results of CFD analysis against experimental data. Therefore validation of the results of CFD analysis is often not performed and it is necessary to use caution when interpreting its results under these circumstances. It has been shown that the results of CFD analy-

sis for a given flow condition can be highly operator specific, with some investigators producing results which show very little agreement with the experimental data in a multilaboratory benchmark study [71]. Little correlation was observed between the self ascribed experience of the investigator and the agreement between experimental and computational results. This study highlights the importance of validation in CFD analysis.

Various different methods have been developed for CFD analysis. The most popular methods are the finite volume/finite element methods (FVM/FEM) which provide a procedure for numerically solving the Navier-Stokes (N-S) equations which govern fluid flow [160].

The lattice Boltzmann method (LBM) has also recently gained popularity. This method is reported to be suitable for simulating complex flows, e.g. biological flows [73; 124; 151], flows in porous media [65] and flows incorporating complex physical phenomena such as Magnetohydrodynamics [39]. It is based on molecular dynamics as described by the Boltzmann equation with the phase space discretised from a continuum to a lattice.

Although FEM/FVM are well established for performing CFD simulations and have been widely validated LBM has some potential advantages over them. The most important advantage when studying biological flows is that the mesh is an entirely Cartesian grid, which requires minimal user input is required to define. This advantage may be particularly significant in the development of patient-specific blood flow models to plan cardiovascular interventions [113]. Other potential advantages of LBM include its excellent parallel efficiency [150] and the existence of a good open-source implementation [96]. However it should be noted that LBM is an emerging technology and relatively few comparisons between the accuracy of the results of LBM and

FEM/FVM. Therefore it was decided that comparison should be made between the results obtained using LBM and those obtained using FVM for a case in which experimental data were available. The test case chosen for this comparison was the ventricular assist device used in the study of CFD results obtained in multiple laboratories performed by Hariharan *et al* [71]. The geometry used in this study is a simple nozzle-expansion model, as shown in figure 3.1. The same geometry used by Hariharan *et al* [71] was used to compare the results of LBM and FVM.

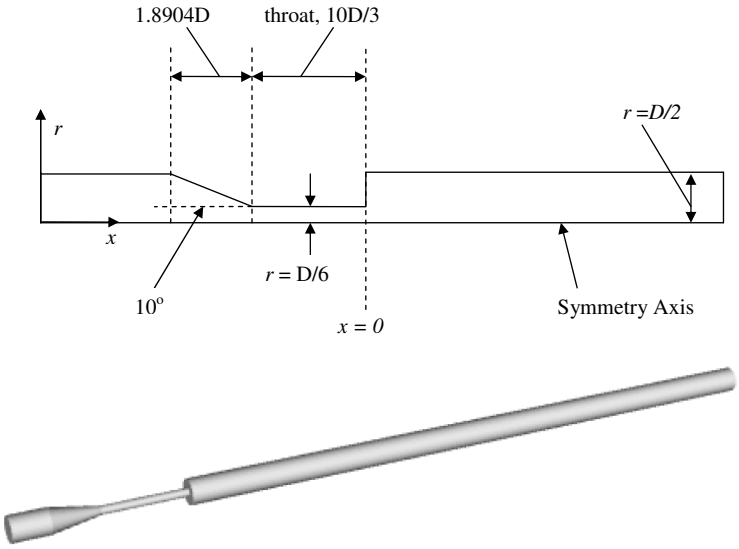

Figure 3.1: Geometry in which simulations were performed (Not to scale). The outlet is kept sufficiently long so that when the flow leaves the domain it is fully developed. The location at the expansion ($x = 0$) is used as reference point for the discussion of results.

Experimental particle image velocimetry (PIV) data are openly available for a range of *Re* from 500 to 6500, based on the average velocity and diameter in the throat of the device (`http://fdacfd.nci.nih.gov`). As the flow is expected to be laminar in our flowchambers it was decided that the comparison should be performed for a laminar flow. Therefore the data at *Re* = 500 were employed as the benchmark

for the flow simulations.

The geometry shown in figure 3.1 was chosen for a number of reasons. Firstly, it is simple and axisymmetrical but challenging to model due to the sudden expansion. Secondly, and more importantly, it is a benchmark flow model employed in the US Food and Drug Administration (FDA) Critical Path Initiative project [71] to determine the applicability and limits of current CFD simulations in evaluating medical devices, i.e. to better study the interaction of flowing fluids with medical devices, an area in which the application of LBM has already been reported [124; 151] and which is expected to become increasingly popular and important. Therefore it is appropriate that LBM is tested using this benchmark flow model. The diameter ratio between the throat and the expansion is 1:3, causing an approximately nine fold increase in velocity from the inlet to the end of the throat.

3.2 Methods

3.2.1 Lattice Boltzmann Method

3.2.1.1 The Boltzmann Equation

The Boltzmann equation was developed by Ludwig Boltzmann in 1872 [13]. It can be expressed in the following form:

$$\frac{\partial f}{\partial t} + \frac{\mathbf{p}}{m} \cdot \nabla f + \mathbf{F} \cdot \frac{\partial f}{\partial \mathbf{p}} = \left(\frac{\partial f}{\partial t} \right)_{collisions} \tag{3.1}$$

The equation describes the statistical molecular dynamics of a fluid based on the probability distribution function $f(x, t, u)$ which describes the probability of finding a particle at location x and time t with velocity u. The terms on the left represent the

free streaming of the particles in the absence of intermolecular collisions and the term on the right accounts for the effects of intermolecular collisions.

Macroscopic variables such as instantaneous velocity can be derived from the function f by integrating to find the statistical mean of the particle velocities at time t and location x. However, as the equation describes a continuum of velocity, time and position values it is rarely possible to find solutions to the equation.

3.2.1.2 Discretization

LBM is based on a discretised Boltzmann equation, in which the velocity, position and time spaces are discretised so that only certain velocity, position and time values are allowed. The position values are chosen such that the probability distribution function f is defined only at regularly spaced intervals in all spatial dimensions. These positions are defined as the nodes on which the simulation is performed. The shortest distance between adjacent nodes is then defined as one spatial lattice unit. Time is also discretised such that only integer time values are permitted in lattice units. Allowed velocity vectors are typically chosen such that a particle on a node at integer time would either move either exactly one or exactly zero lattice units in each spatial direction in one time step, although models have been developed which allow particles to travel further [28]. Therefore the chosen velocity values form connections between lattice nodes.

In a three dimensional geometry, with the only allowed velocity in each lattice direction equal to one or zero there are 27 possible velocity vectors, with total lengths of either zero, one, $\sqrt{2}$ or $\sqrt{3}$. These sets of vectors are shown graphically in figure 3.2, along with the Miller indices that describe the vectors.

To improve computational efficiency it is necessary to use as few velocity vectors as possible to recreate the desired macroscopic physics. Therefore several different

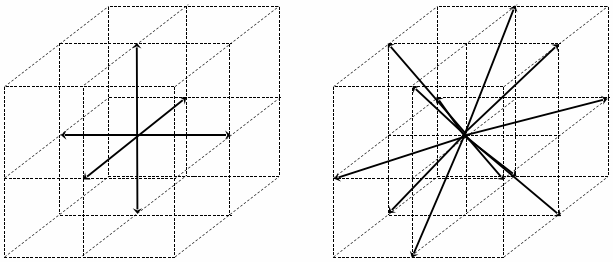

(a) $\langle 100 \rangle$ (b) $\langle 110 \rangle$

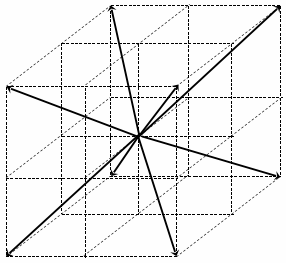

(c) $\langle 111 \rangle$

Figure 3.2: Sets of velocity vectors described by different Miller indices

lattices have been developed which contain different numbers of connections between nodes. Lattices are typically described by the DnQm convention. In this convention n indicates the number of dimensions and m the number of discrete velocities present on each node. For studying three dimensional flows the most popular lattices are D3Q15, D3Q19 and D3Q27. These lattices can be described by the combinations of Miller indices that are present for each of them and the weight of the connection allocated to each velocity vector, as shown in table 3.1.

It should be noted that the lattices are only invariant with certain rotations about their axis. However, to properly model a continuum fluid their properties must not change with any arbitrary rotation. Therefore the tensors derived from moments of the distribution function which give the values of the macroscopic variables density,

Table 3.1: Weights of velocity vectors present on different lattices

Miller Index	Length	D3Q15	D3Q19	D3Q27
[000]	0	2/9	1/3	8/27
$\langle 100 \rangle$	1	1/9	1/18	2/27
$\langle 110 \rangle$	$\sqrt{2}$	0	1/36	1/54
$\langle 111 \rangle$	$\sqrt{3}$	1/72	0	1/216

ρ, velocity $\mathbf{u}$ and momentum flux $\mathbf{\Pi}$ as shown by equations 3.2 - 3.4 must be fully isotropic.

$$\mathbf{M}_1 = \rho = \sum_{i=1}^{n} f_i \tag{3.2}$$

$$\mathbf{M}_2 = \mathbf{u} = \sum_{i=1}^{n} f_i e_i \tag{3.3}$$

$$\mathbf{M}_3 = \mathbf{\Pi} = \sum_{i=1}^{n} f_i e_i e_i \tag{3.4}$$

Whilst all of the lattices used to date are believed to be fully isotropic it should be noted that there have been observations of qualitatively incorrect results in which unphysical artefacts were observed [72; 109]. Therefore the results we obtained were compared with the experimental data on several planes to ensure that the results were accurate throughout the domain.

3.2.1.3 Numerical Method

LBM was originally proposed as an improvement to lattice gas cellular automata (LGCA) [79; 110]. However it has been shown that the NS equations can be derived directly from the LB equation (LBE) [128] and the LBE can be obtained directly from the Boltzmann equation [75].

The LBE is frequently expressed in the following form:

$$f_i\left(x+\mathbf{e}_i dt, t+dt\right) dxdp - f_i(x,t) dxd\rho = \frac{\partial f_i(x,t)}{\partial t}_{collision} dxd\rho dt \tag{3.5}$$

Similarly to the continuous equation, the terms on the left represent the free streaming of the particles and the term on the right accounts for intermolecular collisions. A collision operator which has become popular due to its simplicity and efficiency is the Bhatnager, Gross, Krook (BGK) collision operator [10; 23]. At each time step this operator simply relaxes all of the particle populations at a uniform rate towards a local equilibrium distribution function found from the local density and velocity by the equation:

$$f_i^{eq} = \rho\omega_i\left(1+\frac{\mathbf{e}_i.\mathbf{u}}{c_s^2}+\frac{(\mathbf{e}_i.\mathbf{u})^2}{2c_s^4}+\frac{\mathbf{u}.\mathbf{u}}{2c_s^2}\right) \tag{3.6}$$

where the vectors $\mathbf{e}_i$ and $\mathbf{u}$ represent respectively the velocity components in each direction and the local velocity vector. c_s^2 represents the speed of sound in lattice units which is typically $1/\sqrt{3}$. BGK can be regarded as a single relaxation time collision operator. Variations on this collision operator which simulate fully incompressible flows [74] or improve the numerical stability compared to the standard BGK model [95] have

been reported. Multiple relaxation time (MRT) models have also been reported to significantly improve numerical stability and potentially reduce computational effort by allowing simulations to be performed on much smaller grids [42].

3.2.1.4 Simulation Setup

The LBM simulations in this study employ the open source software library Palabos (`http://www.lbmethod.org/palabos`). Palabos is written in C++ and implements various LB models. It is capable of running either in serial or in parallel. The 3D geometries were read from stl files created using SoildWorks (SolidWorks Corp. Concord, MA, USA). A voxelization process was then implemented using the open source C++ library CVMLCPP (`http://tech.unige.ch/cvmlcpp/`). This produced a lattice with only fluid and solid nodes. It should be noted that no smoothing of the edges was implemented. This was acceptable as a highly accurate solution near the boundaries was not necessary in this validation study.

As LBM is based on molecular dynamics it is essential to ensure that *Kn* is sufficiently low that the flow can be considered a continuum. *Kn* was calculated using the following equation [155]:

$$Kn = \frac{l_m}{H} = \frac{\nu}{c_s H} \tag{3.7}$$

where l_m is the molecular mean free path, H is the shortest length scale, taken in this case to be the diameter of the throat in lattice units, ν is the kinematic viscosity and c_s is the speed of sound. *Kn* was below 0.0005 in all simulations.

Simulations were performed either in serial or parallel on the Iceberg supercomputer at the University of Sheffield on 64 bit AMD processor cores. In all simulations a Dirichlet boundary for velocity was imposed at the inlet applying a constant fully de-

veloped parabolic velocity profile. At the outlet a zero gradient condition was applied on all particle populations. All solid nodes applied a bounce back boundary condition.

The simulations comparing the effect of grid density and those at $Re \leq 250$ used the BGK collision operator as it has been shown to be extremely efficient [23]. The results comparing different lattices at $Re = 500$ were obtained using the regularized BGK collision operator as it improves numerical stability with a minimal effect on computation time [95]. The final results with either collision operator when other variables were kept constant were observed to be in close agreement as discussed in section 3.3.3.4.

LBM has been shown to be second order accurate for velocity and shear stress fields [92], although it is possible that in this 3D study on a complex domain at fairly high *Re* the computational cost of performing calculations on a grid with sufficient resolution to achieve second order accuracy may be too high. Mesh independence tests were therefore performed to quantify the errors introduced by the spatial discretisation. Temporal convergence tests were also performed and simulations were run until a steady state was reached.

3.2.2 The Finite Volume Method

The N-S equations are a set of paired, nonlinear, second order partial differential equations. The N-S equation and the continuity equation, which describe respectively the conservation of momentum and the conservation of mass for a fluid are shown below.

$$\rho\left(\frac{\partial \mathbf{u}}{\partial t} + \mathbf{u}\cdot\nabla\mathbf{u}\right) = -\frac{\nabla p}{\rho} + \nu\nabla^2\mathbf{u} + \mathbf{F} \tag{3.8}$$

$$\frac{\partial \rho}{\partial t} + \nabla \cdot \rho \mathbf{u} = 0 \tag{3.9}$$

It is possible to obtain analytical solutions to these equations under certain of limiting assumptions. However, for the vast majority of real flow conditions it is not possible to solve the equations analytically. Therefore numerical methods are required to obtain an approximate solution to the equations. FVM has gained widespread use for this purpose because of its accuracy and versatility. There are three main steps in the computation of a the FVM solution to a given flow problem:

- Discretisation of the flow domain into control volumes (alternatively called elements or cells).
- Integration of the governing equations over all control volumes to transform the set of differential equations to algebraic equations.
- Iteration to solve the resulting set of algebraic equations.

3.2.2.1 Discretisation

The discretisation process involves defining a number of control volumes which fill the entire flow volume, with adjacent control volumes sharing at least one face. The control volumes next to the flow boundaries have at least one face which lies on the boundary. Within each control volume there is one node at which macroscopic variables are defined.

3.2.2.2 Integration

Once the flow domain is discretised and the faces shared between adjacent cells are defined the governing equations shown in equations 3.8 and 3.9 are integrated over the control volume, as shown below:

$$\int_{CV} \frac{\partial(\rho \mathbf{u})}{\partial t} dV + \int_A \mathbf{n} \cdot (\rho \mathbf{u}\mathbf{u}) dA = \int_A \mathbf{n} \cdot (\mu \nabla \mathbf{u}) dA + \int_{CV} \mathbf{F} dV \tag{3.10}$$

$$\int_{CV} \frac{\partial \rho}{\partial t} dV + \int_A \mathbf{n} \cdot (\rho \mathbf{u}) dA = 0 \tag{3.11}$$

where CV is the control volume, A is the surface of the control volume and $\mathbf{n}$ is a vector in the direction normal to the surface A.

Discretisation of these equations over time and space yields a set of algebraic equations describing the transport of mass and momentum through the control volume at each time step in terms of the balance of the mass and momentum fluxes at the faces of the control volume.

These equations are then solved by iteration, with a convergence criterion selected to ensure that the results do not change when more iterations are performed. As the pressure gradient is unknown and cannot be derived from equations 3.10-3.11 a method for pressure-velocity coupling is required. The SIMPLE algorithm [121] was used for this purpose.

3.2.2.3 Simulation Setup

The simulations were performed using the finite volume solver Fluent 13 (Ansys inc., Canonsburg, PA, USA) using a pressure based Navier-Stokes solver. Second order schemes were used for the discretisation of both pressure and momentum. This made the scheme numerically second order accurate in space.

The domain was discretised using the mesh generator in Ansys Workbench 13 using the CutCell algorithm with uniform edge spacing throughout the domain. This algorithm results in a mesh which has a high proportion of regular hexahedral cells. Mesh refinement studies were performed by comparing results obtained using meshes with average cell edge sizes ranging from 0.27 - 1.7 mm and examining the convergence behaviour of the results.

Although the flow was steady it was expected that during the development of the flow there may be some time dependent features. Therefore the flow was modelled as an unsteady flow with time steps lasting 0.01s. Sufficient time steps were calculated to ensure that the steady state solution had been reached. Solutions for each time step were considered converged when the normalised, scaled residuals for continuity and all three velocity components had fallen to below 10^{-4}.

The fluid properties were modelled as those of water at room temperature, with $\rho = 1000kg/m^3$ and $\mu = 0.001Pa.s$ and the average inlet velocity was $0.0139m/s$, and the diameter of the pipe was 0.012m (0.004m in the throat), resulting in a Reynolds number of 500 in the throat section, the same as that used in the PIV experiments.

3.2.3 Quantification of Axisymmetry

A quantitative measure of the axisymmetry of the results was introduced to ensure that the observed results were consistent throughout the domain. This measure examines the level of disagreement between axial velocity profiles along different lines which passed through the central axis of the flow at the same location but which were rotated through 45 degrees relative to each other. It defines the disagreement through the following equation:

$$\epsilon = 100 \times \frac{\sum_{i=0}^{D} |u_1 - u_2|}{0.5 \sum_{i=0}^{D} (u_1 + u_2)} \tag{3.12}$$

where ϵ is a measure of the asymmetry and u_1 and u_2 are the velocity profiles along two lines at equivalent axial positions but rotated through $45°$. As computational nodes were not at the same locations along the two lines, linear interpolation and extrapolation was performed to obtain u_2 with nodes located at the same distance from the centreline as u_1. When performing the extrapolation values of zero were imposed on any solid nodes. Clearly for an axisymmetrical flow ϵ will be equal to zero.

3.3 Results

3.3.1 Spatial Convergence

For the simulations using both LBM and FVM it was necessary to ensure that the results obtained were independent of both the grid density and the simulation time. For the FVM simulations it was further necessary to ensure that the results did not depend on the number of iterations performed. To examine the convergence of the results, changes in the maximum observed velocity along the centreline as a function of the

grid density were plotted for both LBM, using a D3Q19 lattice, and FVM, as shown in figures 3.3 and 3.4. LBM using a D3Q27 lattice showed similar spatial convergence to D3Q19, with changes of less than 1.5% observed between the D3Q27 grids having the same number of cells as the two finest D3Q19 grids shown in figure 3.3. Therefore, the second finest grid was used for LBM simulations on both the D3Q19 and D3Q27 lattices (unless otherwise stated).

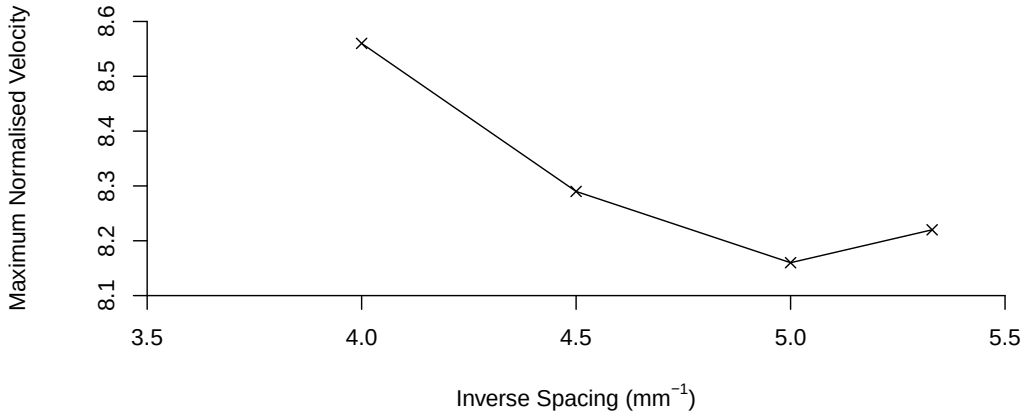

Figure 3.3: Maximum velocity observed in LBM simulations of flow in nozzle-expansion model using different grid densities. Velocity values are normalised against the average inlet velocity

Figures 3.3 and 3.4 show that changes in maximum velocity introduced by increasing mesh density were very small for both LBM and FVM. It should be noted that the range of grid densities studied for LBM is smaller than that for FVM. This was because LBM produced numerically unstable results at lower grid densities.

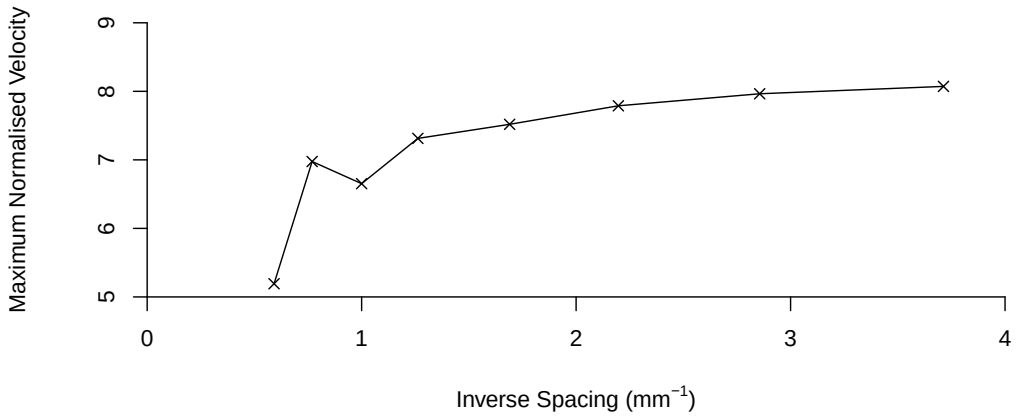

Figure 3.4: Maximum velocity observed in FVM simulations of flow in nozzle-expansion model using different grid densities. Velocity values are normalised against the average inlet velocity

3.3.2 Comparisons Between Computational Predictions and Experimental Data

To examine the accuracy of the predictions made by the two schemes the computed velocity fields were compared with those obtained experimentally [71]. Figure 3.5 shows the normalised velocity along the centreline of the flow domain obtained using LBM and FVM along with PIV data showing experimental measurements of the fluid velocity along the centreline from three independent laboratories. Excellent agreement is observed between the predicted and experimental velocities for FVM and LBM using the D3Q19 lattice. However, the centreline velocity is slightly overestimated by the D3Q27 lattice.

Figures 3.6-3.7 show the velocity profiles along a line which is perpendicular to the centreline that passes through the centreline at $x = 5d$ downstream from the expansion

obtained using FVM and LBM, along with the experimental velocity measurements along the same line. From these figures it appears that only FVM has faithfully reproduced the experimental data. The LBM simulation using D3Q19 shows a clear lack of axisymmetry, whilst the LBM simulation using D3Q27 overestimates the centreline velocity by approximately 10%.

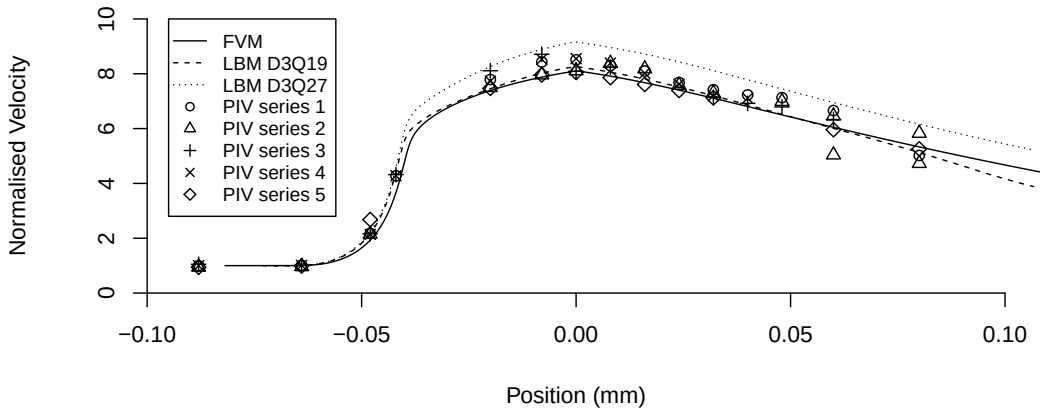

Figure 3.5: Velocity profiles along the centreline of the nozzle flow domain using FVM and LBM computational schemes and PIV data points from three independent flow laboratories.

3.3.3 Axisymmetry

The experimental data showed axisymmetrical results. It was therefore important to ensure that the results produced by the simulations were also axisymmetrical. To test the axisymmetry of the results axial velocity plots were produced on lines which were perpendicular to the centerline and which passed through the centreline at the same location, but which were rotated through 45^o with respect to each other for both com-

putational schemes. In terms of Miller indices, these lines were parallel to either the [010] or [011] vectors.

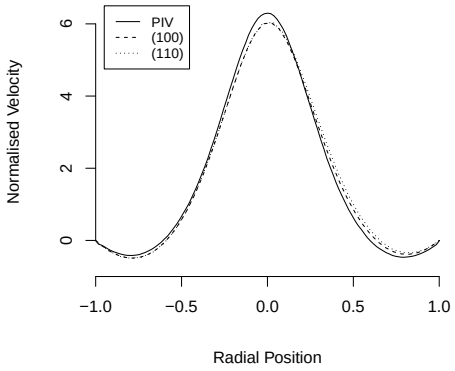

Figure 3.6: Graph of axial velocity on the (010) plane and the (011) plane obtained using FVM along with sample PIV data, $x = +5D$, emphRe = 500

As shown in figure 3.6 the results produced by FVM are axisymmetrical. However, the results produced by LBM show clear differences between lines at 45 degrees to each other and are therefore not axisymmetrical, as shown in figure 3.8. This result was not expected for a flow in an axisymmetrical domain and shows clear disagreement with the experimental flow data. Therefore it appears likely that these results do not represent a physical effect but instead show an error in the model. As the geometry is axisymmetrical and the effects of gravity were ignored there is no physical reason why the results should not be axisymmetrical. Therefore it appears that rotational invariance has been lost in the LBM simulations. This was an unexpected result. Therefore further simulations were performed to investigate the reason for the loss of rotational invariance.

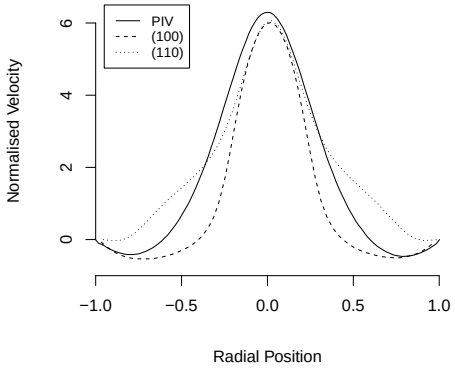

Figure 3.7: Graph of axial velocity on the (010) plane and the (011) plane obtained using LBM on the D3Q19 along with sample PIV data, $x = +5D$, emphRe = 500

3.3.3.1 Effect of Lattice Model

The unphysical results observed using LBM were obtained using the D3Q19 lattice model. It was hypothesised that the use of other lattice models might improve the observed results and recover the apparently lost rotational invariance. Therefore simulations were performed using the D3Q15 and D3Q27 lattices and similar tests for axisymmetry were performed. Unfortunately the simulation using the D3Q15 lattice was numerically unstable and did not produce meaningful results. Previous investigations have shown that the D3Q15 lattice produces poorer stability than the D3Q15 lattice [112]. However, stable results were obtained using the D3Q15 lattice at a lower *Re* of 250. Figures 3.9 and 3.10 show the results obtained on respectively the D3Q27 and D3Q15 lattices.

As shown in figures 3.9 and 3.10, rotational invariance appears to be recovered for the D3Q27 lattice but not the D3Q15 lattice. It should be noted that the results for D3Q19 and D3Q15 appear rotated relative to each other, with the (010) plane on

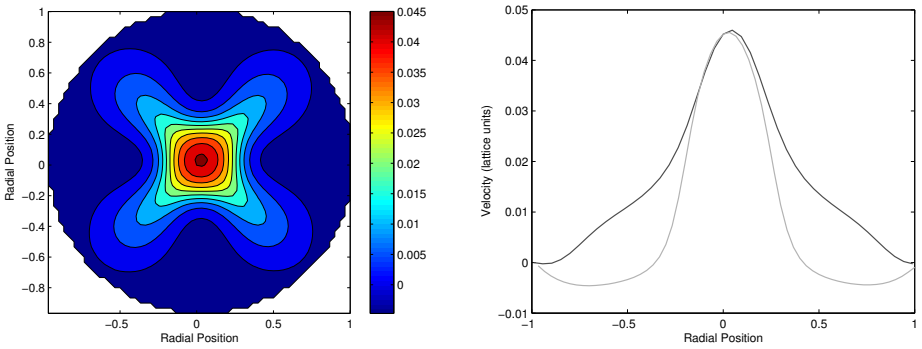

(a) Contour Plot (b) Velocity Profiles

Figure 3.8: Contour plot and graph of axial velocity on the (010) plane (light grey) and the (011) plane (dark grey) on D3Q19 lattice, $x = +4D$, *Re* = 500, *Ma* = 0.0545, regularized BGK collision operator

the D3Q19 lattice and the (110) plane on the D3Q15 lattice showing results which are qualitatively similar to the experimental results, whilst the (110) plane on the D3Q19 lattice and the (010) plane on the D3Q15 lattice show qualitatively different results. It is interesting to note that for both lattices the plane with the fewest velocity vectors produces results which disagree with the experimental data, whilst the planes with more velocity vectors show qualitative agreement with the experimental data.

The D3Q19 lattice model is the most widely used lattice for LBM. It was therefore considered important to determine whether unphysical effects observed were a result of inadequate implementation of the model or a fundamental problem with the method.

3.3.3.2 Effect of Grid Density

Under-resolved grids can produce unphysical results. To ensure that this was not the case in these simulations the effect of grid density on ϵ was investigated. Table 3.2 shows ϵ and u_{max}, the maximum velocity observed along the centreline normalized against the maximum inlet velocity, at location $x = +4D$ for different sized grids

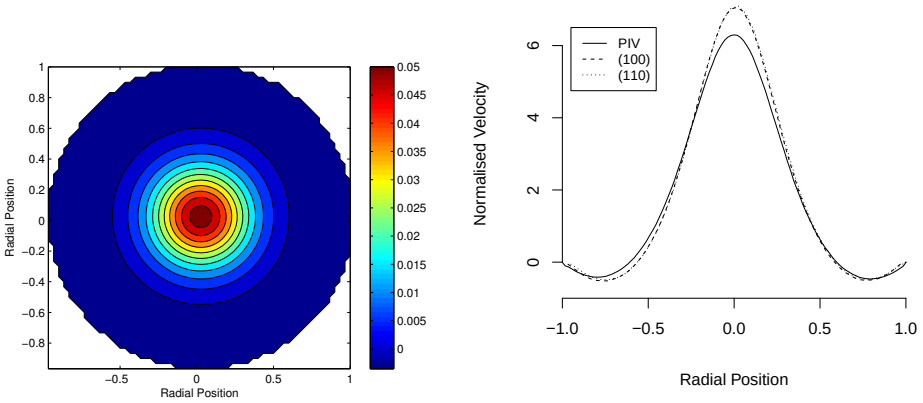

(a) Contour Plot

(b) Velocity Profiles

Figure 3.9: Contour plot and graph of axial velocity on the (010) plane (light grey) and the (011) plane (dark grey) on D3Q27 lattice, $x = +5D$, *Re* = 500, *Ma* = 0.0545, regularized BGK collision operator

applying a D3Q19 lattice and BGK collision operator at *Re* = 500. At very low grid density ϵ was observed to be at a minimum, after which little change was observed. It could be observed that changes in u_{max} introduced by increasing the resolution beyond 54 lattice nodes per diameter were less than 2%. This was the case both when simulations were performed at constant *Ma* and when *Ma* was decreased with increasing mesh density.

Table 3.2: Values of ϵ for different grid densities at $x = +4D$

Diameter (lattice units)	*Ma*	ϵ	u_{max}
48	0.0779	66.38%	8.56
54	0.0545	71.04%	8.29
60	0.0545	73.21%	8.16
64	0.0545	71.29%	8.22
64	0.0468	72.50%	8.23

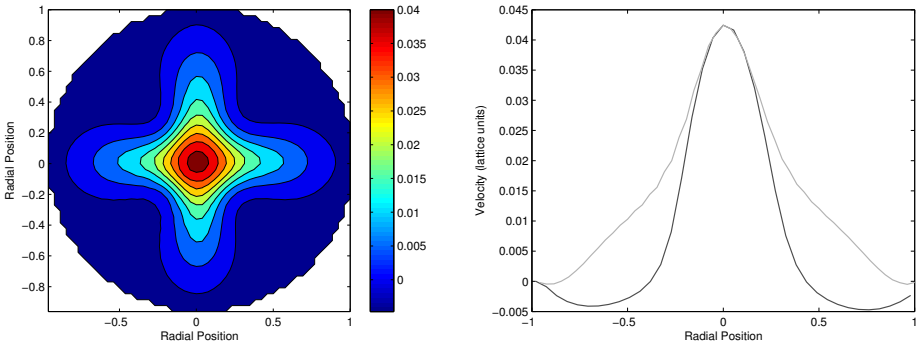

(a) Contour Plot (b) Velocity Profiles

Figure 3.10: Contour plot and graph of axial velocity on the (010) plane (light grey) and the (011) plane (dark grey) on D3Q15 lattice, $x = +2D$, *Re* = 250, *Ma* = 0.0468, BGK collision operator

3.3.3.3 Effect of Mach Number

As discussed in section 3.2.1 LBM is a weakly compressible scheme for CFD. However, in the experimental case compressibility effects were likely to be negligible, as the Mach number (*Ma*) was very low. It was therefore important to ensure that the erroneous results obtained with LBM were not caused by compressibility effects.

To investigate the effect of fluid compressibility, simulations were performed at equivalent *Re* (500) and with equal grid spacing (60 lattice units diameter) but for different *Ma*, defined as

$$Ma = u_{throat}/c_s \tag{3.13}$$

where u_{throat} is the average velocity inside the throat and c_s is the speed of sound, equal to $1/\sqrt{3}$ in lattice units. Table 3.3 shows that for *Ma* around 0.0545 the results are not strongly affected by changes in *Ma*, with both doubling to 0.109 and halving to 0.0275 having effects of less than 2% on both ϵ and u_{max}.

Table 3.3: Values of ϵ and u_{max} for different *Ma*

Ma	u_{max}	ϵ
0.109	8.288	73.41%
0.0545	8.170	72.48%
0.02725	8.184	73.62%

3.3.3.4 Effect of Collision Operator

The collision operator in the lattice Boltzmann equation, represented by the term on the right hand side of equation 3.5, can take various forms. For the simulations performed above either the BGK or regularized BGK collision operators. To ensure that the observed results did not depend on the choice of collision operator simulations were performed using a standard BGK, regularized BGK and MRT collision operators on a D3Q19 lattice at *Re* = 500. As shown in figure 3.11 these collision operators did not improve the axisymmetry, with values of ϵ of 72.98% for MRT, 72.71% for BGK and 72.48% for the regularized BGK simulation.

3.3.3.5 Axisymmetry at Different Locations

The axisymmetry of the results was also examined upstream from the expansion, both in the nozzle and the throat. It was found that the results before the expansion were fairly axisymmetrical in all 3 cases, with low values of ϵ at all locations studied. In the throat for the D3Q19 lattice the values of ϵ were around 6% while for the D3Q27 simulation the velocity inside the throat was slightly increased ($<$10%) compared to the D3Q19 simulation. Far downstream, at a location $x \approx +25D$ for *Re* = 500, all lattices showed axisymmetrical results and recovered a Poiseuille velocity profile. Figures 3.12 and 3.13 show the development of the velocity profile for the D3Q19 and D3Q27

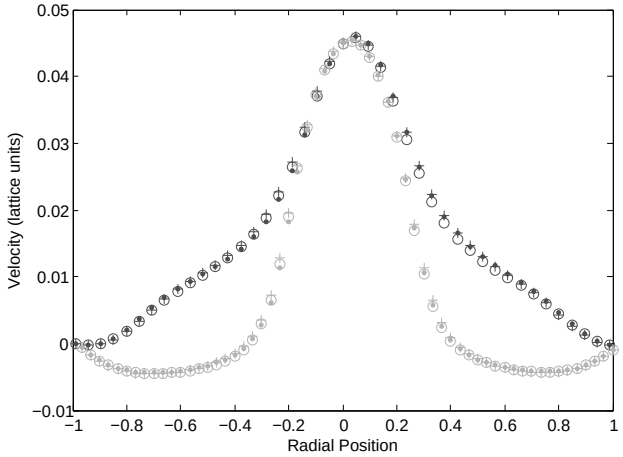

Figure 3.11: Graphs of axial velocity on the (010) plane (light grey) and the (011) planes (dark grey) for standard BGK (○), regularized BGK (solid dots) and MRT (+) collision operators on D3Q19 lattice, *Re* = 500, *Ma* = 0.0545, $x = +4D$

lattices at *Re* = 500 using a regularized BGK collision operator. From these two figures one can clearly observe that the velocity profile is strongly dependent on the chosen plane for the D3Q19 lattice but not for D3Q27.

3.3.3.6 Effect of Reynolds Number

To investigate the effect of flow complexity, simulations were performed in the same geometry on a D3Q19 lattice but at lower *Re*. Figure 3.14 shows the difference between axial velocity plots taken at $x = +4D$ on either the (010) or (011) plane for simulations at *Re* = 50 and *Re* = 250. It is evident that only the simulation at *Re* = 50 shows rotational invariance. The simulations at *Re* = 250 show different solutions on different planes, with ϵ = 38.39%. Similar features are observed at *Re* = 500 (figure 3.7). It should be noted that the value of ϵ produced by the D3Q19 lattice is lower than that produced by D3Q15 at the same *Re* (67.52%).

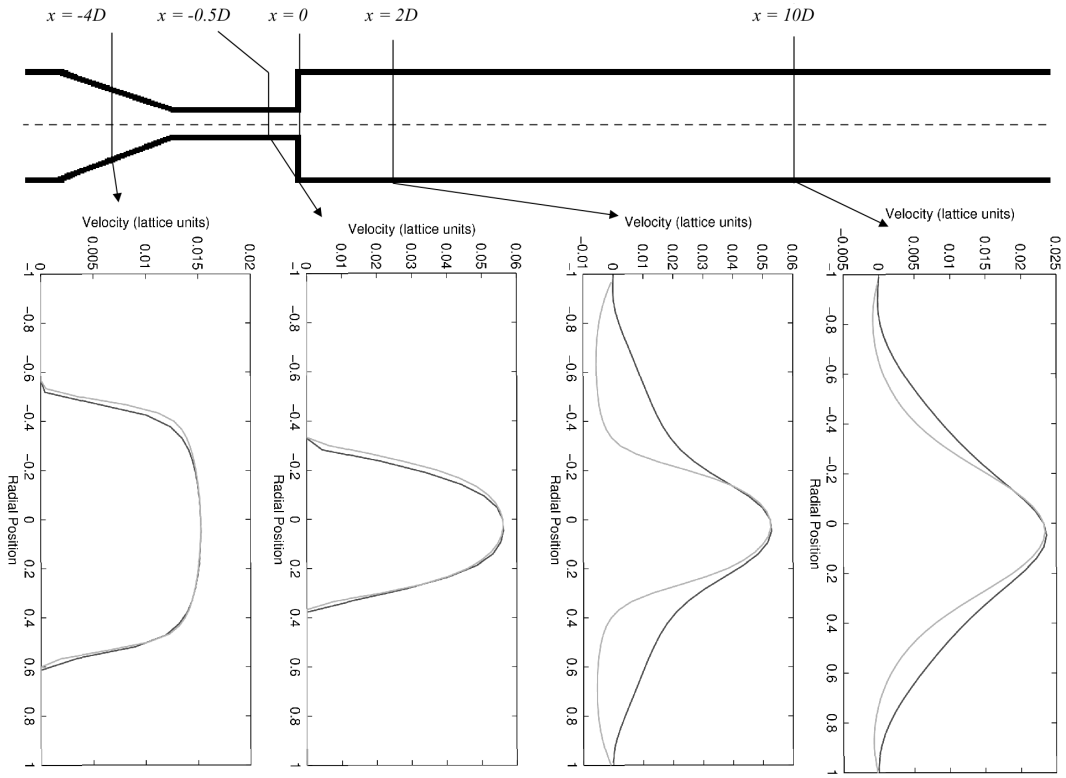

Figure 3.12: Development of velocity profile on (010) plane (light grey) and (011) plane (dark grey) at different locations for D3Q19 lattice

3.4 Discussion

Comparison between experimental flow data (PIV) and CFD results for the same flow condition has shown that FVM is able to produce excellent agreement with the PIV data throughout the flow domain. Although it has been previously shown that FVM is capable of reproducing experimental data [179] it is important to perform this validation to increase confidence in CFD results obtained using this scheme to make predictions when experimental data are not available as CFD results have been shown to be highly operator-dependent [71].

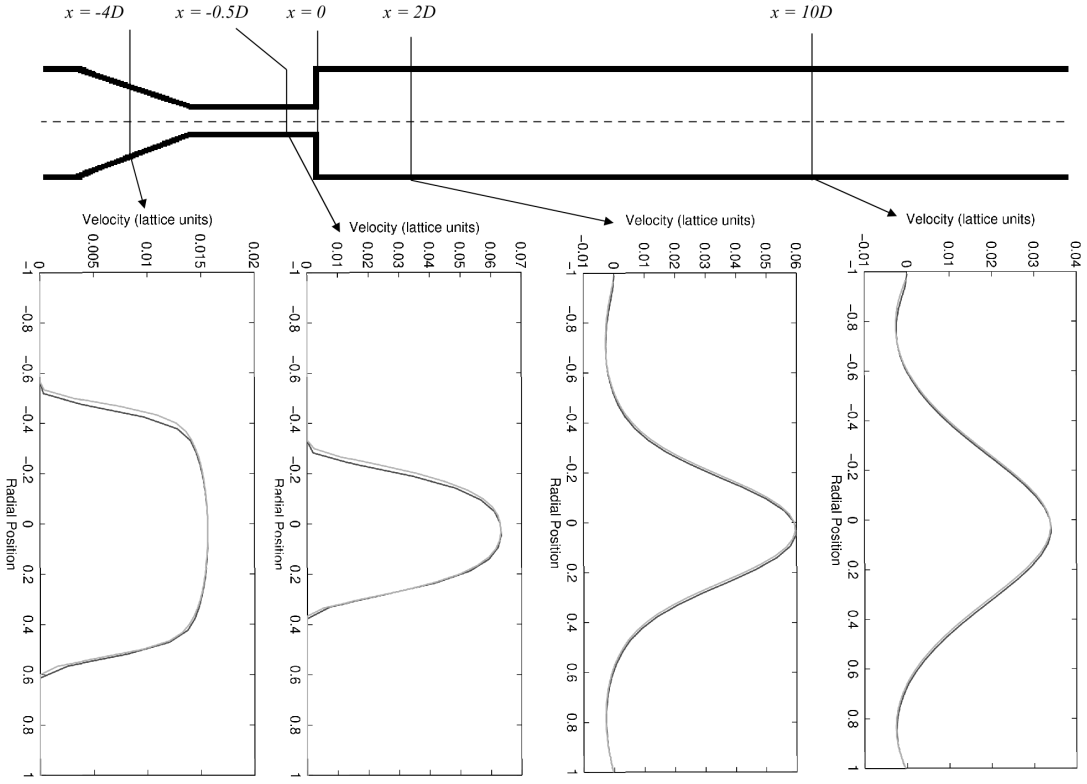

Figure 3.13: Development of velocity profile on (010) plane (light grey) and (011) plane (dark grey) at different locations for D3Q27 lattice

Comparison was also made between results produced by LBM and the experimental data. As LBM is a less well established method than FVM there have been fewer validations of the results produced by LBM, and many of these validations have used analytical solutions to the N-S equations as the benchmark, e.g. [3]. Therefore it is useful to study the performance of LBM on different lattices in this benchmark test for which the flow complexity is too high for an analytical solution to the NS equations to be obtainable.

LBM was able to produce good agreement with the PIV data for part of the flow domain. However, there were also locations where the agreement was very poor for

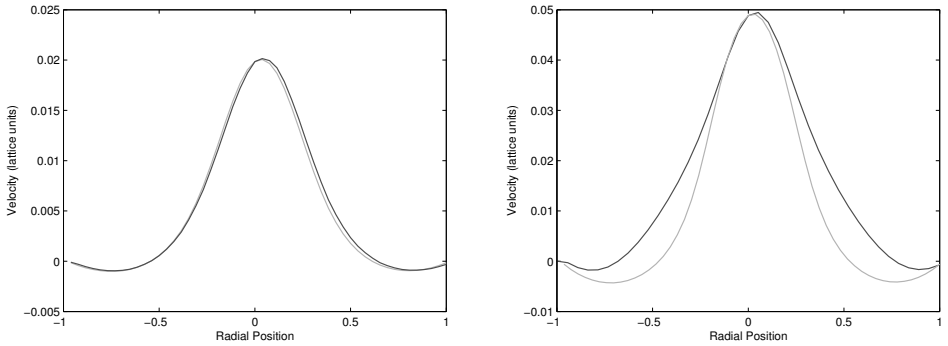

(a) *Re* = 50, $x = +0.5D$, *Ma* = 0.0218 (b) *Re* = 250, $x = +2D$, *Ma* = 0.0545

Figure 3.14: Graphs of axial velocity at different *Re* on (010) plane (light grey) and (011) plane (dark grey), BGK collision operator on D3Q19 lattice, *Ma* = 0.0545

both the D3Q19 and D3Q15 lattices. This appeared to be due to a lack of rotational invariance on these lattices. This lack of rotational invariance was present irrespective of grid density, suggesting an insufficiency in the lattice rather than errors due to an unresolved simulation. The lower value of ϵ at the lowest grid density on the D3Q19 was likely to be due to the increased effect of discretisation errors at this low density rather than an improved simulation.

The lack of rotational invariance in LBM observed may be due to the lack of velocity vectors in certain planes causing parts of the solution to be inadequately resolved. While this insufficiency is most obvious for axisymmetrical flows it may have a significant and undetected effect on flows in different geometries. This effect may be particularly important if LBM is being used to make predictions for real world problems for which no analytical solution or experimental data are available for cross examination or validation. Clearly, however, the main benefit of all CFD, including LBM could only be realized if it is able to accurately model flows in such situations.

The (011) plane on the D3Q15 lattice was the plane with the fewest velocity vec-

tors which showed qualitative agreement with the results on the D3Q27 lattice. The planes which did not agree were the (010) plane on the D3Q15 lattice and the (011) plane on the D3Q19 lattice, both of which have only five velocity vectors. This may be significant because the athermal, 2D NS equations require six independent components (pressure/density, two components of velocity and three components of the symmetrical mass flux tensor) to be fully defined. An analogy could be drawn between the planes with only five velocity vectors and the Hardy-Pomeau-de Pazzis (HPP) 2D lattice with four non zero velocities employed for lattice gas cellular automata (LGCA), which was the predecessor to LBM [70]. This lattice has been shown to be unable to properly recover the NS equations [56]. It is postulated that the planes which also have only four non zero velocities may show similar problems to this lattice when complex flow features are aligned with the plane because too few velocity vectors are present. Further work in this area supports the above hypothesis [88].

The effect of reducing *Re* was to reduce the expected flow complexity, as the vortices around the central jet are reduced in size, and improve the axisymmetry of the results. This would suggest that the larger vortices at higher *Re* cause an increase in flow complexity that is too much for the planes with fewer velocity vectors to accurately model, causing non axisymmetrical results. It is hypothesized that the lack of rotational invariance being present only at higher *Re* is because the five velocity planes are capable of modelling fluid behaviour when complexity is relatively low, in a similar manner to the HPP model for cellular automation. However, when the fluid displays more of the richness of the NS equations these planes are unable to fully capture it. Our results support this hypothesis, as when *Re* is high all planes with only five velocities show incorrect results. Under this circumstance it appears unlikely that similar problems would be observed when 2D lattices are used, as they have only one plane,

and for all commonly used lattices this plane contains sufficient velocity vectors. The D3Q15 lattice showed poorer agreement than the D3Q19 lattice when simulations were performed at equivalent *Re*. This suggests that D3Q15 is less suitable for modelling complex flows than D3Q19 and that it would begin to show a lack of rotational invariance at lower *Re* than D3Q19. On the other hand when compared to D3Q27 (figure 3.13), the insufficiency of the D3Q19 lattice is clearly demonstrated as it shows a very clear lack of rotational invariance downstream from the expansion where the flow is complex (figure 3.12).

The non axisymmetrical velocity profiles presented here have been observed previously in similar simulations by Harrison, using a D3Q19 lattice [72], in which the velocity contour plots observed were quantitatively similar to those observed in this study. Mayer and Házi also observed qualitatively incorrect results when using a D3Q19 lattice but not when using D3Q27 [109]. While the flow condition employed by Mayer and Házi was more complex than that used in this study, the results were similar in that the velocity contours in each quadrant were in close agreement, suggesting that their results depended upon the plane of the lattice with which the flow was aligned. Our results, coupled with the problems observed by Harrison and Mayer and Házi, suggest that when performing simulations in axisymmetrical geometries incorrect results may be present on certain planes of the D3Q15 and D3Q19 lattices even when the grid density is sufficiently high. Further work based on the hypothesis that the D3Q19 lattice produces inadequate results on the planes with fewest velocity vectors showed that LBM simulations of turbulent flows in pipes and ducts produced different results before and after a rotation if the D3Q19 lattice was used but not if D3Q27 was used [88].

These observations also highlight the importance of checking that simulation re-

sults are independent of lattice orientation in all geometries, as the problems present in the axisymmetrical geometry studied here may have more subtle effects in more complex geometries. As these results showed localized regions in which solutions were qualitatively incorrect they also highlight the importance of checking the solutions throughout the domain when validating CFD models against experimental data or analytical solutions.

It should be acknowledged that errors due to the discretisation of time and space are present in all CFD. In LBM errors are also introduced by compressibility, which are related to the discretisation of time because the velocity used in a simulation (in lattice units), and therefore *Ma*, must be larger when a larger timestep is used. It is expected that these errors would only disappear in the limit of infinite resolution of time and space. It was found in this study that compressibility errors were very small with negligible change in maximum observed velocity and small changes in ϵ when *Ma* was halved or doubled from 0.0545. Therefore, to accelerate convergence all simulations at *Re* = 500 or 250 were performed with *Ma*, based on the average velocity in the throat, close to 0.05 as this made the maximum observed *Ma* close to 0.1. Errors due to the discretisation of space were also small, with changes in maximum observed velocity of less than 2% at *Re* = 500 provided the diameter of the geometry was covered by at least 54 lattice nodes, which was the case in this study.

It should be noted that the relaxation parameters used in this study were fairly low at all times. This was necessary because *Re* was determined by the diameter of the throat, the mean velocity inside the throat and the lattice viscosity by the formula:

$$Re = \frac{ud}{\nu} \tag{3.14}$$

Available computational resources limited the diameter of the throat to around 20 lattice units, as the overall length had to be around 100 times greater than the diameter of the throat to ensure fully developed flow at the outlet. The requirement that Ma, as determined by equation 3.13, should be approximately 0.05 made the maximum viscosity for the required Re of 500 approximately 0.0025, corresponding to a relaxation time of 0.50075 which is lower than that required for optimal numerical stability and accuracy [92]. However, it is expected that increasing the relaxation parameters to the levels suggested by Kruger *et al* [92] would not change the overall result and would simply result in a very slow simulation at this relatively high Re. It was initially thought that the improvement in axisymmetry at lower Re was due to the increased lattice viscosity. However, in the simulation at $Ma = 0.109$ and $Re = 500$ shown in table 3.3 the viscosity was twice that used in the simulations at $Ma = 0.0545$ and the results were not significantly affected.

It should also be noted that, for the LBM simulations in this study, the walls were approximated by steps with no boundary smoothing performed. While this may have had a significant effect on the accuracy of the solution near the wall it is unlikely that the overall flow patterns were significantly affected. As the boundary shape was not particularly complex and a relatively high resolution was used in all simulations the circumference of the tube was represented by at least 180 cells in all simulations. The geometrical error is therefore likely to have been low. However, if convergence up to second-order accuracy was required then a more accurate boundary treatment would be necessary because the convergence of the geometrical error introduced at the walls is less than second-order. The small ϵ and the slightly increased velocity inside the throat could have been due to the lack of geometrical resolution which was highest in the throat due to its small diameter. However this geometrical error is unlikely

to affect the symmetry properties downstream from the throat since the diameter of the expansion is three times larger than that of the throat. If required, interpolated boundary conditions could be implemented; this is expected to significantly improve the geometrical accuracy and eliminate these errors as demonstrated by Chang *et al* [21]. Harrison hypothesized that the non axisymmetrical velocity profiles may have been due to the geometrical error at the boundaries [72]. However, this is unlikely to be the case, as Mayer and Házi also observed similar problems when interpolated boundary conditions were used [109].

When performing simulations using LBM, the choice of lattice, beside the flow complexity and grid density, significantly affects both the computational expense and the accuracy. In this study the simulations using D3Q27 were more computationally expensive than those at equivalent *Re* using D3Q19 as grid size was the same. However as the accuracy was significantly better this extra cost was justified. While the results of this study showed the D3Q27 lattice performed well it is acknowledged that the results presented here are limited to the system for which they were obtained. It is possible that for other systems or for similar systems with more complex flows than those investigated here, the 4^{th} order isotropy displayed by D3Q27 may be insufficient. If this were the case, it would then be interesting to investigate if the recently reported higher order lattices [28] or the off lattice D3Q27 model [186] which displays 6^{th} order isotropy would be more appropriate than the D3Q27 lattice. Further tests of the standard D3Q27 lattice to show whether or not its isotropy is sufficient, in flow systems beyond that investigated here, would therefore be beneficial, as it offers advantages such as reduced computational expense compared to the higher order model and simpler advection compared to the off lattice model. Nevertheless computational cost efficiency should not be at the expense of the accuracy of the solutions and higher order

lattices should be used when increased accuracy clearly outweighs any possible loss in efficiency, as was the case in this study. It is currently not possible to determine, *a priori*, the lowest order lattice which will produce acceptable results. Therefore further work to determine the specific circumstances in which different lattices are capable of producing adequate results would be beneficial.

Although the D3Q27 lattice was able to produce the expected axisymmetrical results it should be noted that this lattice appeared to slightly overestimate the centreline velocity for much of the domain. Therefore none of the LBM models studied were able to accurately model the flow in this situation. The reason for the overestimation of the centreline velocity by the D3Q27 lattice is not precisely known, although it is possible that the treatment of the boundaries may have caused a slight geometrical error which may be responsible for the overestimation of the centreline velocity.

In contrast to LBM, FVM was able to produce results which showed excellent agreement with the PIV data throughout the domain.

Although it has been previously shown that FVM is capable of producing results which are in excellent agreement with the PIV data in this benchmark study the results were highly operator dependent [71]. Reproduction of the excellent agreement suggests that the modelling process employed using FVM in this study can be expected to produce accurate results in similar simulations for which experimental validation data are not available.

As the performance of FVM was clearly superior to that of LBM it was decided that further work in this project should be performed using FVM rather than LBM.

Chapter 4

Design and Characterisation of Flowchambers

4.1 Introduction

An F-BS capable of producing flow waveforms which are proportional to physiologically realistic flow or WSS waveforms has been developed, as described in Chapter 2. This system was designed to apply a range of mechanical stimuli to cultured cells both individually and in combination. The desired mechanical stimuli were WSS, SWSSG, TWSSG and OSI. To expose cells to the desired mechanical stimuli using this F-BS it was necessary to establish flowchambers that cause the cells cultured within them to experience either WSS or SWSSG at a level which is proportional to the instantaneous flow rate through the chamber, which can be easily determined using the flow system. Combinations of mechanical stimuli can then be achieved as the TWSSG in a flowchamber designed for uniform WSS proportional to the flow rate is proportional to the temporal gradient in the flow rate and the OSI in such a chamber depends on the

level of flow reversal in the flow waveform.

It is important to relate the measured flow rates to the mechanical stimuli that they cause the cells to experience. However, experimental measurement of the WSS within the flowchamber is not possible. Therefore predictions regarding the relationship between the flow rate and the induced mechanical stimuli must be made using either analytical fluid mechanical relationships or CFD analysis. As the desired WSS environments are to be spatially and temporally non-uniform it is expected that analytical methods will not yield sufficiently accurate results. Therefore CFD analysis will be required to determine the mechanical stimuli within the flowchambers.

4.2 Methods

4.2.1 Design of Flowchambers

As discussed in section 1.1.4 many different flowchambers have been designed for applying mechanical stimuli including WSS and SWSSG to cultured cells. The most popular flowchamber for applying spatially constant WSS to cultured cells is the PPFC [53]. This design is popular because it is simple and it applies a uniform, easily determined WSS to a large number of cells. For these reasons it was decided that a PPFC would be suitable for use in this project.

Several flowchambers have also been developed to apply SWSSG to cultured cells, although none has gained as widespread use as the PPFC. These systems include the sudden expansion flowchamber [163], the 'T' shaped flowchamber [138] and converging flowchambers [43; 157]. However, the only flowchambers designed to date which apply a constant SWSSG are the converging flowchambers similar to those designed

by Dolan *et al* and Usami *et al* [43; 157]. These flowchambers produce a constant SWSSG by varying either the height [43] or the width [157] of the chamber along the flow direction. The following sections will discuss the design of the two flowchambers for use in this project.

4.2.1.1 Parallel Plate Flowchamber

The flow in a PPFC is often modelled as a fully developed, laminar flow between two infinitely wide parallel plates. For this assumption to be valid the criteria discussed in section 1.1.4.5 must all be satisfied. Under this assumption the flow is assumed to produce a uniform, parabolic velocity profile for the entire domain. This causes the cells cultured on one of the plates to experience a constant WSS which can be analytically determined using equation 1.2. Although it is unlikely that the assumptions discussed in section 1.1.4.5 will all be satisfied in the flowchambers employed in this study it is useful to use equation 1.2 in the design of a PPFC to obtain an approximate value of the WSS within the flowchamber. The accuracy of this approximation can then be tested using CFD.

The PPFC was designed to apply WSS to cells cultured on standard, 75mm by 25mm by 1mm glass microscope slides. The flowchamber consists of three main components:

- A bottom plate for housing the microscope slide with cultured cells.
- A top plate with inlet and outlet ports which fits on top of the microscope slide and bottom plate and produces a gap of known height for the flow to pass through.

- A silicone gasket which fits between the two plates and ensures that no leakage occurs.

The chamber is assembled by first carefully placing a slide with a monolayer of EC cultured on one side into the groove on the bottom plate. The gasket and top plate are then placed on top of the bottom plate and the plates are held together by machine screws, which are tightened until the surfaces of the plates which are outside the gasket meet. 2 way, 1/8 NPT - barbed connectors obtained from Cole-Parmer are provided to connect the flowchamber to the rest of flow circuit. Technical drawings showing the specifications and assembly of the flowchamber are provided in appendix A.

4.2.1.2 Converging Flowchamber

To achieve a constant SWSSG a converging flowchamber in which the height of the flowchamber varied as a function of the length along the chamber in the flow direction was designed. This flowchamber is qualitatively similar to that produced by Dolan *et al*, although the height of the chamber designed as part of this study is smaller than that used by Dolan *et al*. This results in a lower flow rate to get a desired WSS value, and therefore reduces the *Re* within the chamber. This is expected to lead to a less complex flow pattern within the chamber.

The height profile was designed based on a modified version of equation 1.2 in which h becomes $h(l)$ and varies from a maximum height, h_1 near the inlet to a minimum height h_2 near the outlet. Modifying equation 1.2 so that τ varies linearly with l and solving for $h(l)$ gives:

$$h(l) = \sqrt{\frac{6\mu Q}{b\tau(l)}} \tag{4.1}$$

The height profile can then be determined, given a desired flow rate and a given maximum and minimum WSS value spaced a given distance apart.

4.2.2 CFD Analysis

CFD was used to determine the WSS distribution within the flowchambers when the target flow waveforms shown in figure 2.6 were passed through the flowchambers. As discussed in Chapter 3, FVM was shown to outperform LBM and therefore simulations were performed using FVM implemented in Fluent.

Meshing was performed using the mesh utility in Ansys Workbench 13 for the PPFC and using Gambit for the converging flowchamber. As the domains for both flowchambers were symmetrical only half the domain was meshed in both cases and a symmetry boundary condition was applied at the symmetry plane. The PPFC mesh was produced using the same CutCell algorithm used in Chapter 3 whilst a mapped hexahedral mesh was used for the converging flowchamber. Mesh refinement studies were carried out by performing steady flow simulations on several meshes with different densities. Spacing was varied by a constant factor throughout the domain on all refinement meshes.

Simulation settings were similar to those employed in chapter 3, with the SIMPLE algorithm used for pressure-velocity coupling and second order discretisations used for both pressure and momentum.

Pulsatile boundary conditions were applied by writing user defined functions (UDFs) to describe the time evolution of the velocity distribution at the inlet, assuming a parabolic velocity profile and matching the volume flow rate to that described by the target flow waveforms shown in figure 2.6. Simulations of each pulse cycle were dis-

cretised into 200 time steps of 0.005s and at least 2 cycles were performed for each pulsatile waveform, with only the data from the second cycle used for analysis to eliminate start up effects. The simulation at each time step was ended either when all components of the scaled residuals dropped below 10^{-5} or after 150 iterations. Examination of the convergence history of the WSS on the cell culture surface showed that this condition was sufficient to yield results which did not change if more iterations were performed.

4.3 Results

4.3.1 CFD Results - Parallel Plate Flowchamber

4.3.1.1 Mesh Refinement

The mesh refinement study was performed on a series of five meshes with average cell edge sizing ranging from 0.3mm to 0.1mm, resulting in a twenty seven fold difference between the number of cells in the coarsest and finest meshes. Simulations were performed at a steady flow rate equal to the mean flow rate in the RCA, LAD and PA waveforms, which was predicted to expose the cells to a WSS of approximately 1.47Pa. The convergence of the average wall shear stress on both a small (2mm square) plane on the culture surface and a plane covering the entire culture surface was analysed to determine the spatial convergence of the results, as shown in figure 4.1.

Figure 4.1 shows that the results are very similar for the two most refined meshes, with changes in the WSS averaged over the different planes of less than 2.5%. The results on successive grids consistently show that WSS increases when a more refined grid is used but at a rate that decreases with the density of the grid. Therefore it is

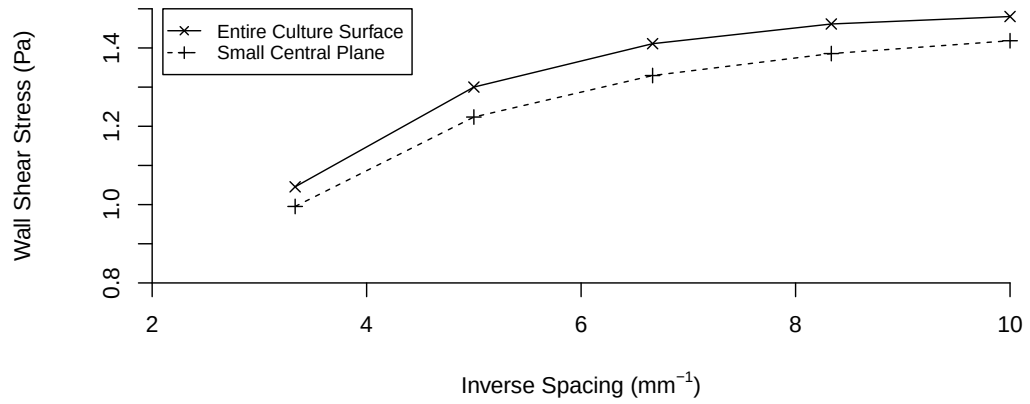

Figure 4.1: Average WSS on the entire culture surface and on a small plane in the centre of the culture surface for different mesh densities in the PPFC.

expected that the errors obtained by using the finest grid are acceptably small and that the true WSS experienced by the cells is slightly higher than that predicted by the CFD analysis.

Iterative convergence of the results was also examined, with negligible changes observed for several iterations before the calculations were terminated.

4.3.1.2 Analysis of Wall Shear Stress Distribution

The PPFC is designed to apply a spatially constant WSS to as great a proportion of the cells as possible. Figures 4.2 - 4.4 shows the distribution of WSS on the culture surface at different times in the LAD, RCA and PA waveforms, which are shown in figure 2.6. These contour plots show a relatively constant WSS over a large proportion of the culture area. However, it is difficult to quantitatively determine the area in which the WSS can be considered uniform at each time point from contour plots because small

variations are not clearly shown due to the large scale.

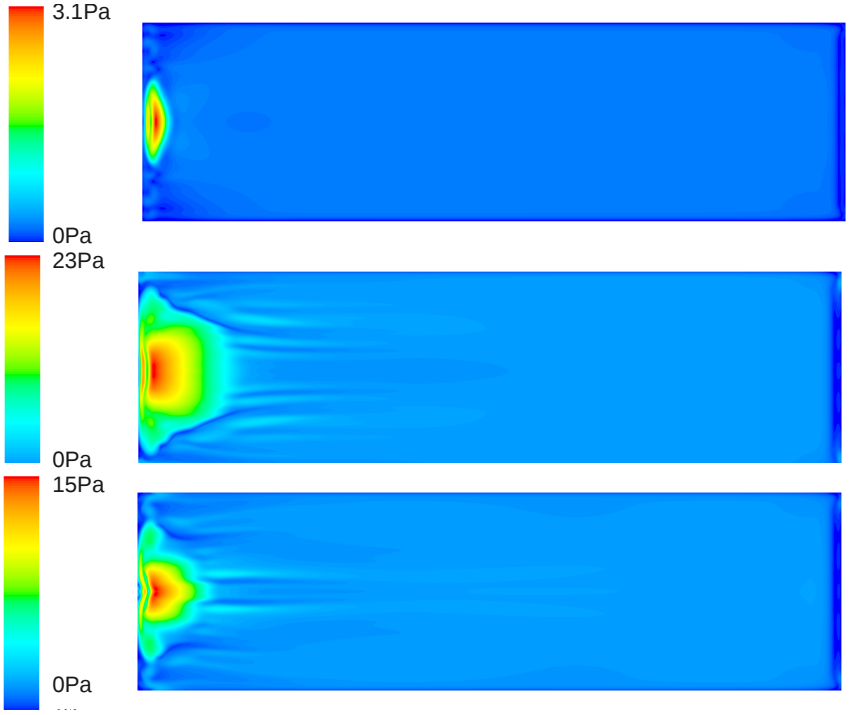

Figure 4.2: Contour plots showing the WSS distribution on the culture surface in the PPFC after 0.3s (top), 0.5s (middle) and 0.9s (bottom) in the LAD waveform. Mean flow is from left to right.

To quantify the proportion of cells exposed to spatially uniform WSS a nominal WSS value was defined at each selected time point from the RCA, LAD and PA flow waveforms by taking the average WSS on a plane positioned on the cell culture surface well downstream from the inlet and well away from the side walls of the chamber. The proportion of the rest of the culture surface that was predicted to experience a WSS within a defined tolerance of the nominal WSS was then computed, and the area in which the WSS was within the defined tolerance at all selected time points was determined. Figure 4.5 shows the areas which experience a WSS within 2%, 5% and 10% of the nominal WSS at all time points. The waveforms were the RCA and PA

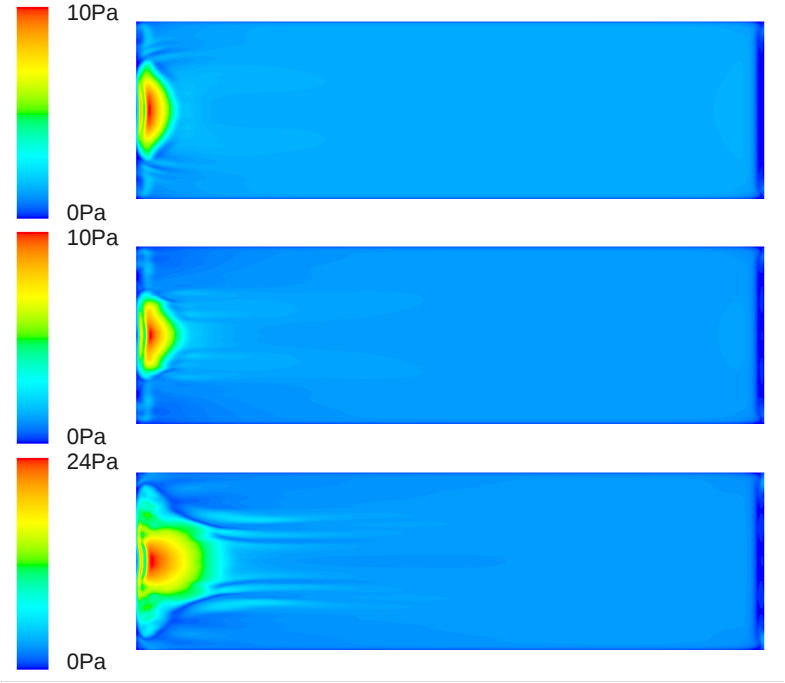

Figure 4.3: Contour plots showing the WSS distribution on the culture surface in the PPFC after 0.2s (top), 0.4s (middle) and 0.7s (bottom) in the RCA waveform. Mean flow is from left to right.

waveforms at a mean WSS of 1.5Pa and the PA waveform at a mean WSS of 0.75Pa. The proportions of the total area where cells were cultured with variations less than 2, 5 and 10% were respectively 11.5%, 45.3% and 72.4%. The areas exposed to variations of 2, 5 and 10% in the individual LAD, PA and RCA waveforms are shown in figure 4.6.

To reproduce the target WSS waveforms shown in figure 2.1 using the combination of the flowsystem and the flowchambers the WSS experienced by the cells in the PPFC must be approximately proportional to the instantaneous flow rate through the flowchamber. To determine the extent to which this assumption was valid the nominal WSS in the flowchamber was plotted against the instantaneous flow rate through

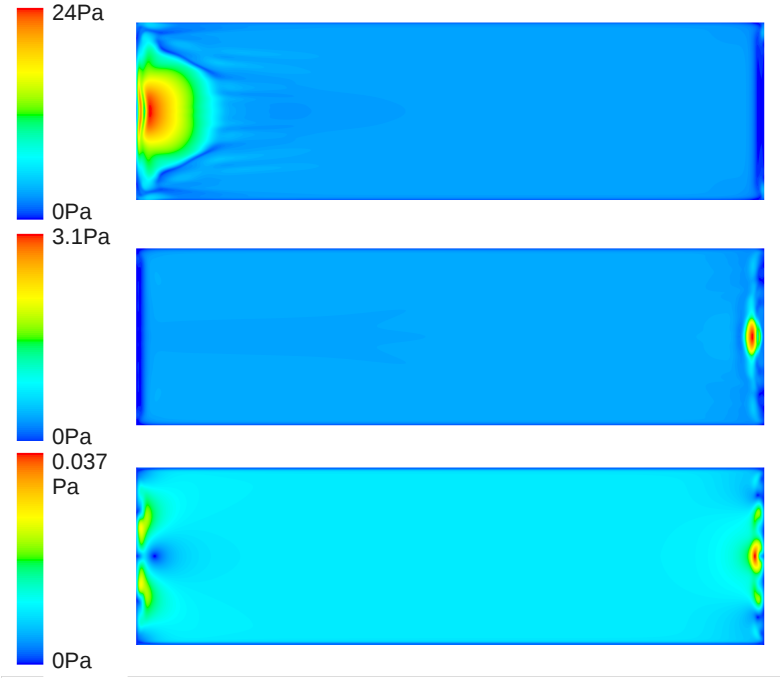

Figure 4.4: Contour plots showing the WSS distribution on the culture surface in the PPFC after 0.1s (top), 0.5s (middle) and 0.8s (bottom) in the PA waveform. Mean flow is from left to right.

the flowchamber at several time points in the different waveforms to determine the relationship between the WSS and the flow rate.

Figure 4.7 shows the correlation between the WSS determined by CFD analysis and that predicted on the basis of equation 1.2 and the instantaneous flow rate through the PPFC. It can be seen that the WSS determined by the two methods are very similar and hence the WSS experienced by the cells is approximately proportional to the flow rate through the chamber. However, there are time points where the WSS predicted by the CFD disagrees slightly with that predicted by equation 1.2.

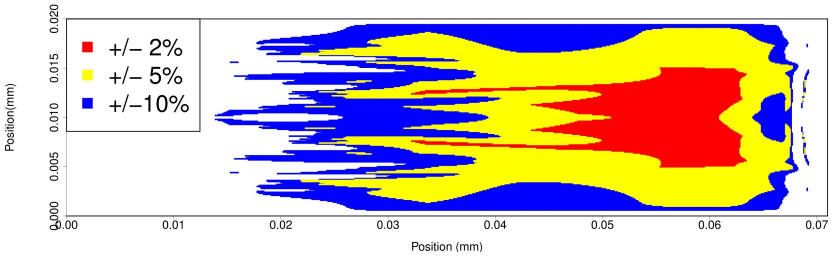

Figure 4.5: Cell culture areas exposed to variations of less than 10, 5 and 2% over all of the LAD, RCA and PA waveforms in the PPFC

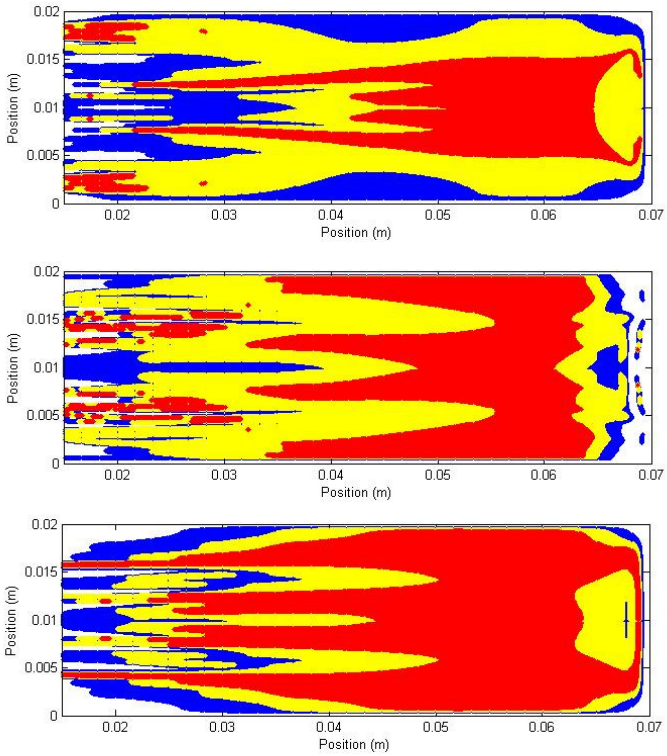

Figure 4.6: Cell culture areas exposed to variations of less than 10, 5 and 2% over the LAD (top), PA (middle) and RCA (bottom) waveforms in the PPFC

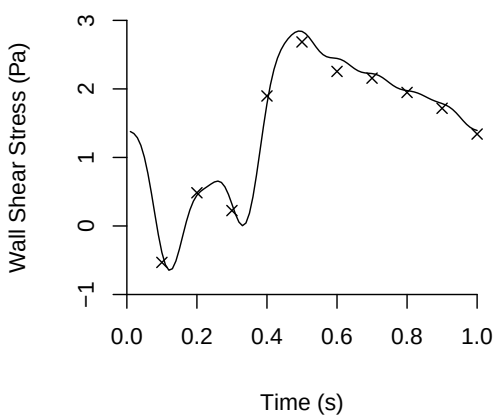

(a) LAD

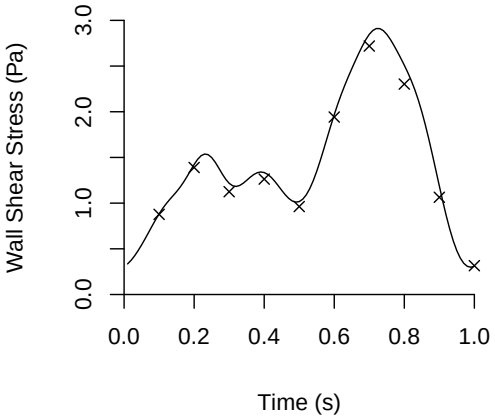

(b) RCA

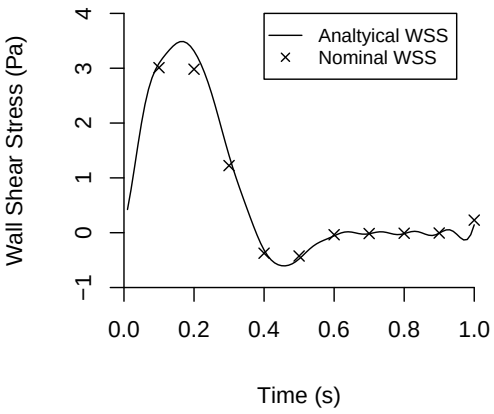

(c) PA

Figure 4.7: Graphs showing the analytical WSS determined from equation 1.2 over three flow waveforms and the nominal WSS determined by CFD analysis

4.3.2 CFD Results - Converging Flowchamber

4.3.2.1 Mesh Refinement

The mesh refinement study for the converging flowchamber was performed by computing the results of a steady flow at a flow rate equal to the mean flow rate in the LAD and RCA waveforms on a series of six meshes of increasing density. There was a 49 fold difference between the number of cells in the finest and coarsest meshes. The convergence of the WSS on the culture surface was examined by plotting the convergence of both the average WSS on the entire culture surface and the average WSS on a small (2mm square) plane located in the centre of the culture surface. The mesh refinement was performed for a steady flow because the mesh refinement study aimed to elucidate only the effects of spatial discretisation. Temporal discretisation was studied separately.

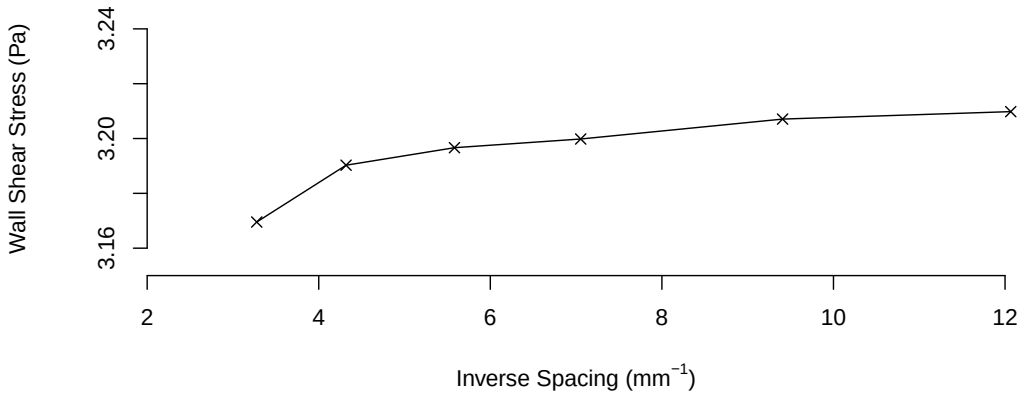

Figure 4.8: Average WSS on the entire culture surface for different mesh densities in the converging flowchamber.

Figure 4.8 shows the convergence of the WSS on the two planes as a function of the mesh density. Very small differences in WSS are observed between all meshes, with a difference of less than 1.5% in the mean WSS observed on the coarsest and finest grids. This clearly shows that the results are independent of the grid density throughout the range spanned by the meshes examined here. The third finest grid was chosen for use in the pulsatile flow computations as it displayed excellent accuracy at modest computational cost.

Examination of the WSS history during the calculations showed that the mean WSS did not change for several iterations before the calculations were terminated, suggesting that the results observed are independent of the number of iterations performed.

4.3.2.2 Analysis of Wall Shear Stress Distribution

Pulsatile flow computations were performed for the LAD and RCA waveforms at a mean WSS on 1.5Pa and the PA waveform at a mean WSS of 0.75Pa. The converging flowchamber was designed to produce a constant WSS in the inlet and the outlet and a constant SWSSG in the converging section. Figure 4.9 shows the WSS distribution on the culture surface in the converging flowchamber at selected time points. As expected, the WSS appears relatively constant in the inlet section, then increase steadily in the converging section before reaching a plateau near the outlet.

A constant SWSSG is required in the converging section. Figure 4.10 shows the WSS and SWSSG distribution along the centreline of the flowchamber at different time points for the LAD waveform.

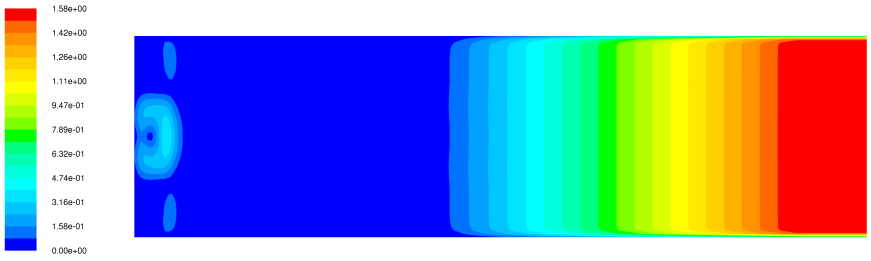

(a) 0.3s

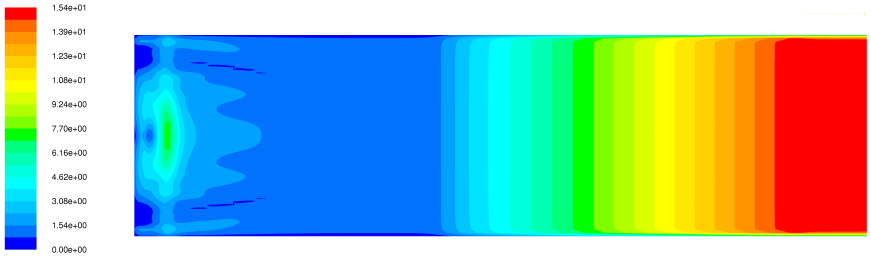

(b) 0.5s

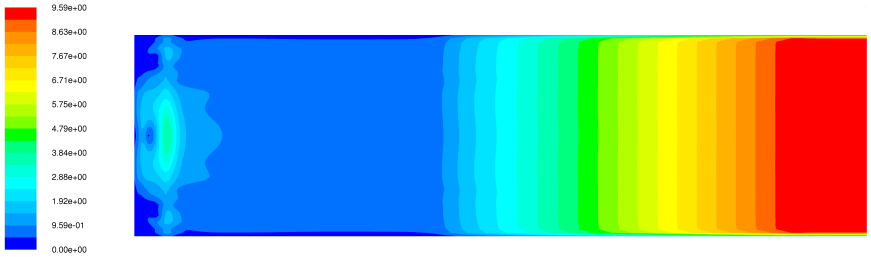

(c) 0.9s

Figure 4.9: Contour plots showing the WSS distribution (in Pa) on the culture surface in the converging flowchamber at different time points in the LAD waveform

4.4 Discussion

Flowchambers have been designed and characterised to apply mechanical stimuli to cultured cells in proportion to the flow rate through the chambers. Although analytical methods were used to approximately determine the mechanical forces experienced by cells in the chambers it was not possible to be sure that the assumptions made in the derivations of the analytical solutions were applicable in the flowchambers. Therefore

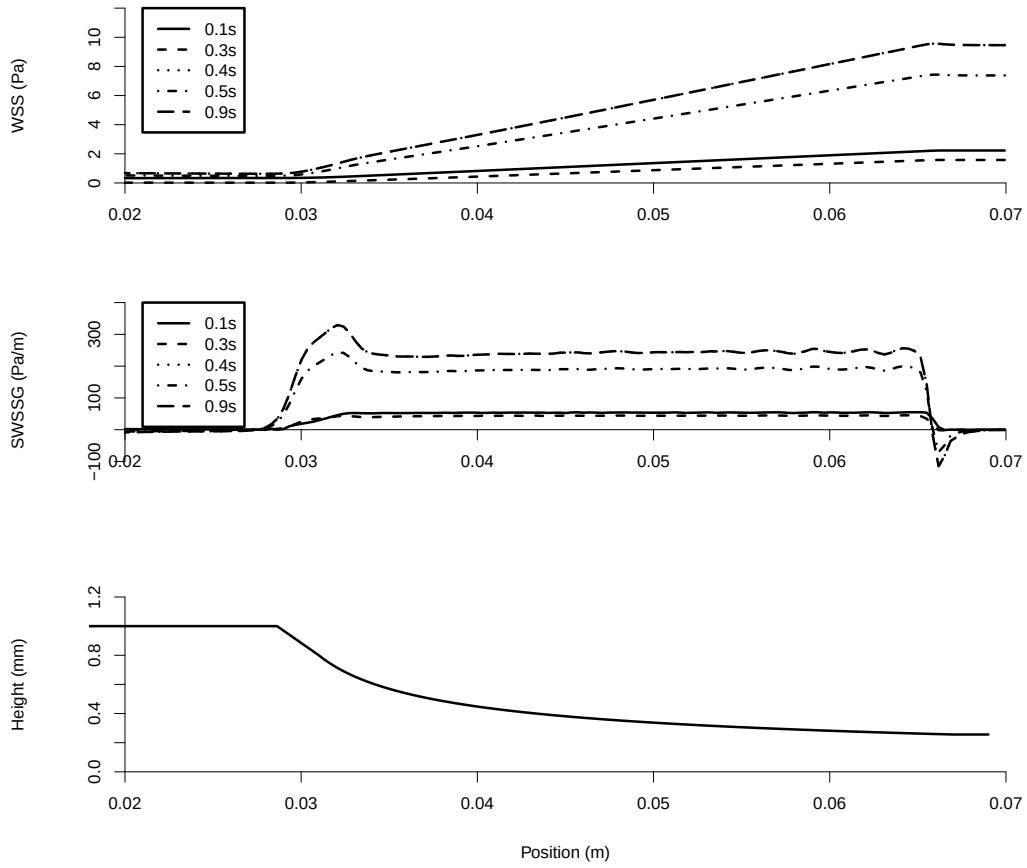

(a)

Figure 4.10: Line graphs showing the WSS (top) and SWSSG (middle) and flowchamber height (bottom) on the centre of the culture surface in the converging flowchamber at different time points in the LAD waveform

CFD was used to accurately determine the mechanical forces experienced by cells in the flowchambers.

Although CFD is a highly versatile and powerful tool for determining flow features which cannot be experimentally or analytically quantified it is well known that it can produce unrealistic results if appropriate care is not taken when performing CFD analysis [71]. The validation of the method performed in Chapter 3 showed that the software employed in this analysis using similar settings to those employed here is able

to faithfully reproduce experimental results. However, it was still important to ensure that the results observed in this analysis were independent of the spatial and temporal discretisations used. Similar results were observed on a wide range of meshes for both the PPFC and the converging flowchamber, with further refinement expected to produce changes of less than 5% for the PPFC and 1% for the converging flowchamber. Changes in the length of the time steps produced negligible changes in the results. Therefore the results obtained by CFD are likely to be very close to the true results.

The F-BS is designed to apply physiologically realistic WSS waveforms by passing a flow waveform which is proportional to the WSS waveform through a PPFC. This design is based on the assumption that the WSS experienced by cells cultured in the PPFC will be determined by equation 1.2. As shown in figure 4.7 CFD analysis of the WSS in the flowchamber showed reasonable agreement between the nominal WSS values in the PPFC and the WSS determined by equation 1.2. The small differences between the expected and the actual values are likely to be due to the transient effects introduced by the pulsatile flow.

The PPFC was designed to apply a spatially constant WSS. However, as the flow enters the PPFC from the tubing there is a significant geometric change, resulting in disturbances to the flow. Therefore the WSS within the PPFC is spatially non-uniform, as shown in figure 4.2 4.4. Although the variations are quite significant near the inlet to the flowchamber they are much smaller downstream from the inlet. It should be noted that the slide used for cell culture is sandblasted near the inlet, significantly reducing the number of cells exposed to the high WSS near the inlet.

Figure 4.5 shows that for the majority of the slide the variations are below 10% of the nominal WSS value and a significant area is subjected to variations of less than 5%. If experimental requirements dictate that the cells must be subjected to variations of

less than a particular value it is possible to use this figure to determine which areas of the slide cells should be analysed in. The individual coverage figures shown in figure 4.6 could be used for studies in which only the specific waveforms to which they relate are used. Previous studies using CFD to quantify the WSS over a pulsatile waveform have not shown maps of the variations [127]. Therefore it is difficult to determine how uniform the WSS is in these systems.

It is particularly important to determine the WSS variations in the PPFC used in this study as the *Re* is higher than that expected in many other PPFC systems e.g. [53]. As discussed in section 2.2.2 this was necessary to ensure that the flow rate was high enough to be accurately quantified using the ultrasonic flowsensor.

Analysis of the flow in the converging flowchamber showed that the cells were subjected to a constant WSS in the inlet and outlet sections and a relatively constant SWSSG for all of the converging section apart from a small ($<$5mm) region near the start of the converging section. The WSS distribution in the converging chamber is comparable to that observed by Dolan *et al*, who studied a steady flow in a similar converging flowchamber. However, the region of increased SWSSG near the inlet is smaller in this case compared to the flowchamber used by Dolan *et al*[43]. This may be because the maximum *Re* used by Dolan *et al* was higher (848) than that used in this study (384).

The flowchambers can be used in combination with the flow system described in chapter 2 to create a highly versatile, modular flow-bioreactor system (F-BS). The requirements set out in section 1.2 were that it should be capable of applying physiologically realistic, controllable levels of WSS, TWSSG, OSI and SWSSG. The F-BS is able to meet these requirements as temporally steady WSS can be applied by passing a steady flow through a PPFC. The magnitude of the WSS is determined by the

flow rate. TWSSG can be applied by using pulsatile flow instead of steady flow. Depending on the pulsatile flow waveform employed it is also possible to apply OSI by subjecting cells in a PPFC to pulsatile flow. It is possible to combine SWSSG with either temporally steady WSS or TWSSG by substituting the PPFC for the converging flowchamber. The modular design of the F-BS also allows for the future incorporation of further mechanical stimuli, for example cyclic stretch determined by the pressure waveform could be applied by culturing cells on a deformable membrane.

Chapter 5

Segmentation Programme for Quantifying Cell Morphology

5.1 Introduction

After exposure to mechanical stimuli cells are frequently analysed using florescence microscopy. Staining can be performed to determine the cell morphology by imaging specific organelles or to determine the level and location of the expression of molecules of interest. Whilst this method can produce excellent qualitative data it can be challenging to obtain quantitative data from fluorescence microscopy images.

To obtain quantitative data from images of stained cells investigators have performed manual counting and assessment of morphological features [47]. The human brain is well suited to the task of interpreting the potentially highly complex information displayed in florescence microscopy images. However, manual interpretation suffers from the disadvantage that the analysis may be operator-dependent, which may affect the repeatability of the results. Image processing routines have therefore been

developed to obtain quantitative data from microscope images [82]. These routines have the advantage that the analysis is entirely unbiased and repeatable. They are also potentially much higher throughput than manual quantification methods.

Various methods have been used to computationally segment images of stained cells including machine learning approaches [82] and watershed transform methods. However, segmentation is known to be more challenging when the cells in the image are confluent and therefore there is little or no space between the cells. The watershed transform is particularly efficient at segmenting images of closely-packed objects if markers for the objects to be segmented are available [64].

Flouresence microscopy images of cells frequently contain different stains for the nuclei and for cytoskeletal molecules such as actin. In these images the nuclei are typically distinct from each other and can therefore be easily segmented whilst the cytoskeletons of adjacent cells are typically very close together, making segmentation of the entire cell area difficult. As each cell contains exactly one nucleus it was hypothesised that a marker based watershed transform using the EC nuclei as the marker would be able to accurately segment combined images of the nuclei and cytoskeleton of confluent ECs.

5.2 Methods

5.2.1 Cell Culture

For routine cell work HUVECs (Promocell, Germany) were cultured in T25 or T75 flasks which were pre-coated with bovine skin gelatin for at least 30 mins. Growth medium was M199 containing 20% fetal calf serum (BioSera, UK), 30μg/ml endothe-

lial cell growth factor, 30μg/ml Heparin, 2mM L-Glutamine, 100U/ml penicillin and 100μg/ml streptomycin. Cultures were maintained in a humidified incubator at 37 degrees C and 5% CO_2. Culture medium was changed at least every 3 days. Routine passage was performed when cultures were 90-100% confluent, typically with a 1:4 split ratio. HUVECs were used before passage 5.

Cells for use in imaging or flow experiments were seeded on 75mm by 25mm by 1mm glass microscope slides (Corning, USA). The slides were thoroughly washed with distilled water then sterilised by soaking in a solution of 0.1% peracetic acid in phosphate buffered saline (PBS) for at least one hour followed by washing three times with sterile PBS to remove all of the peracetic acid. Sterile slides were then placed in dry petri dishes and coated with fibronectin (Sigma, UK) by placing 1ml of a 50μg/ml solution of fibronectin in Hank's balanced salt solution (HBSS) on top of the slide. The solution fully covered the surface of the slide without spilling onto the petri dish. Slides were then carefully placed into a CO_2 incubator (37^o)for at least one hour. The coating solution was then removed and P4 HUVECs were seeded onto the slide by adding 1.5ml of cell suspension containing 330,000 cells per ml. This resulted in a seeding density of approximately 26,700 cells per cm^2. Slides were then carefully returned to the incubator for a further 3-4 hours, after which time the petri dishes were flooded with 15ml of warm, complete medium (M199 containing 20% foetal calf serum (BioSera, UK), 30μg/ml endothelial cell growth factor, 30μg/ml Heparin, 2mM L-Glutamine, 100U/ml penicillin and 100μg/ml streptomycin). All cell culture reagents were obtained from Sigma (UK) unless otherwise stated.

5.2.2 Cell Imaging

All images were of confluent monolayers of ECs cultured on glass slides for 36-48 hrs. Some of the monolayers were subjected to steady or pulsatile WSS for 24hrs before staining, whilst others were unstimulated. Culture medium was aspirated and the monolayer was washed once with PBS then fixed in 3.7% formaledhyde for 20 minutes. After fixation the cells were washed three times with PBS then permeabailsed by adding 1% Triton-X100 for 3-5 minutes, followed by washing three times with PBS. Cells were then exposed to 1% bovine serum albumin in PBS for 30 minutes to block nonspecific binding. Staining solution was a 0.05 ng/ml solution of FITC conjugated Phalloidin (Sigma, UK) in PBS was then added to the cells for 40 minutes at room temperature. The cells were then washed in PBS before a 0.1μg/ml Dapi solution was added for 10 minutes, followed by a further wash with PBS. Cells were then air dried before a coversilp was mounted on top of the monolayer using general purpose grade DPX mounting medium (Fisher Chemical, UK).

Visualisation of the cells was performed using a flouresence microscope with appropriate excitation and emission filters (ImageExpress, Axon Instruments, UK). Images of the nuclei (Dapi) and the actin cytoskeleton (Phalloidin) were obtained at the same location and overlaid to produce composite images.

5.2.3 The Watershed Transform

Code for applying the watershed transform and other image processing operations is available in the Matlab image processing toolbox. Therefore the image processing routine required for this study was written in Matlab.

The watershed transform is an algorithm for segmenting a greyscale image into

several distinct regions. The algorithm is conceptually similar to finding the dividing lines between different basins in a topographic surface that is filled with water. The watershed transform considers the intensity values in the image to be representative of the height in the topographic surface and seed points are placed at local mimima. The image can then be considered to be ”filled with water” starting from these seed points. Watershed boundaries are placed at the points where the ”water” from different seed points meets.

This approach can result in over segmentation of the image (i.e. segmenting the image into too many distinct regions) if too many seed points are used. Therefore the algorithm can be improved by placing markers into the regions to be segmented and using only these markers as the seed points.

The watershed transform requires a greyscale image in which the boundaries between the objects have the highest intensity value and markers to determine the seed points. Therefore preprocessing of the images and identification of the seed points was required before the application of the watershed transform.

Each cell was expected to contain exactly one nucleus. Therefore the location of the nucleus was a convenient location for the seed points in the marker based watershed transform. The nuclei (stained with DAPI) were well separated and showed strong contrast with the background. Segmentation of the nuclei was performed by extracting only the DAPI channel from the image of the stained cells and then applying a threshold value of 1/3 of the mean intensity of the image, so that only locations where a nucleus was present remained. This produced a binary image in which the nuclei had a value of one and the background had a value of zero. Markers were then placed in the centre of each continuous region. This produced one marker per nucleus.

In the unprocessed images of the actin of the cells stained with phalloidin the

boundaries between the cells show minimal staining as the phalloidin is absent in these regions. To produce an image in which the maximum intensity values were at the boundaries it was necessary to invert the image. The strength of the maxima in the inverted images was improved by applying a background reduction technique to the images before the inversion of the image. This background reduction was performed by determining a value of the background staining using the Matlab function 'imopen'. This function is able to determine a matrix of local background values, thus correcting for nonuniform background staining across the image. The background values are then subtracted from the original image.

Once the inverted image is created it is further modified to ensure that local minima are present only at the locations of the markers identified at the nuclei.

To complete the segmentation the watershed transform is applied to the inverted images of the phalloidin stained cells, with minima imposed at the markers where the nuclei were detected. This ensures that the watershed regions are seeded only from the nuclei. The boundaries found by the watershed transform can then be superimposed onto the original image, and the morphological data relating to the image can be processed in Matlab, or exported to another application for further analysis.

A flowchart showing the procedure for segmenting images of cells stained with DAPI and Phalloidin using the watershed transform is shown in figure 5.1, and the Matlab code for preprocessing, segmenting and exporting morphological data from images of stained cells is presented in appendix B.

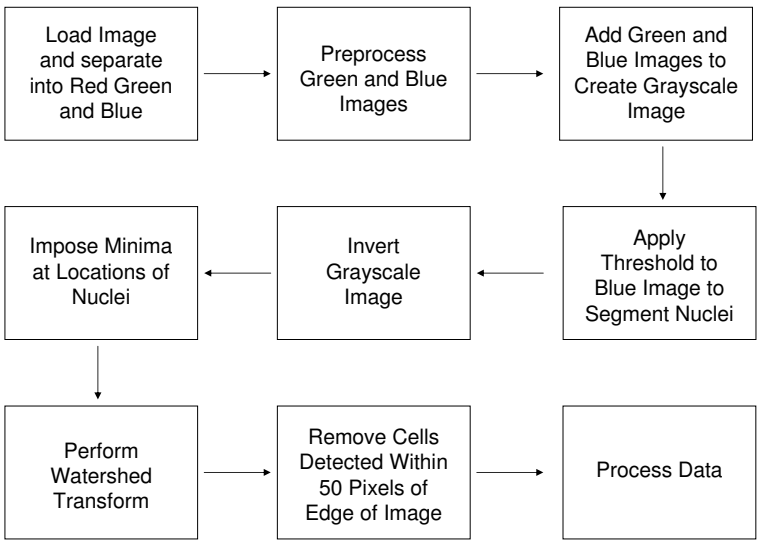

Figure 5.1: Flowchart showing the steps involved in segmenting images of cells using the watershed transform.

5.2.4 Quantification of Morphology

Once the segmentation is performed the morphological features of the segmented regions can be readily determined using the Matlab function 'regionprops'. The morphological features which can be quantified using this function include the cell area and aspect ratio and the orientation of the cell's major axis.

In addition to morphological features relating to the overall shape of the cells it it possible to determine the morphological features of the nuclei based on the threshold segmentation of the nuclei, and to calculate the position of the nuclei within the cell body.

Cells which are touching the edge of the image may not be imaged in their entirety,

resulting in an abnormally small cell being detected by the image processing code. Additionally cells near the edge of the image may include part of a cell whose nucleus was not in the image, resulting in the image processing code detecting an abnormally large cell. Therefore, all cells detected within 50 pixels of the edge of the image were excluded from the analysis of the morphological data. This appeared to eliminate the detection of artificially large or small cells near the edge of the image.

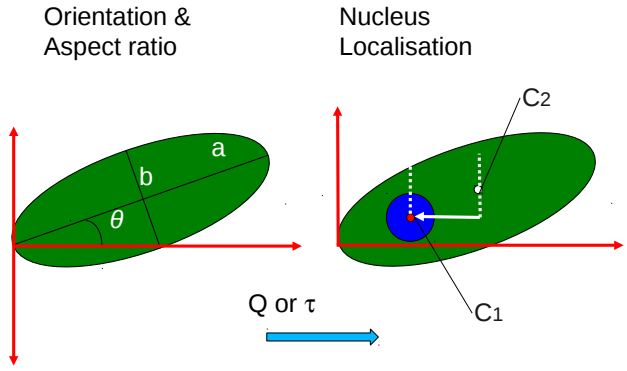

Figure 5.2: Illustration of the morphological parameters the segmentation programme can be used to study.

Figure 5.2 shows how the different morphological parameters are calculated. The aspect ratio is calculated by finding the length of the major axis (a) and dividing it by the length of the minor axis (b), whilst orientation is calculated by calculating the angle between the major axis and an axis parallel to the flow direction. For the calculation of both orientation and aspect ratio it is necessary to fit an equivalent ellipse to the area of the cell for the definition of the major and minor axes. The localisation of the nuclei either upstream or downstream on the flow (or WSS) axis is calculated by finding the distance between the centroid of the entire cell and that of the nucleus in the direction of flow.

5.2.5 Validation

The 'gold standard' method for quantifying the morphology of cells is to manually segment the boundaries of the cells and then determine the morphological features of the segmented areas. This can be performed using the drawing tools in ImageJ.

The morphology of individual cells can be found from the label matrix produced by the Matlab segmentation code. Therefore the morphological features of individual cells determined by automatic and manual segmentation can be directly compared to validate the accuracy of the segmentation programme. To validate the segmentation algorithm the size, aspect ratio and orientation of cells segmented manually in ImageJ and the automatic segmentation programme.

5.3 Results

5.3.1 Imaging

The staining and imaging process resulted in images of cells with the Dapi coloured blue and the Phalloidin coloured green. These two stains can be overlaid to produce composite images, as shown in figure 5.3

5.3.2 Segmentation Process

5.3.2.1 Background Reduction

The clarity of the background was clearly improved by the application of background reduction, as shown in figure 5.4. This improved the clarity of the borders between cells and produced an improved segmentation result.

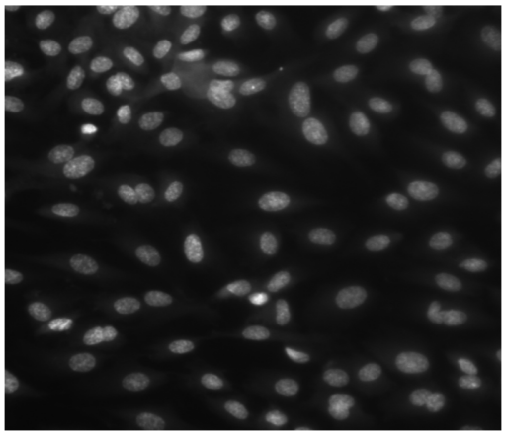

(a) Dapi

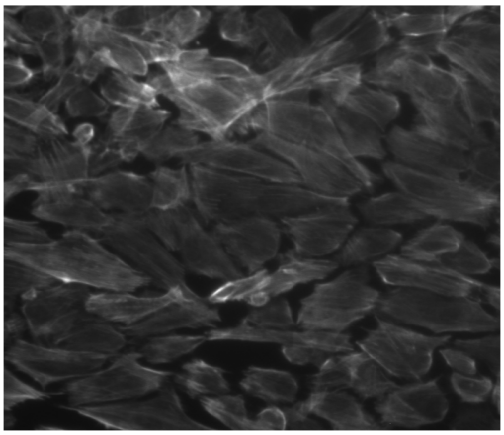

(b) Phalloidin

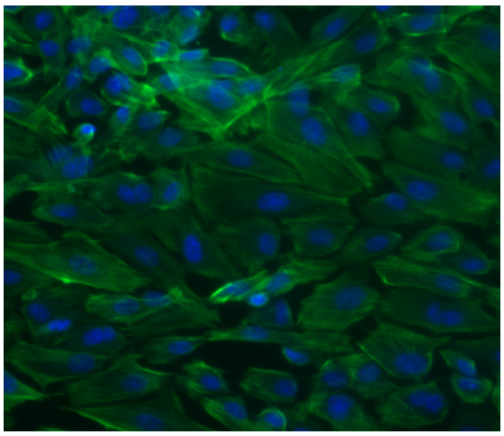

(c) Overlay

Figure 5.3: Images of ECs stained with Dapi and Phalloidin-FITC

5.3.2.2 Nucleus Segmentation

For the majority of images of confluent monolayers of HUVEC cells the nuclei were well separated, resulting in easy segmentation of the nuclei (a & b in figure 5.5). However, if the cells were allowed to become overconfluent then the segmentation sometimes failed to segment individual nuclei in some areas, resulting in several clumps of

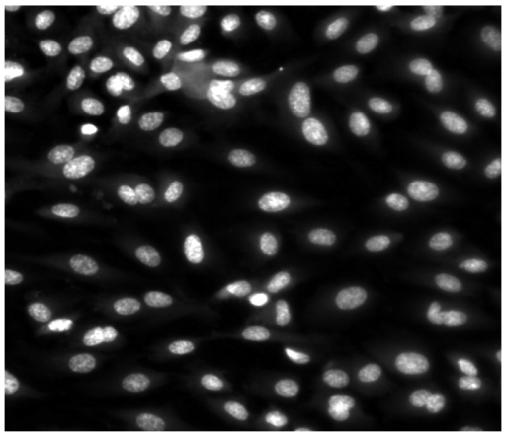

(a) Dapi

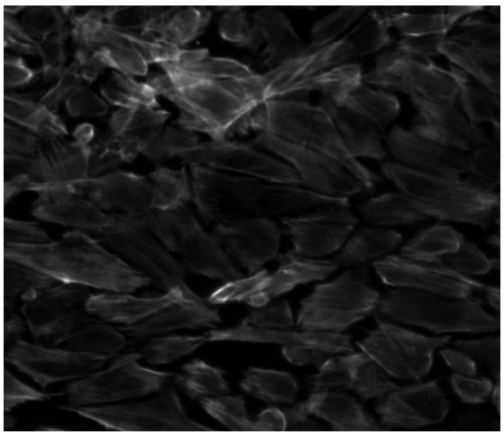

(b) Phalloidin

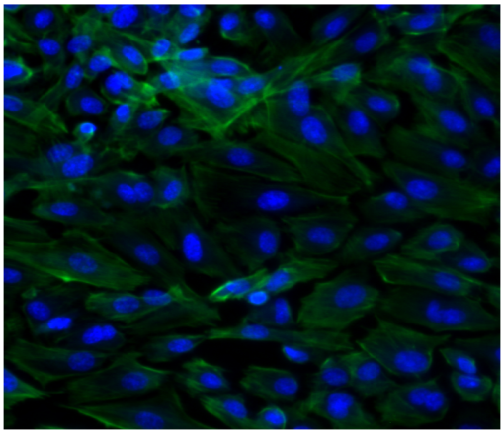

(c) Overlay

Figure 5.4: Images of ECs stained with Dapi and Phalloidin-FITC after automatic background reduction

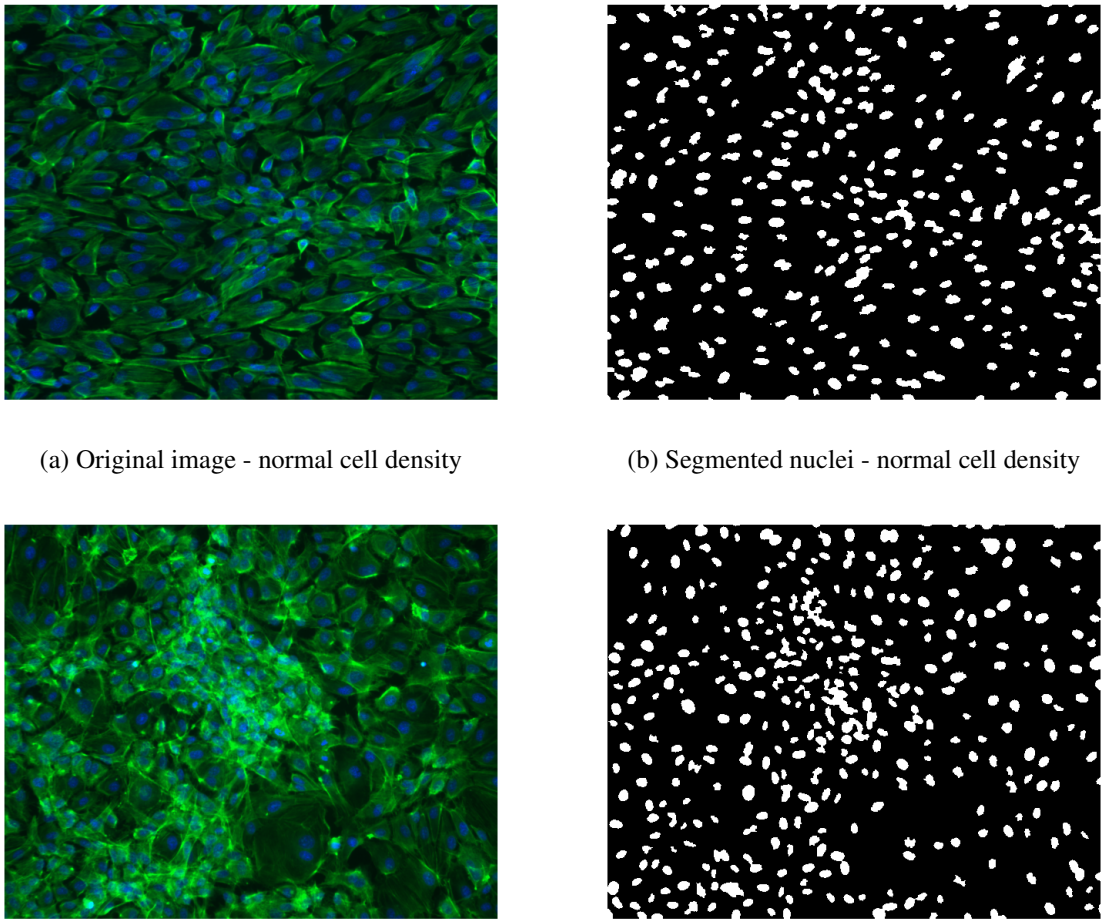

(a) Original image - normal cell density

(b) Segmented nuclei - normal cell density

(c) Original image - overconfluent cells

(d) Segmented nuclei - overconfluent cells

Figure 5.5: Nuclei segmented from original image to determine positions of markers for the watershed transform

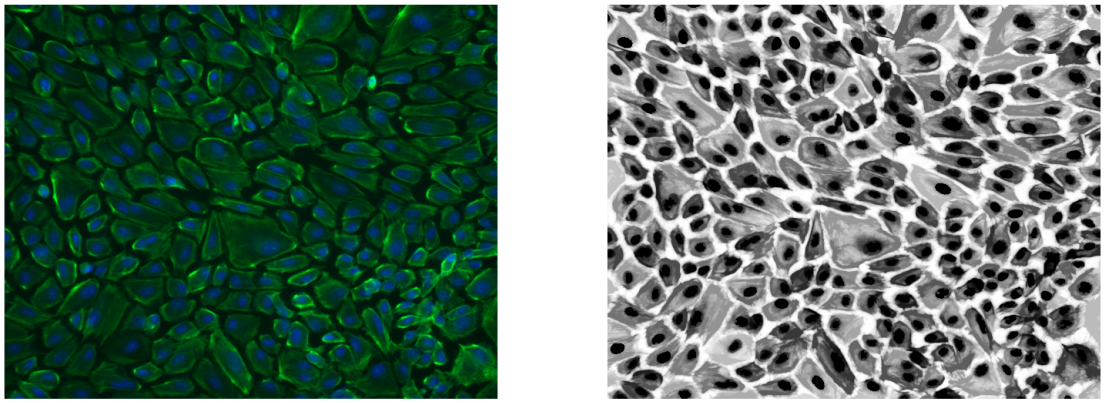

(a) Raw Image (b) Processed Image

Figure 5.6: Images of ECs stained with Dapi and Phalloidin then processed so that the watershed transform can be applied to segment the cells

nuclei which were recognised as single nuclei (c & d in figure 5.5). If further segmentation is performed on these images then inaccurate results will be obtained. It should be noted that these images are difficult to segment by any method as the boundaries of the cells overlap each other.

Cells which have more than one nucleus are sometimes segmented as individual cells but sometimes segmented as multiple cells, depending on how distinct the two nuclei are from each other. This may occasionally lead to inaccurate segmentation. However, in a normal monolayer of cells only a very small proportion are likely have more than one nucleus, as this is only likely to be observed for cells which are either mitotic or apoptotic.

5.3.2.3 Watershed Transform

The processing algorithm employed successfully modified the images into a form suitable for application of the watershed transform. Figure 5.6 shows a sample image

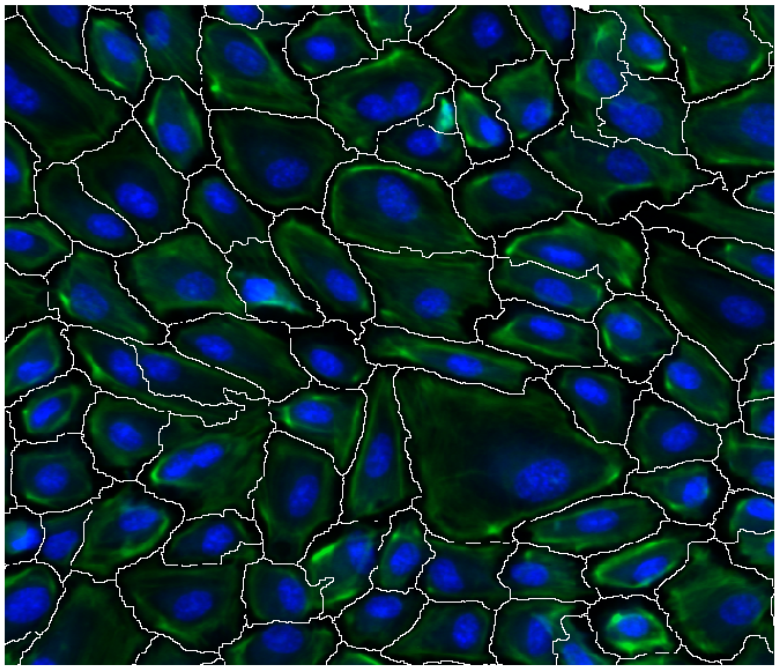

(a)

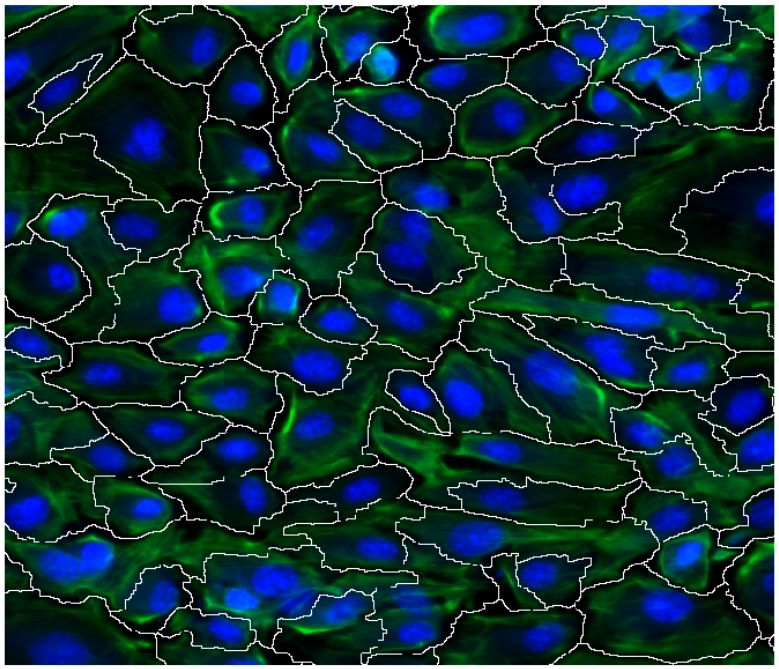

(b)

Figure 5.7: Sample images of cells segmented using the watershed transform code.

before the application of any processing and the same image after the background reduction, inversion and imposition of minima at the nuclei.

For all images of cells which were not overconfluent the watershed transform produced a segmentation result which appeared to be accurate, as shown in figure 5.7. However, quantitative analysis was required to ensure that the morphological data obtained from the segmented images were reliable.

5.3.3 Segmentation Accuracy and Validation

Quantitative analysis was performed by examining the correlation between the orientation, size and aspect ratio of cells measured using the image processing programme and manual segmentation using the drawing tools in ImageJ. The accuracy of the segmentation programme was determined by comparing the size, orientation and aspect ratio of corresponding cells segmented manually in ImageJ and automatically using the segmentation algorithm.

Figure 5.8 shows the correlation between the size, orientation and aspect ratio of 50 individual cells from 3 different images, including images of mechanically stimulated and unstimulated cells, segmented manually using ImageJ and the same cells segmented using the segmentation programme. Strong agreement between the two different methods is observed for all three morphological parameters, with an approximately 1:1 correlation and high r^2 values observed in all cases, as shown in table 5.1.

5.4 Discussion

A segmentation programme has been developed using the marker based watershed transform. This method is known to be effective in determining boundaries between

Table 5.1: r^2 values and gradient of line of best fit (m) for correlation between morphological parameters of individual cells segmented either manually using ImageJ or automatically using the Matlab image processing algorithm

Parameter	m	r^2
Area	1.01	0.676
Aspect Ratio	0.940	0.767
Orientation	0.977	0.793

objects, particularly when the objects are close together and so simpler segmentation methods would be less effective [133]. Although it is possible to apply the watershed transform without markers, its segmentation accuracy has been shown to be significantly better if markers are employed [64].

The segmentation programme works on images of the actin cytoskeleton and nucleus of cells. Staining of these organelles is frequently used to qualitatively assess the morphology of a cells. In the images shown staining was performed with DAPI to show the nuclei and Phalloidin to image the actin cytoskeleton. However, any combination of stains which bind to the nucleus and the actin cytoskeleton would be equally suitable, provided the molecules and/or the flurophores to which they were conjugated could be imaged at different wavelengths.

Assessment of the accuracy of the segmentation programme was performed by comparing the size, orientation and aspect ratio of cells segmented manually using ImageJ with the same parameters determined using the image processing programme. Whilst it was assumed that the results obtained using manual segmentation were accurate, it should be noted that it is not always clear where the boundaries of an individual cell lie. A limited amount of variability between operators is therefore to be expected when determining cell morphology by this method. However, the human brain

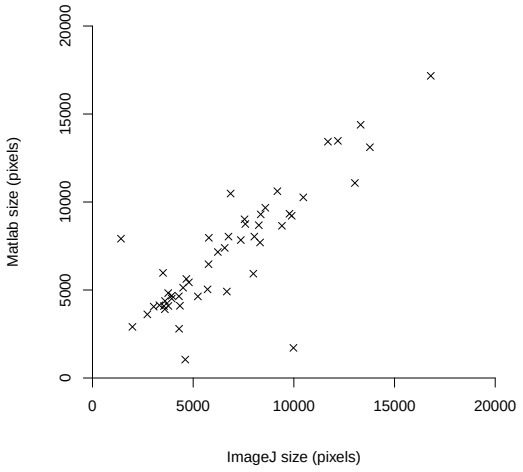

(a) Area

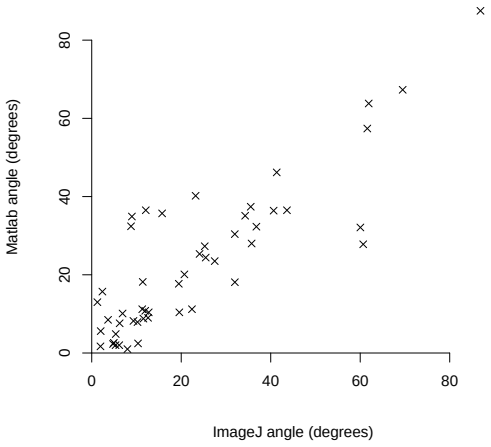

(b) Orientation

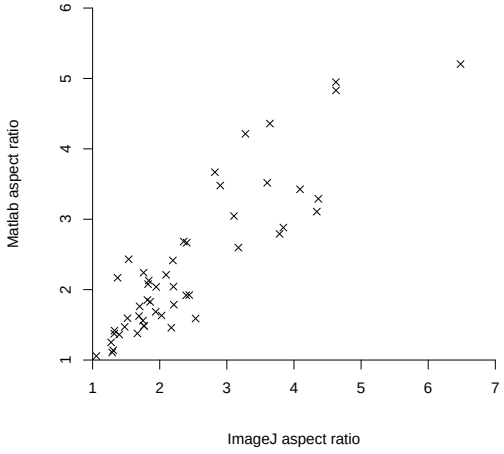

(c) Aspect Ratio

Figure 5.8: Scatter plots showing the correlation between different morphological parameters of individual cells segmented either manually using ImageJ or automatically using the Matlab image processing algorithm

is known to have excellent capacity for interpreting images and recognising patterns.

Manual segmentation should therefore be expected to give sufficiently accurate results

to assess the accuracy of the segmentation programme against providing a sufficiently high number of data points are used.

The performance of the segmentation programme appeared to be very good, with strong, approximately 1:1 correlations observed between values obtained by manual segmentation and the image processing programme for all three morphological parameters. r^2 were observed to be above 0.65 (table 5.1). Although these values are relatively low, it should be noted that determination of the morphology of a single cell by any method is likely to involve a high degree of uncertainty as the boundaries are unlikely to be immediately obvious. This uncertainty may be particularly evident when determining the orientation of a single cell if the cell is of relatively low aspect ratio. This is because, for shapes having a low aspect ratio, all of the axes of the cell are of similar length to the major axis. Therefore the determination of a particular axis as the major axis may be highly sensitive to small changes in the measured shape of the cell.

The limitations in determining the morphology of individual cells are significantly reduced when the morpholology of a large population of cells is investigated, as it is to be expected that the effects of small changes in measured cell shape, which may have a significant impact on the measured morphology of individual cells, will not have a significant effect when averaged over many cells. The approximately 1:1 correlations between the morphological parameters measured manually and using the segmentation programme therefore suggest that it is capable of producing similar results to manual segmentation when applied to large populations of cells. As a typical image of a monolayer of cells contain at least 100 cells it is likely that the average morphological features of entire images determined using the segmentation programme will be in close agreement with those determined by manual segmentation.

The use of a computational image processing programme has several advantages

over manual segmentation. A particular advantage of computational image processing over manual segmentation is that it is feasible to study the morphology of significantly larger populations of cells using computational image processing. This is particularly useful if an experiment is performed wherein cells at different locations experience significant variations in mechanical forces. In this case then the image processing programme may help to correlate the mechanical forces experienced by cells to their morphological response. The converging flowchamber which was computationally analysed in Chapter 4 may be used in such an experiment.

Another advantage of computational image processing is that the variability in results between operators and the possibility of operator bias affecting the results is eliminated. Although operator bias can be reduced in manual segmentation by 'blinding' the operator performing the segmentation to the experimental conditioning applied to each image, this may not be feasible when experimental conditions cause clear changes in morphology from which operators are likely to be able to infer which images are of experimentally conditioned cells and which are of controls.

In conclusion, a computational image processing routine using the marker-based watershed transform has been developed and tested. This routine can be applied to images of cells obtained using techniques which are widely available in cell culture laboratories. It shows good agreement with manual segmentation of the cells, whilst eliminating some of the drawbacks associated with manual segmentation.

Chapter 6

Effect of Physiologically Realistic Fluid Mechanical Parameters on EC Morphology

6.1 Introduction

Previous work studying the morphology of ECs subjected to WSS *in vitro* has shown that they align in the direction of WSS and elongate [54; 58]. This effect can be observed for both pulsatile and steady flow [14]. The degree of realignment has been shown to depend on the magnitude of the WSS and the duration of its application [100].

It is well known that the morphology of ECs *in vivo* is also dependant on the magnitude of the WSS that they experience, with ECs showing clear alignment in the direction of flow in areas of high WSS but not at the locations where the flow is disturbed [98]. The relationship between EC morphology and WSS *in vivo* has been used to infer

the WSS patterns in animal vessels [14].

EC morphology may be a valuable marker for determining the health of an endothelium. It has been shown that cultured ECs which show the aligned, elongated morphology typical of atheroprotected sites *in vivo* have significantly reduced inflammatory activation compared to ECs which show no preferential alignment or elongation. Interestingly, this reduction in inflammatory activation was present for morphological changes induced by micropatterning of the EC culture surface as well as by the application of WSS [159]. This suggests that the morphology displayed by ECs at atheroprotected parts of the vasculature helps to promote an atheroprotective pheontype.

The majority of previous work studying morphological changes in ECs exposed to WSS has investigated the effect of either steady WSS or sinusoidal WSS waveforms [78; 100]. Work investigating the response of ECs to physiologically realistic pulsatile WSS has also been performed, showing similar morphological changes to those observed under steady WSS [16; 34; 184]. However only a limited amount of work on the effects of pulsatile WSS compared to steady WSS and the effects of SWSSG on EC morphology has been performed.

The different effects of steady WSS and pulsatile reversing and non-reversing WSS on bovine aortic EC (BAEC) morphology have been investigated by Helmlinger *et al* [78]. This study showed that BAECs showed a greater morphological change for steady flow than pulsatile reversing flow. However, pulsatile non-reversing flow induced an even greater morphological change. It should be noted that the flow waveforms employed in this study were sinusoidal and therefore did not contain the higher frequency components present in physiologically realistic flow waveforms.

Relatively few investigations of the effects of SWSSG on cultured ECs have been

performed. Using similar converging flowchambers to those described in chapter 4 Dolan *et al* showed that when exposed to high SWSSG with the positive gradient in the flow direction (i.e. an accelerating gradient) ECs show significantly reduced alignment with the flow direction. However, this effect was not observed when the gradient was in the opposite direction to the WSS (i.e. a decelerating gradient) [43]. A similar effect of high, accelerating SWSSG was observed by Sakamoto *et al* in a 'T' shaped flowchamber [138]. However, to the author's knowledge there have been no studies to date investigating the morphological response of ECs to a combination of physiologically realistic pulsatile WSS and SWSSG.

The F-BS described in chapters 2 and 4 is ideally suited to studying the different effects of pulsatile and steady flow as experiments subjecting cultured ECs to steady and pulsatile flow can be run in parallel. The morphological responses to steady WSS are well characterised. Therefore, studies using the experimental apparatus described in chapters 2 and 4 to investigate the effects of steady WSS on ECs will have the additional benefit of providing a biological validation of the apparatus by confirming that it is capable of producing similar results to those already reported in the literature.

6.2 Methods

6.2.1 Cell Seeding

Routine culture of HUVECs and seeding on slides for use in experiments was performed as described in section 5.2.1. After seeding slides were left overnight to become confluent before use in flow experiments.

6.2.2 Flow Experiment Setup

Experiments studying pulsatile and steady flow were run in parallel. For the pulsatile flow experiments the flow circuit was assembled as shown in figure 2.2 but with the test section replaced by a two way connector. To apply steady flow the circuit was assembled in a similar way but the tubing attaching to the pulsatile pump was not included. Once assembled the flow circuits were sterilised by autoclave, leaving the openings where the pulse dampeners and the sterile filters were attached open to allow steam to enter the tubing. Once sterilised, the medium reservoirs were each filled with 60ml of warm, complete medium and the flow circuits were placed in an incubator for at least 2 hours with the flow rate set to 10ml/min to allow the temperature of the circuit and culture medium to equilibrate.

After equilibration of the flow circuit was completed the slides seeded with HUVECs were washed once with warm HBSS then carefully placed into the groove on the bottom plate of the test section. The gasket and the top plate were then placed on top of the slide and held in place with machine screws. The test sections were then completely filled with warm, complete medium to prevent the formation of bubbles. To attach the test sections to the flow circuit the tubing was clamped either side of the two way connector which replaced the test section in the initial assembly. The two way connector was then removed and the tubing was attached to the inlet and outlet of the test section. For the study of spatially constant WSS cells were housed in a PPFC, whilst a converging flowchamber was used for the study of SWSSG.

Once the test sections were in place the flow rate was gradually increased to the desired mean flow rate over approximately 30 minutes, the flow rate starting at 5ml/min and being doubled every 5 - 10 minutes until the desired flow rate was reached. Once

the desired mean flow rate had been reached the pulsatile component of the flow waveform was applied by switching on the pulsatile pump at the desired speed.

The cells subjected to pulsatile flow were exposed to the LAD flow waveform with a mean flow rate of 144ml/min, as shown in figure 2.6, while cells subjected to steady flow were exposed to a constant flow rate of 144 ml/min. All experiments were performed at ambient pressure. This resulted in both samples experiencing a mean WSS of 1.5Pa. Cells were subjected to these waveforms for 24 hours in the PPFC and 18 hours in the converging flowchamber.

6.2.3 Staining and Data Processing

After the cells had been exposed to flow for the desired length of time the pumps were stopped and the slides were carefully removed from the test sections. The cells were washed twice with PBS then fixed for 20 minutes in 3.7% formaldehyde. Staining and imaging were then performed by the process described in section 5.2.2. The microscope used was capable of focusing on different locations on the slide, with a resolution of less than 1μm. In all cases the slide was located in a holder which ensured that all slides were at the same reference location when images were taken.

Analysis of the cell morphology was performed using the image processing programme described in Chapter 5. To investigate the effects of the small variations in WSS revealed by the CFD analysis of flowchamber images were taken from different locations on the slides and statistical comparison was made between cells exposed to different variations in WSS. For the experiments in the PPFC the images were taken from regions in which variations in WSS were less than 10%, as shown in figure 4.5.

Statistical significance of comparisons was analysed using a 2 tailed, unpaired,

Student's T test, with the critical p value for statistical significance taken to be 0.05.

6.3 Results

6.3.1 Spatially Uniform Wall Shear Stress

As expected, HUVECs exposed to both steady and pulsatile WSS in the PPFC showed clear elongation and realignment in the direction of the WSS after 24hrs exposure. Figure 6.1 shows phase contrast images of HUVECs after 24hrs of steady WSS of an average magnitude of 1.5Pa and pulsatile WSS approximating the LAD waveform, also with an average WSS magnitude of 1.5Pa, along with a static control. In all cases the cells appear to be healthy and the integrity of the monolayer is maintained. Clear realignment in the direction of flow is also observed for the cells exposed to pulsatile and steady WSS. Initial analysis of the the morphology of the cells exposed to pulsatile WSS and steady WSS appears to show similar results for both conditions.

HUVECs exposed to WSS were also stained using DAPI and phalloidin. Figure 6.2 shows sample images of the nuclei (stained with DAPI), the actin cytoskeleton (stained with phalloidin) and overlays of both stains for HUVECs exposed to 24hrs steady WSS, 24hrs pulsatile WSS and static controls. From these figures it can be seen that both the nuclei and the entire cell bodies realign in the direction of the WSS for both steady WSS and pulsatile WSS, while no such response is observed in the static control cells.

Stained images of HUVECs exposed to steady and pulsatile WSS, as well as static controls were analysed using the segmentation programme described in Chapter 5. The morphology of the cells exposed to the different stimuli were analysed by comparing

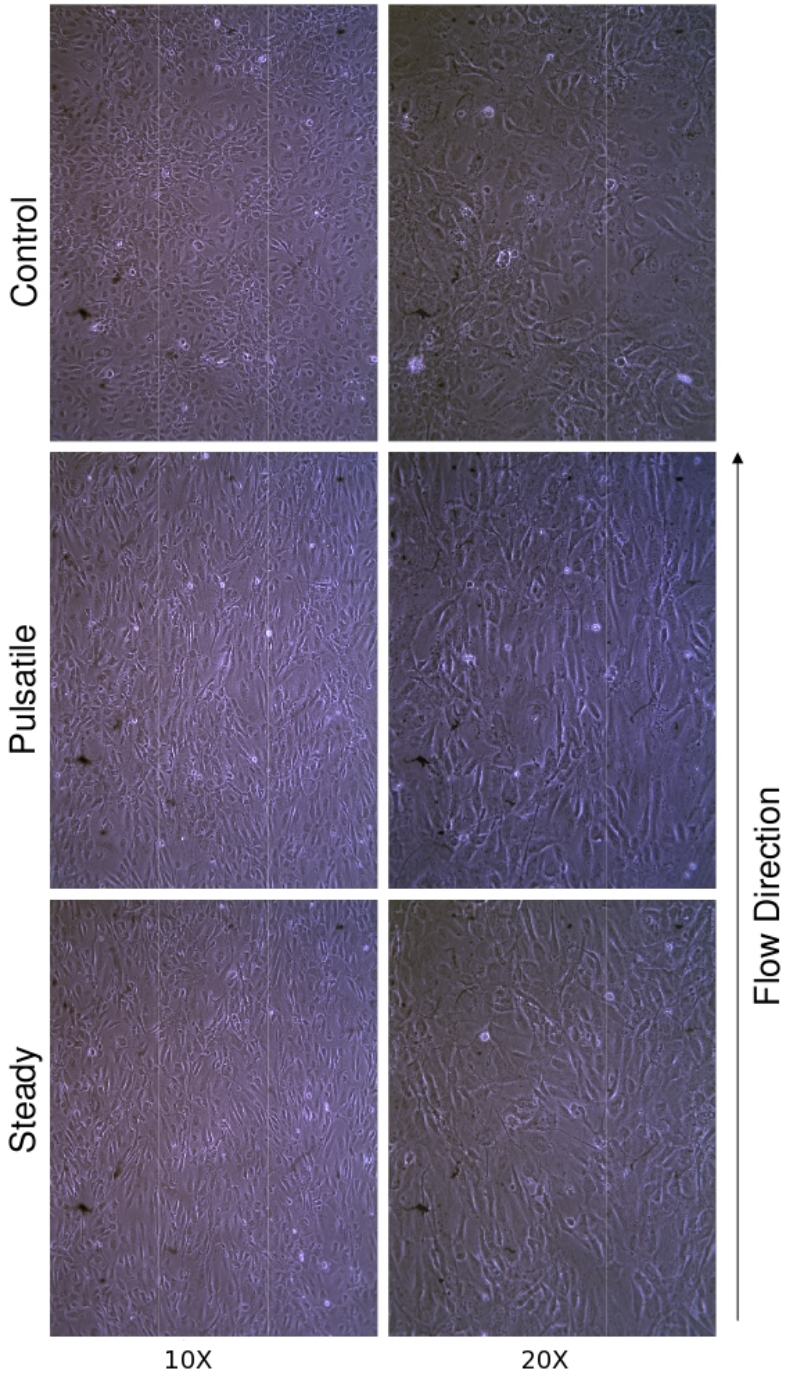

Figure 6.1: Phase contrast images of HUVECs at 10x and 20x magnification after exposure to different shear regimes for 24 hrs in a PPFC

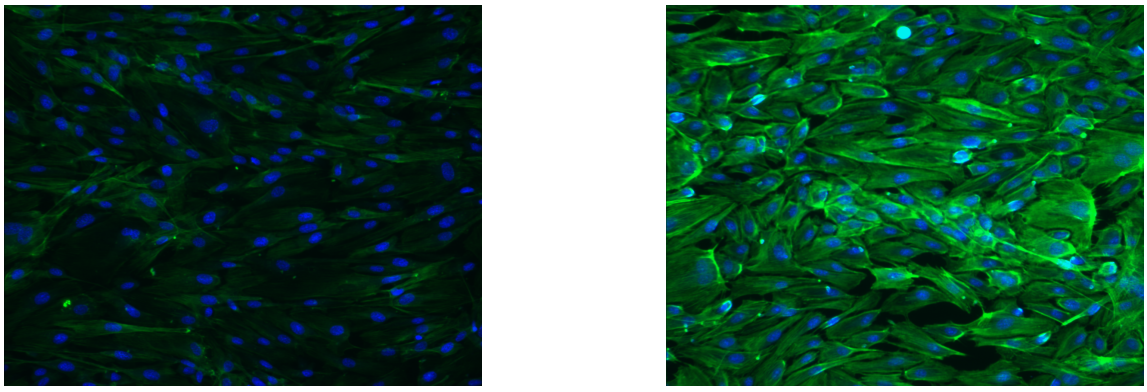

(a) Steady Flow

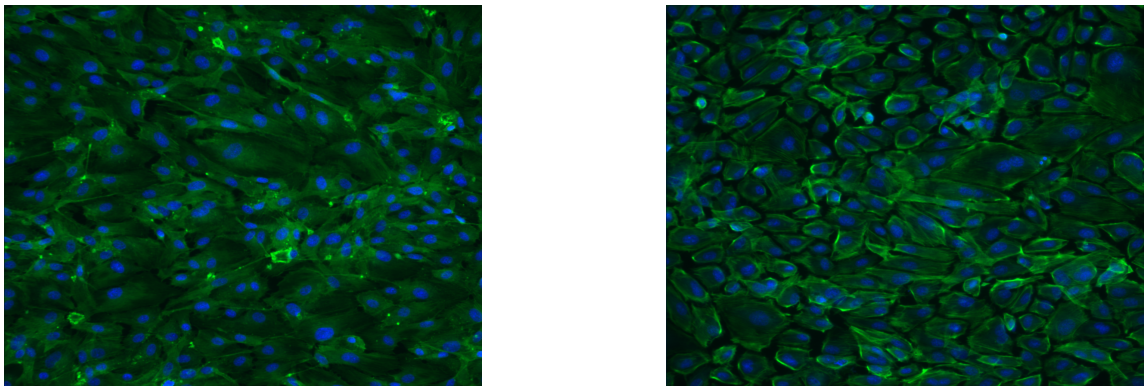

(b) Pulsatile Flow

Figure 6.2: Images of HUVECs exposed to steady and pulsatile WSS for 24hrs. Mean WSS is 1.5Pa and the pulsatile flow is defined by the LAD waveform. Direction of WSS is from left to right.

the elongation, size and orientation of the cell bodies. The segmentation programme appeared to produce an accurate segmentation result for all of the images analysed, as shown in figure 6.3. Note that the white space surrounding the images represents cells which were not included in the analysis because they were close to the edge of the

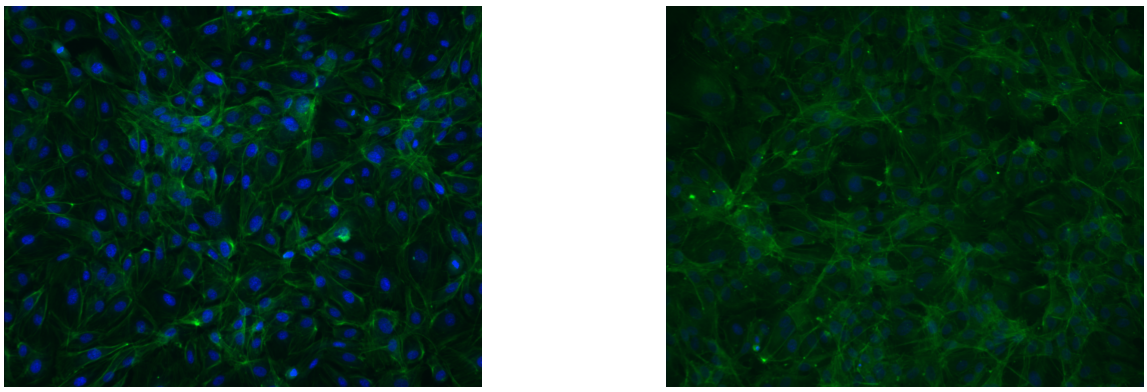

(c) Static Control

Figure 6.2: (cont.) Images of HUVECs exposed to steady and pulsatile WSS for 24hrs. Mean WSS is 1.5Pa and the pulsatile flow is defined by the LAD waveform. Direction of WSS is from left to right.

image.

Figure 6.4 shows the distribution of orientation for cells exposed to steady and pulsatile WSS and static controls, based on at least six images of HUVECs from three independent experiments. Statistically significant differences between the number of cells aligning within 10 degrees of the WSS direction are observed when comparing both steady and pulsatile WSS with the static controls. However, although slight differences in the proportion of the cells aligned within 10 degrees of the flow axis are evident when comparing steady WSS with pulsatile WSS, these differences are not statistically significant.

Although the fluid mechanical stimuli to which cells were exposed were relatively uniform within experiments, there were noticeable differences in the morphology of cells in images taken at different locations in the same experimental sample. To investigate the reason for the observed variations in morphology the average aspect ratio

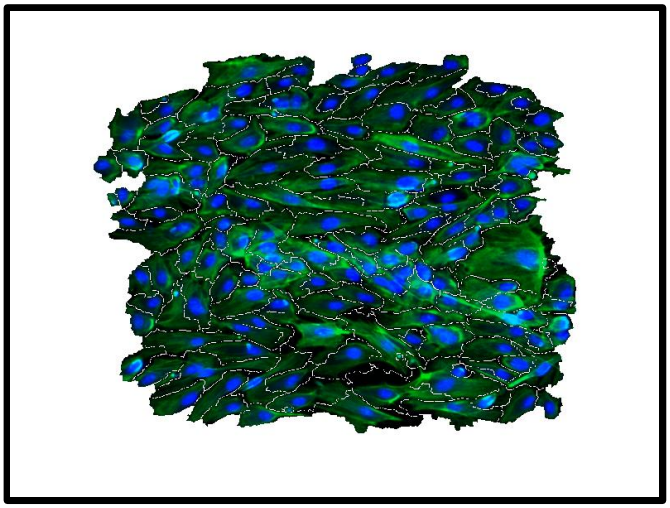

(a) Steady Flow

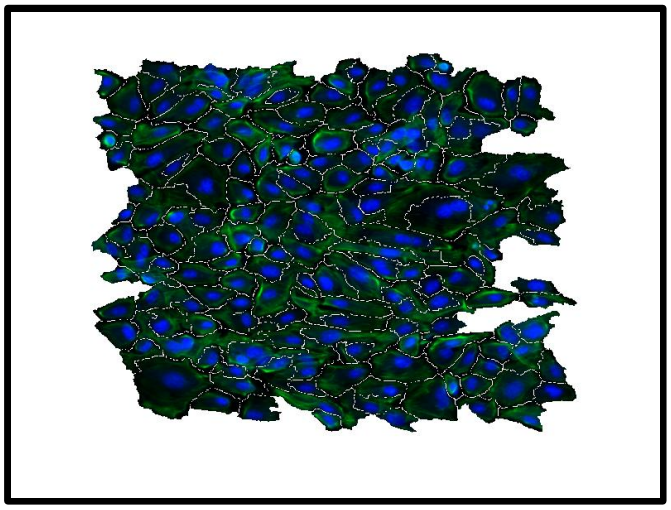

(b) Pulsatile Flow

Figure 6.3: Images of HUVECs exposed to steady and pulsatile WSS for 24hrs and segmented using the image processing routine developed in chapter 5. Mean WSS is 1.5Pa and the pulsatile flow is defined by the LAD waveform. Direction of WSS is from left to right.

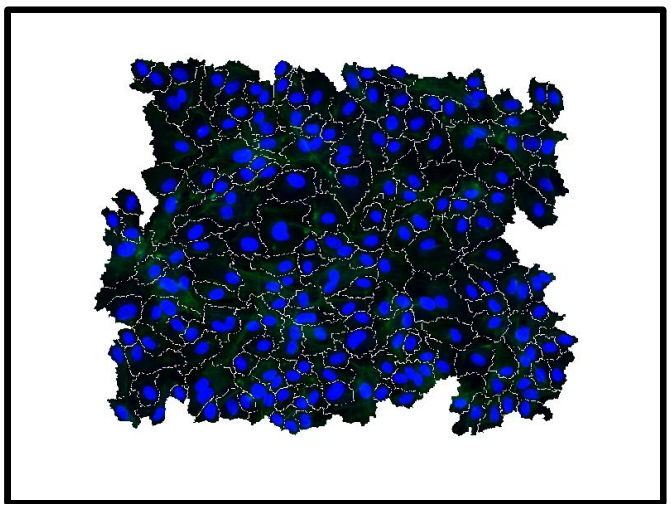

(c) Static Control

Figure 6.3: (cont.) Images of HUVECs exposed to steady and pulsatile WSS for 24hrs and segmented using the image processing routine developed in chapter 5. Mean WSS is 1.5Pa and the pulsatile flow is defined by the LAD waveform. Direction of WSS is from left to right.

and the proportion of cells aligned within +/-10 degree of the flow axis were plotted as a function of the cell density in each image for both steady and pulsatile WSS. Significant, negative correlations were observed between both the aspect ratio and the alignment and the cell density, for both steady and pulsatile WSS (both $\tau_{avg} = 1.5Pa$, LAD waveform used for pulsatile WSS, 24hrs exposure time) as shown in figure 6.5. The strength of the correlations is shown in table 6.3.1.

As discussed in chapter 5, it is also possible to use the segmentation programme for studying the morphology of nuclei, and their position within cells. Figure 6.6 shows the average distance in pixels along the flow axis between the centroid of the nucleus of HUVECs exposed to steady and pulsatile WSS, and unstimulated static control HUVECs. A schematic representation of the measurement of the distance between the

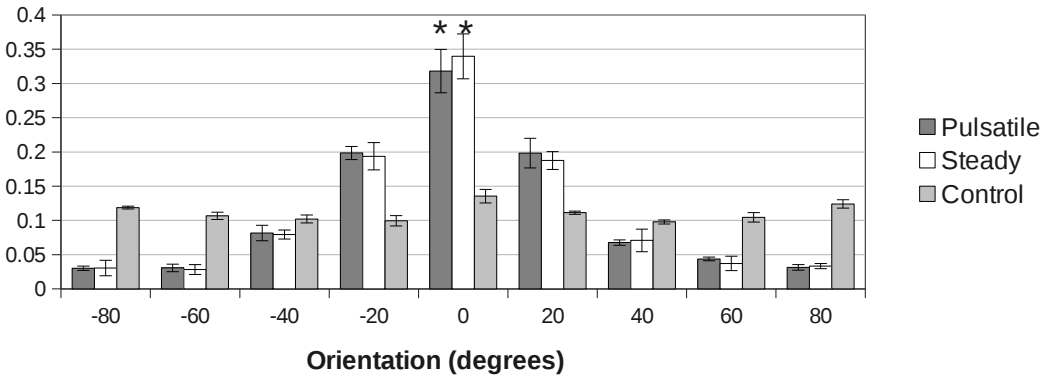

Figure 6.4: Histogram showing the orientation profiles of cells subjected to shear stress for 24hrs and quantitatively analysed using the image processing routine developed in chapter 5. * p $<$0.05 vs control, error bars show SEM of 3 samples.

Table 6.1: Strength of correlations between average cell size and morphological features of cells exposed to steady and pulsatile WSS

WSS Type	Morphological Parameter	r^2	m	p
Steady	Orientation	0.173	-2.74	0.00012
Steady	Aspect Ratio	0.568	-127.1	$<$0.00001
Pulsatile	Orientation	0.152	-2.51	0.025
Pulsatile	Aspect Ratio	0.293	-155.0	0.0011

centroid of a cell and its nucleus is shown in figure 5.2. A positive distance is defined as the centroid of the nucleus located downstream from the centroid of the entire cell. Figure 6.6 shows that nuclei located towards the downstream end of the HUVECs exposed to steady WSS, but not HUVECs exposed to pulsatile WSS or unstimulated cells.

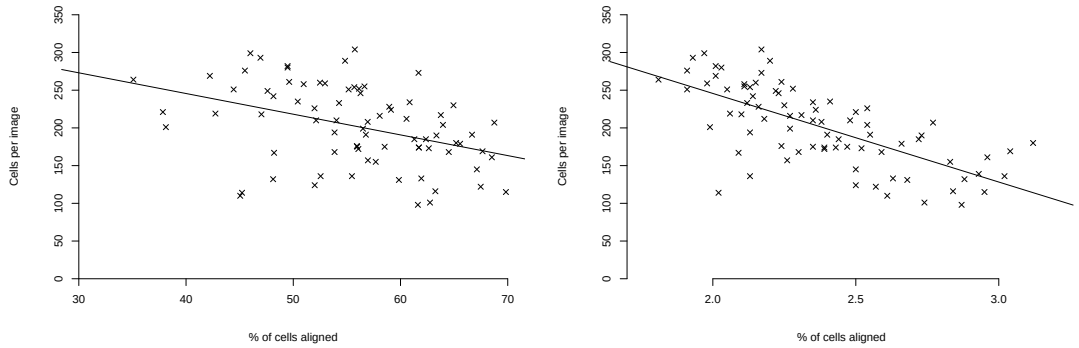

(a) Steady Flow - Orientation

(b) Steady Flow - Aspect Ratio

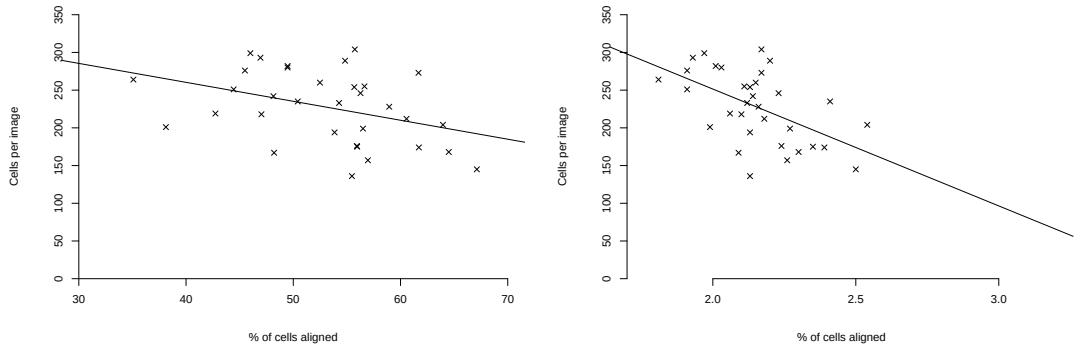

(c) Pulsatile Flow - Orientation

(d) Pulsatile Flow - Aspect Ratio

Figure 6.5: Correlation between average cell size and morphological parameters for ECs exposed to steady and pulsatile flow

6.3.2 Spatial Wall Shear Stress Gradient

Figures 6.7 - 6.9 shows images of ECs at different locations along the culture area of the converging flowchamber for both steady flow, which applied a temporally constant WSS and SWSSG in the converging section and pulsatile flow, which applied a combination of WSS, SWSSG and TWSSG in the converging section. Average WSS and SWSSG values at each location are estimated from the CFD analysis. The images show a clear realignment response for the cells exposed to combinations of WSS and

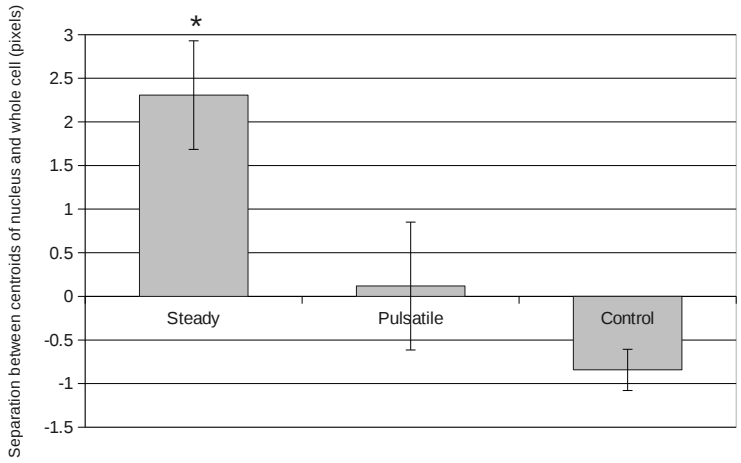

Figure 6.6: Average distance between the centroid of entire cells and their nuclei for HUVECs exposed to steady (1.5Pa), pulsatile (mean WSS = 1.5Pa, LAD waveform) and static control for 24hrs. n = 3, * $p < 0.05$ vs control, Error bars show SEM of 3 samples.

SWSSG but not in the static control cells. However, from visual inspection alone it is unclear what differences, if any, are present between cells exposed to different fluid mechanical stimuli.

The image processing programme described in chapter 5 was applied to determine the morphology of cells exposed to different WSS values within the converging flowchamber. Three images were selected from locations on the same slide that were expected to experience the same WSS value, and the average size, aspect ratio and the percentage of cells aligned within 10^o of the flow axis was determined to quantitatively analyse the effects of the variations in WSS and SWSSG throughout the flowchamber. Cells exposed to steady and pulsatile WSS as well as static controls were analysed in this way, as shown in figure 6.10.

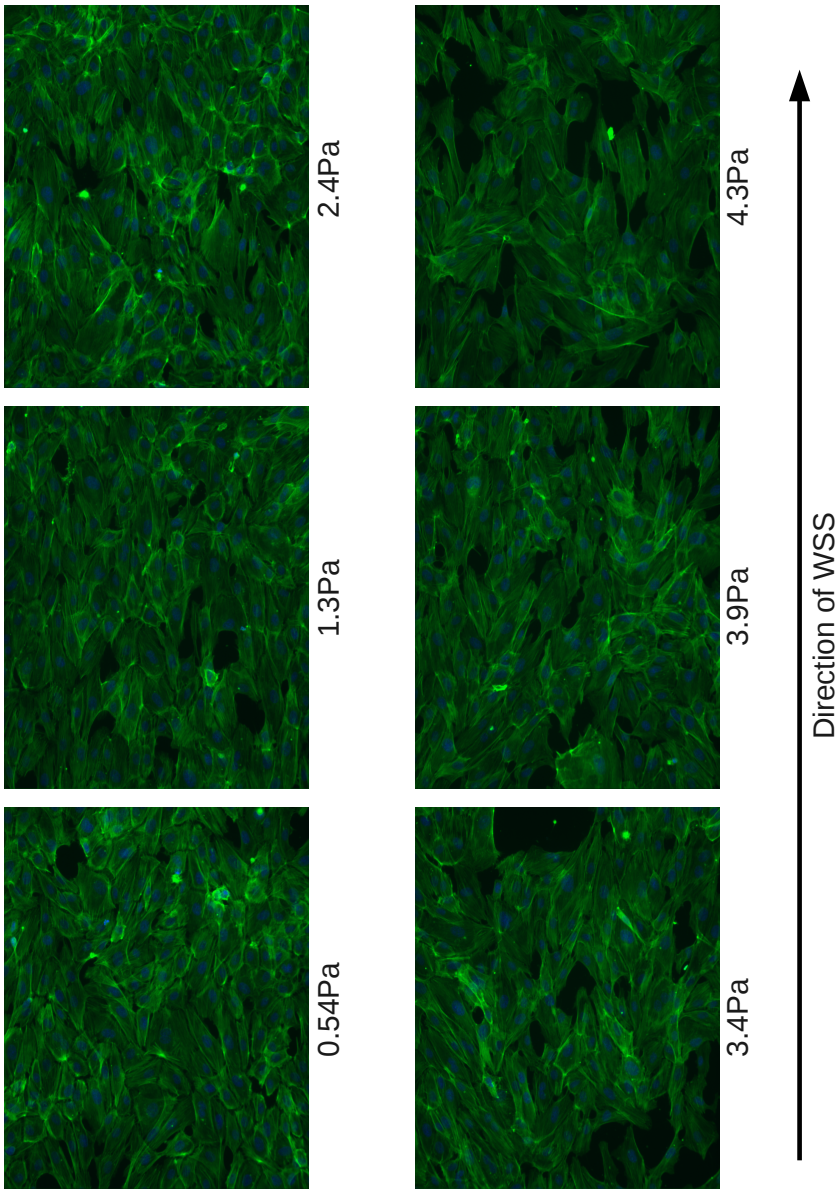

Figure 6.7: Images of HUVECs at x20 magnification after exposure to temporally steady WSS and SWSSG for 18 hrs in a converging flowchamber. Stained with DAPI and Phalloidin

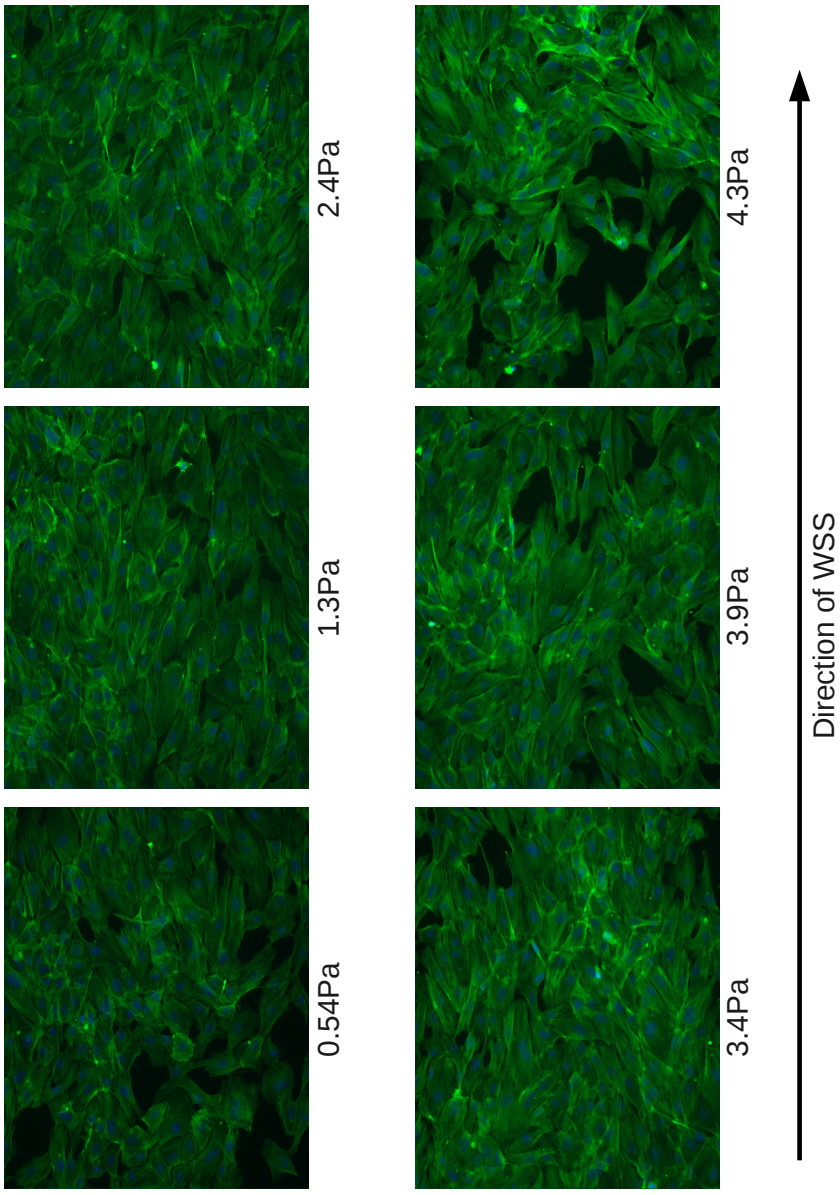

Figure 6.8: Images of HUVECs at x20 magnification after exposure to pulsatile WSS and SWSSG for 18 hrs in a converging flowchamber. Stained with DAPI and Phalloidin

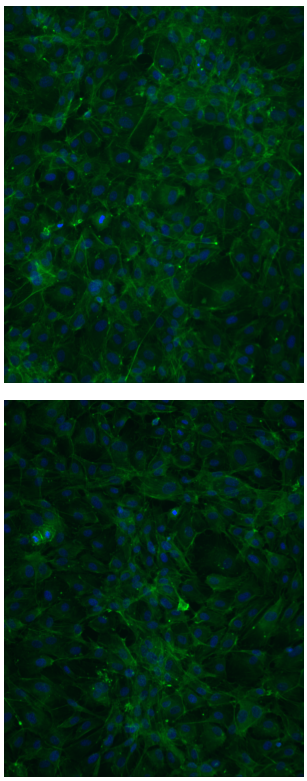

Figure 6.9: Images of static control HUVECs at x20 magnification . Stained with DAPI and Phalloidin

6.4 Discussion

The results of the steady and pulsatile flow experiments demonstrate that the F-BS is capable of supporting healthy cultures for experiment durations of at least 24 hours. The morphological changes observed in the monolayers are qualitatively similar to those observed in many previous experiments subjecting HUVECs to WSS, in which cells were observed to elongate and align in the direction of the WSS [34; 40; 58]. It is important that ECs subjected to WSS in the flow system developed for this project show qualitative agreement with those subjected to similar stimuli in other flow sys-

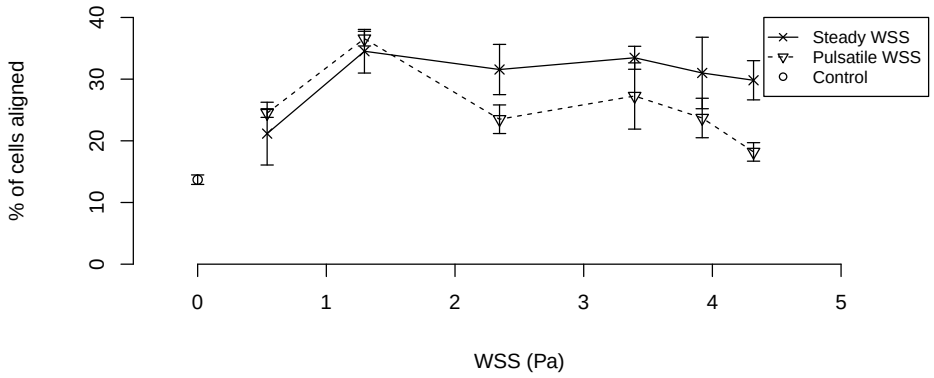

(a) Orientation

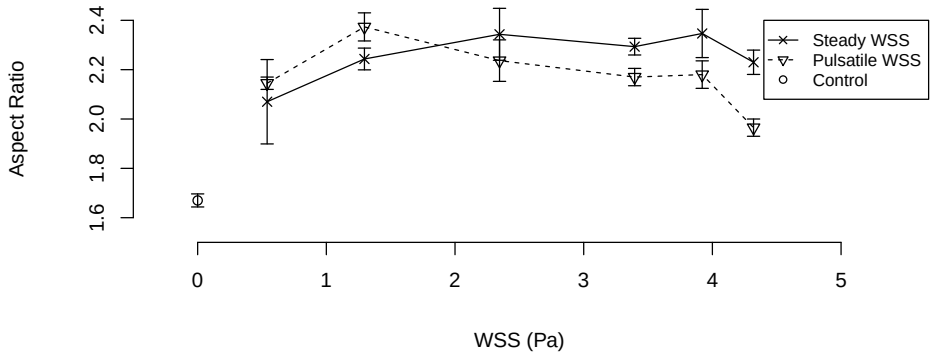

(b) Aspect Ratio

Figure 6.10: Morphological features of cells exposed to different average WSS values by pulsatile and steady flow in a converging flow chamber. n = 1. Error bars show SEM of 3 images.

tems as this suggests that the system is able to determine the normal physiological response of cultured HUVECs to WSS.

Although slight differences were evident between the response of HUVECs to pulsatile WSS defined by the LAD waveform, these differences were not significant and

may therefore be attributable to normal experimental variation. This suggests that the average magnitude of the WSS applied to cells is the main factor in determining their morphological response, in agreement with the results of Bond *et al* [14]. However, it has also been shown that pulsatile reversing and pulsatile non-reversing WSS have different effects on EC morphology [78], with pulsatile non reversing flow showing a stronger realignment relative to steady WSS whilst pulsatile reversing WSS caused a weaker morphological response than a steady WSS with and equivalent time averaged WSS. As the pulsatile flow defined by the LAD flow waveform included a small reversing component it is possible that the effect of the increased OSI due to the small reversing component and the TWSSG caused by the pulsatile flow had opposite effects, resulting in similar morphological responses being observed between the steady and pulsatile flow conditions. Further investigation into the effects of different WSS waveforms on HUVECs is therefore needed to more clearly elucidate the different effects of TWSSG, OSI and steady WSS at physiologically realistic levels on HUVEC morphology.

For HUVECs exposed to both steady and pulsatile WSS it was found that the orientation and elongation of the cells was significantly influenced by the cell density. Although all experiments were seeded at approximately the same cell density, experimental variations caused the cell density to vary both between samples and at different locations within samples. Using the image processing routine described in chapter 5 the local cell density in an image can easily be determined by computing the average cell size in the image, then taking the reciprocal of the average cell size to yield the local cell density in cells per unit area. This can be easily repeated for a large number of images to obtain a correlation between the average cell density in an image and other morphological parameters.

Investigation of the effect of cell density on the response of HUVECs to both steady WSS and physiologically realistic pulsatile WSS showed significant, negative correlations between the cell density and the alignment and elongation of HUVECs for both fluid mechanical conditions. It has been hypothesised that dense peripheral actin bands on the basal surface of ECs prevent collisions between adjacent ECs during realignment and normal cell movement [154]. This may explain why the realignment response is weaker for cells cultured more densely, as they are likely to experience more collisions between adjacent cells, slowing down the realignment process.

An alternative explanation for the observed correlation between EC realignment and cell density may be that variations in WSS within the flowchamber caused some of the cells in areas of increased WSS to detach. If this were the case then the cells remaining attached in these areas could be expected to realign more than cells at locations where WSS is lower because the realignment response of ECs has been shown to be stronger when WSS is higher [14; 78]. This would explain the co-dependence of alignment and orientation with cell size. This explanation is, however, considered to be relatively unlikely as the variations in WSS predicted by CFD analysis are very low and would not be expected to cause significant changes in the number of HUVECs detaching at areas of relatively low and relatively high WSS. This hypothesis is therefore considered relatively unlikely in the experiments in the PPFC. However, when spatial variations in WSS are experimentally introduced, as is the case for experiments performed in the converging flowchamber, the range of WSS experienced by the cells is clearly significant. The hypothesis that differences in WSS could be responsible for differences in both morphology and cell detachment, causing an artificial correlation between morphology and cell density to be observed, is therefore considered more likely in experiments performed in the converging flowchamber than those performed

in the PPFC.

It is important to take into account the correlation between cell density and morphological changes in response to WSS when interpreting the morphological response of ECs to fluid mechanical stimuli. As EC morphology has been shown to be an important marker of endothelial phenotype [159], it may also be significant when interpreting results of quantitative experiments investigating other responses of ECs to WSS.

Investigating the effect of steady and pulsatile WSS on the localisation of nuclei within HUVECs showed that the nuclei located towards the downstream end of the cells exposed to steady WSS, but not those exposed to pulsatile WSS or static control cells. This interesting difference between cells exposed to steady and pulsatile WSS may be caused by the reversing component of the LAD WSS waveform (shown in figure 2.1), which is clearly not present in the steady WSS. However, it should be noted that the average displacement of the nucleus for the cells exposed to steady WSS is relatively small. For context, the average displacement of 2.3 pixels corresponds to approximately 4.7% of the average representative radius of a cell, where the representative radius is defined as the radius of a circle having equivalent area.

Figures 6.7 - 6.10 show the response of cells to WSS at different locations in a converging flowchamber to steady and pulsatile WSS. Cells at all locations in the converging flowchamber are shown to align in the direction of flow more than cells not exposed to WSS. It appears that the realignment response is stronger for cells exposed to a shear stress in the approximate range of 1-3Pa, with the response appearing slightly weaker at lower and higher WSS values. This was the case for cells exposed to both steady and pulsatile WSS. However, it should be noted that these results represent data from images taken from different locations on individual samples exposed to each experimental condition and should therefore only be considered to give an indication of

the possible response of cells to the studied range of fluid mechanical stimuli. Furthermore, variations in the number of cells attached to the slide, caused either by normal variations in the seeding or by local variations in cell detachment caused by the variations in WSS across the slide, may have contributed to the variations in morphology observed. It can be seen from figures 6.7 - 6.8, especially in the image of cells exposed to 4.3Pa in figure 6.8, that cells have detached from small areas of the slide at higher WSS values and it is quite possible that this affects the morphology of the cells.

Figure 6.10 also shows that the realignment response is stronger in regions of the converging flowchamber where cells experience SWSSG. It is currently not possible to determine whether this stronger realignment response is due to the changes in SWSSG or WSS. However, as both Dolan [43] and Saksamoto [138] observed weaker realignment responses in cells exposed to high SWSSG it may be more likely that differences in WSS are responsible for the stronger realignment response observed in parts of the converging region. As mentioned above, it should also be noted that the data on the response of ECs in the converging flowchamber represent individual samples corresponding to each experimental condition, and should therefore only be considered as an indication of the response of ECs to the fluid mechanical stimuli. Further work is necessary to conclusively determine the response of ECs to WSS and SWSSG in the converging flowchamber.

The results observed in the converging flowchamber do, however, demonstrate the feasibility of studying the response of HUVECs to a range of pulsatile and steady WSS in combination with an approximately constant SWSSG using the converging flowchamber as a part of the F-BS.

Although direct comparison cannot be made between the results in the converging flowchamber and the PPFC due to the different timescales between the two experi-

ments, similar realignment responses were observed for the cells exposed to a mean shear of approximately 1.3Pa in the converging flowchamber and the cells exposed to 1.5Pa in the PPFC, with approximately 30% of cells aligned within 10 degrees of the flow axis in both cases.

Future work may be able to resolve the different effects of WSS and SWSSG by comparing data obtained in the PPFC to that obtained at a location in the converging flowchamber where cells are expected to experience a similar WSS value.

The results obtained using the F-BS show that it is capable of maintaining healthy cultures of HUVECs and exposing them to fluid mechanical forces for 24 hours, which is sufficiently long to induce significant realignment. This time period has also been shown to be sufficient to induce ECs to take clearly distinct phenotypes when exposed to fluid mechanical stimuli typical of atheroprotected and atheroprone locations in the human carotid bifurcation [34]. The F-BS may therefore enable future studies of EC response to various different fluid mechanical parameters which may not have been possible using previously existing systems. Although the F-BS has so far only been used for time periods of up to 24 hours, there is no reason why it could not also be used for longer durations if a particular experiment required it. Similarly, although the F-BS has only been used with HUVECs in this project, future experiments could use ECs from different vascular beds, or even non-endothelial cells if an experiment required it, simply by changing the culture medium to one appropriate for the selected cell type.

HUVECs have been widely used as a model arterial endothelium for use in studies predicting the response of ECs to stimuli predicted to either promote or prevent atherogenesis. However, it is important to note the limitations of *in vitro* models when determining the physiological response to a given stimulus as whilst these models provide convenient means for performing well controlled experiments, they necessarily

neglect a significant amount of the complexity present *in vivo*. An element of the complexity present *in vivo* which may be particularly important in determining the response of ECs to a given stimulus is the presence of other cell types, both in the arterial wall and in the circulating blood. It has been predicted that signalling cross talk between different cell types may play a significant role in determining the response of ECs [29; 102].

Another potentially important aspect of physiological systems which cannot be accurately recreated *in vitro* is that cells *in vivo* typically experience stimuli relevant to atherogenesis for timescalse of several years. It is not generally practical to perform *in vitro* cell culture experiments for timescales exceeding a few days. Experiments exposing ECs to shear stress have been performed for up to 1 week [165]. However practical considerations dictate that the majority of experiments are performed for much shorter time periods, and even one week may be considered a relatively short timescale compared to the timescales on which atherogenesis occur.

Despite these limitations, and many others, *in vitro* studies of the response of ECs to stimuli relevant to atherogenesis are still widely performed, as good agreement between results obtained in cell culture models and *in vivo* experiments investigating similar stimuli has been widely observed [163; 187].

The popularity of HUVECs for use as a model endothelium may be due to their human origin, the relative convenience of obtaining tissue for isolating cells from and the relative simplicity of the isolation procedure, which has been long established [84]. However, it must be noted that HUVECs are a non-arterial cell type and therefore the fluid mechanical environment that they experience *in vivo* is significantly different from that experienced by arterial ECs. Despite these problems, good agreement has generally been observed between the response of HUVECs and the response of ECs

of arterial origin [41; 99], although it should be noted that this agreement has been observed to be less strong when the response of human coronary arterial ECs is compared with that of HUVECs [104].

Although previous work has shown HUVECs to be a good model for arterial endothelium, it should of course be noted that no model can be considered an accurate predictor of the behaviour of cells in response to stimuli which have not previously been investigated. Therefore it is important that future work using the F-BS is combined with, and validated against, work investigating similar stimuli in different experimental models.

Chapter 7

Conclusions and Future Work

As discussed in Chapter 1, the objectives of this project can be summarised as follows:

- Develop a versatile F-BS to apply physiologically realistic WSS, T/SWSSG and OSI to cultured ECs.
- Compare CFD results obtained using LBM and FVM with experimental data to determine which method produces the closest agreement with experimental data.
- Apply the chosen CFD method to quantify the fluid mechanical environment experienced by cells within the F-BS.
- Develop a method to quantitatively analyse images of cells and determine their morphological features.
- Quantitatively analyse the morphological response of cultured ECs to different fluid mechanical stimuli.

The work directed at achieving the first objective was described in Chapter 2. This work was considered a success. The F-BS developed is capable of applying all of the desired fluid mechanical stimuli. Indeed, when a flow waveform having a reversing

component is chosen and the converging flowchamber is employed, the F-BS simultaneously applies WSS, TWSSG, SWSSG and OSI, all at approximately physiological levels. Such an experiment was demonstrated in Chapter 6. To the author's knowledge no previously existing flow system was capable of producing such a combination whilst maintaining all of the fluid mechanical parameters at approximately physiological levels.

As described in Chapter 2, the F-BS can easily control WSS in the PPFC and SWSSG in the converging flowchamber by changing the flow rate programmed into the peristaltic pump. The system can also control the OSI and TWSSG by either changing the cam used to provide the pulsatile component of the waveform or changing the size of the syringe driven by the cam system. The F-BS therefore fulfils the criteria outlined in Chapter 1.

The characteristics of the F-BS system were presented at the 2011 meeting of the Bioengineering society at Queen Mary, University of London [170].

The work directed at achieving the second objective confirmed that FVM was capable of producing results which were in agreement with experimental data. Although this was already known, the results of CFD studies have been shown to be highly operator-specific [71]. It was therefore important to validate the specific methods used to improve the confidence in the results of later CFD analyses, for which no experimental data were available. This allowed the third objective to be achieved, and an accurate quantification of the WSS environment experienced by cells cultured within the flowchambers was obtained using FVM.

The validation of LBM did not succeed in validating LBM against experimental data. Clear differences between experimental and LBM results were observed. However, this work did serve to highlight an important problem with LBM, namely that

certain lattices do not produce rotationally symmetrical results when the boundary conditions and domain are all rotationally symmetrical [171]. It was hypothesised that the unphysical results are due to insufficient velocity vectors being present on certain planes of the lattices. Further work on this hypothesis, performed by Kang *et al*, also showed that unphysical effects could be observed on planes with the fewest velocity vectors, supporting the hypothesis that the number of velocity vectors provided on certain lattices is insufficient [88]. Interestingly, the effect was only observed for wall-bounded flows and adequate results were observed on all planes when a wall was not present. This work will hopefully lead to further research into the circumstances under which different lattices produce accurate results, which may improve the suitability of LBM for simulating biological flows, among other things.

As described in Chapter 5, a segmentation programme was developed in the course of the project which can simply, accurately and repeatably determine the boundaries between ECs in confluent monolayers. This programme can then output the morphological data into Matlab for further analysis. The segmentation programme provides an enabling technology for determining the morphology of cells from stained images.

The final objective of this project was to quantitatively analyse the response of ECs to different fluid mechanical stimuli including WSS, SWSSG, TWSSG and OSI. Initial efforts to this end have been successful, and have clearly demonstrated the applicability of the enabling technologies developed for analysing the response of ECs to physiologically realistic fluid mechanical stimuli. An interesting finding was the significant correlation between the morphological response of ECs to a given fluid mechanical stimulus and the local cell density, described in Chapter 6. Initial results on the response of ECs cultured in the F-BS to fluid mechanical stimuli were presented at the 18th Congress of the European Society of Biomechanics [172] and further results

were presented at the 19th Congress of the European Society of Biomechanics [173].

The majority of the output from this project relates to enabling technologies. For this reason a significant amount of future work can be envisaged. For example, the response of ECs cultured within the F-BS has thus far only been determined in terms of morphological changes to ECs in response to WSS. However, the F-BS could be employed in experiments investigating various other responses of ECs to WSS, including responses relating to cell cycle progression such as proliferation or apoptosis, or molecular level responses, such as the expression of signalling molecules and/or pathways known to be important in either promoting or preventing atherogenesis. The segmentation programme may be useful in performing this work if cells are stained for the presence of such molecules because it could simply be modified to quantify the level of staining present in individual cells. This may be particularly important if this work investigates the effects of heterogeneous fluid mechanical environments on ECs, such as those including SWSSG, which are applied in the converging flowchamber.

As discussed in Chapter 2, the F-BS is capable of modifying the pressure experienced by ECs cultured therein and future work may therefore investigate the effects of hydrostatic pressure on EC function. The modular design of the F-BS also permits the easy incorporation flowchambers that have different geometries and hence apply different fluid mechanical environments to cells cultured therein.

Appendix A

This appendix contains the technical drawings for the flowchambers and the pulsatile pump. The groove profile for the converging flowchamber is shown in figure 1.

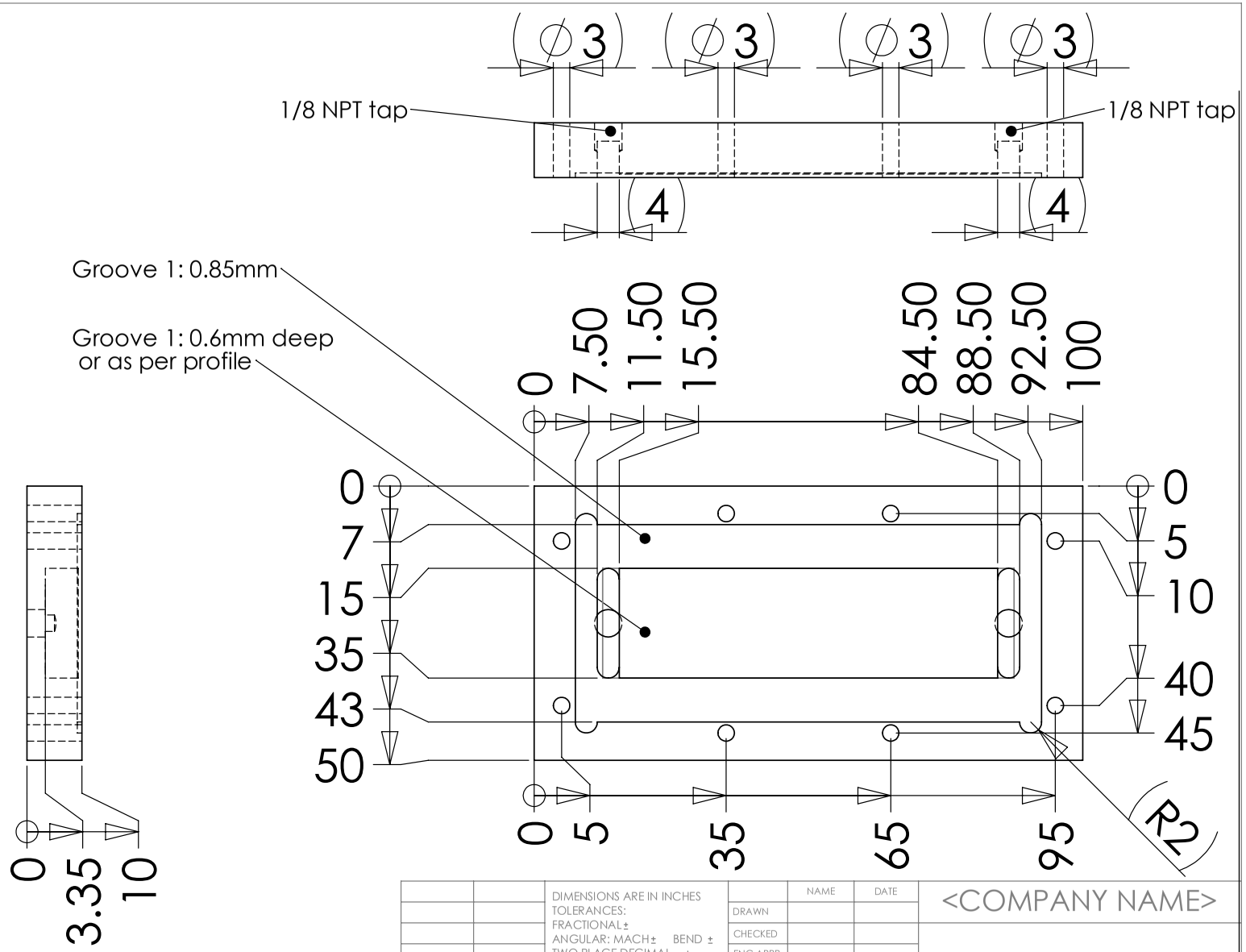

		DIMENSIONS ARE IN INCHES TOLERANCES: FRACTIONAL ± ANGULAR: MACH ± BEND ± TWO PLACE DECIMAL ± THREE PLACE DECIMAL ±		NAME	DATE
			DRAWN		
			CHECKED		
			ENG APPR.		
			MFG APPR.		
		MATERIAL --	Q.A.		
NEXT ASSY	USED ON	FINISH --	COMMENTS:		
APPLICATION		DO NOT SCALE DRAWING			

<COMPANY NAME>

SIZE	DWG. NO.	REV.
A		
SCALE:1:1	WEIGHT:	SHEET 1 OF 1

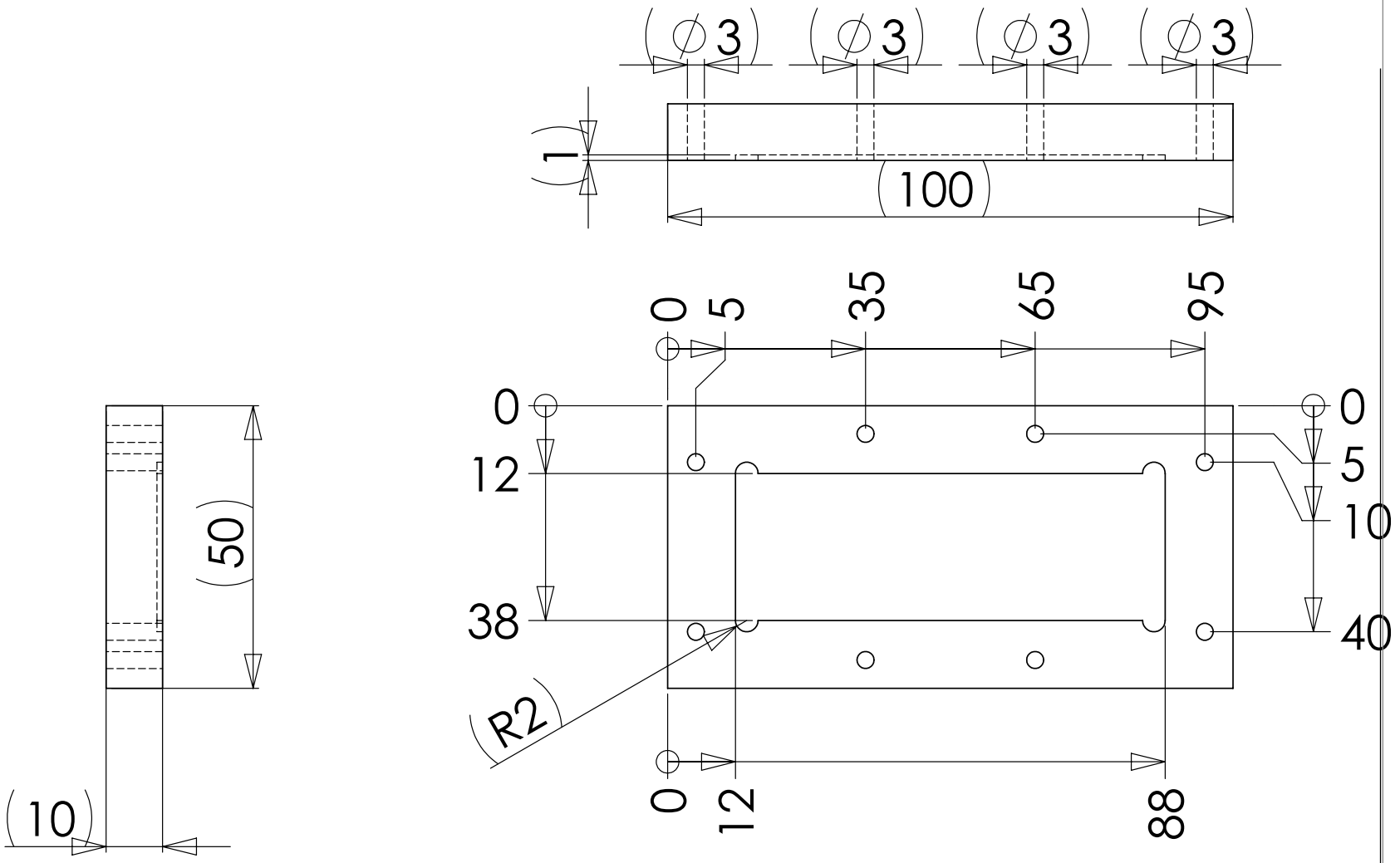

		DIMENSIONS ARE IN mm TOLERANCES: FRACTIONAL ± ANGULAR: MACH ± BEND ± TWO PLACE DECIMAL ± THREE PLACE DECIMAL ±		NAME	DATE
			DRAWN		
			CHECKED		
			ENG APPR.		
			MFG APPR.		
		MATERIAL LEXAN	Q.A.		
NEXT ASSY	USED ON	FINISH --	COMMENTS:		
APPLICATION		DO NOT SCALE DRAWING			

<COMPANY NAME>

SIZE	DWG. NO.	REV.
A		
SCALE:1:1	WEIGHT:	SHEET 1 OF 1

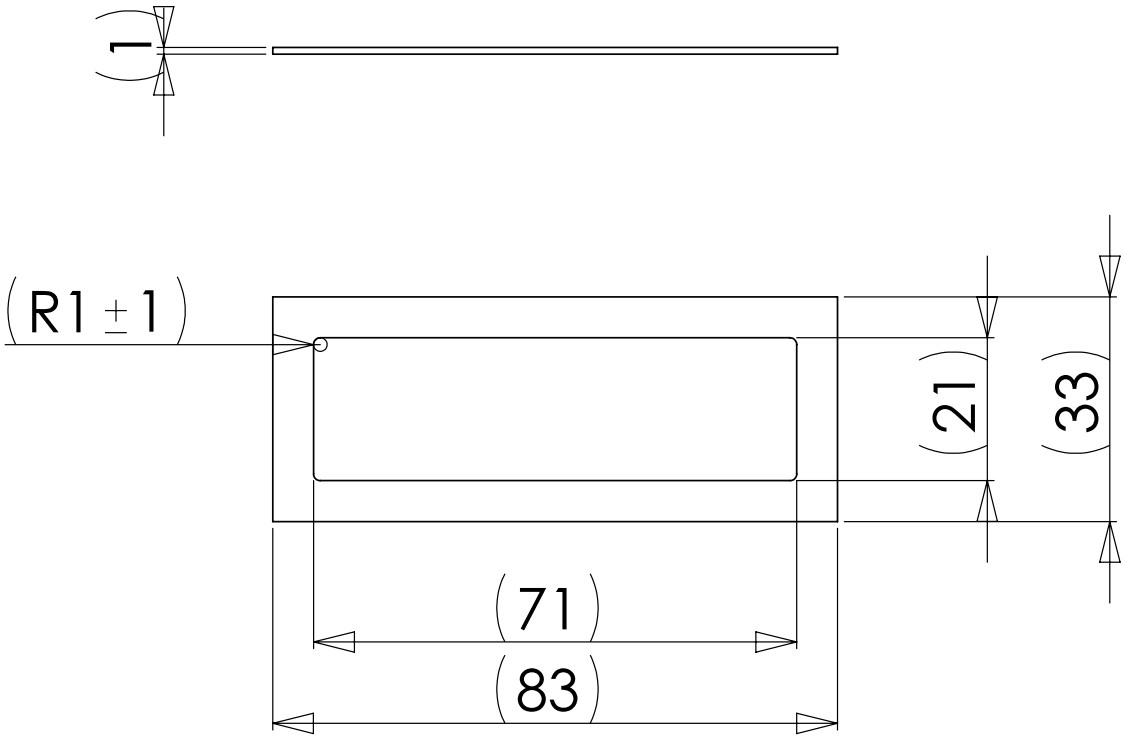

		DIMENSIONS ARE IN INCHES TOLERANCES: FRACTIONAL ± ANGULAR: MACH ± BEND ± TWO PLACE DECIMAL ± THREE PLACE DECIMAL ±		NAME	DATE
			DRAWN		
			CHECKED		
			ENG APPR.		
			MFG APPR.		
		MATERIAL --	Q.A.		
NEXT ASSY	USED ON	FINISH --	COMMENTS:		
APPLICATION		DO NOT SCALE DRAWING			

<COMPANY NAME>

SIZE	DWG. NO.	REV.
A		
SCALE:1:1	WEIGHT:	SHEET 1 OF 1

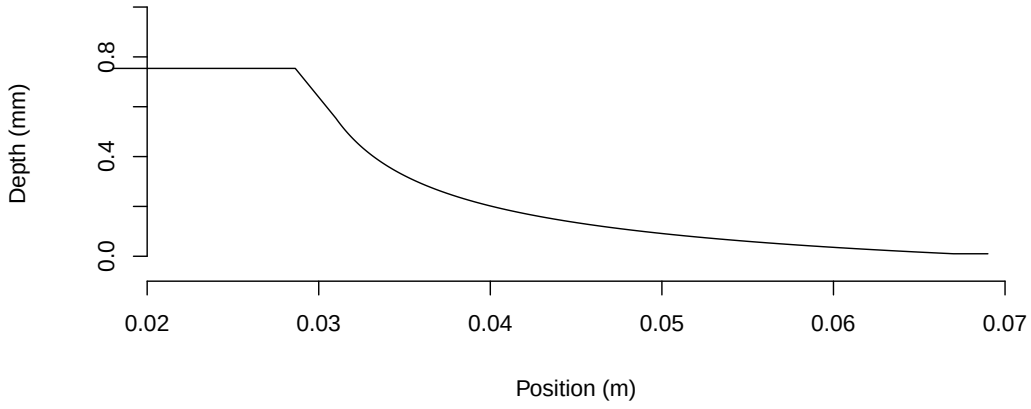

Figure 1: Groove profile for the converging flowchamber

Appendix B

This appendix contains the Matlab code for the segmentation script described in chapter 5.

```
function [Orientation Aspects Area L] = SegmentationGreenBlueNew(a)
% Segmentation script for images of confluent monolayers of cells
% stained with DAPI and Phalloidin (or similar)
% Authors: Alex White, Bernadette Deere and Chuh Chong

% 1) Read the image, separate the green and blue matrices and
% remove background staining.
J = imread(a);
% preprocessing blue
J_B=J(:,:,3);
background_B = imopen(J_B,strel('disk',75));
J_B2 = J_B - background_B;
% preprocessing green
J_G=J(:,:,2);
background_G = imopen(J_G,strel('disk',75));
J_G2 = J_G - background_G;
% Create enhanced Image
I = cat(3,J(:,:,1),J_G2,2*J_B2);
% Add green and blue matrices to create greyscale image
I_GB = imadd(J_G2,J_B2);
% Enhance Image
I_GB1=adapthisteq(I_GB);
I_GB2=imadjust(I_GB1);

% 2) Nucleus Segmentation
I_eq = 2*J_B2;
mask_em = imextendedmax(I_eq, 100);
mask_em = imclose(mask_em, ones(5,5));
mask_em = bwareaopen(mask_em, 10);

% 3) Watershed Transform
I_C = imcomplement(I_GB2);
% Invert the greyscale image of the combined blue and green matrices.
I_mod = imimposemin(I_C, mask_em);
% Ensure that minima are only at the defined markers
L = watershed(I_mod);
stats = regionprops(L,'Orientation', 'Area','BoundingBox',...
    'PixelIdxList');

% 4) Remove cells which have pixels on the edges of the image
CellNumber = length(cat(1,stats.Area));
BB = cat(1,stats.BoundingBox);
k=0;
l=zeros(1,CellNumber);
for x = 1:CellNumber
    if BB(x,1) < 50
        else if BB(x,2) < 50
            else if (BB(x,3) + BB(x,1)) > (length(I_GB(1,:))-50)
                else if (BB(x,4) + BB(x,2)) > (length(I_GB(:,1)) - 50)
```

```
                    else
                        k = k + 1;
                        l(x) = x;
                end
            end
        end
    end
end
for i=1:CellNumber
    ith_object_idx_list = stats(i).PixelIdxList;
    L(ith_object_idx_list) = l(i);
end
stats2 = regionprops(L,'Orientation', 'MajorAxisLength',...
    'MinorAxisLength','Area');
figure,imshow(label2rgb(L,'spring','c','shuffle')),...
    title('Watershed Transform')

% 5) Compute morphological parameters
MajLength= cat(1,stats2.MajorAxisLength);
MinLength = cat(1,stats2.MinorAxisLength);
Aspects = MajLength./MinLength;
Orientation = cat(1, stats2.Orientation);
Area = cat(1, stats2.Area);

% 6) Show segmentation boundaries overlaid on original image
Lthresh =imcomplement( im2bw(L,0.000000001));
I_overlay = imoverlay(I, Lthresh);
figure, imshow(I_overlay)
```

References

[1] S. AKIMOTO, M. MITSUMATA, T. SASAGURI, AND Y. YOSHIDA. Laminar shear stress inhibits vascular endothelial cell proliferation by inducing cyclin-dependent kinase inhibitor p21$^{Sdi1/Cip1/Waf1}$. *Circulation research*, **86**[2]:185–190, 2000. 18

[2] F. ALI, M. ZAKKAR, K. KARU, E. A. LIDINGTON, S. S. HAMDULAY, J. J. BOYLE, M. ZLOH, A. BAUER, D. O. HANSKARD, P. C. EVANS, AND J. C. MASON. Induction of the cytoprotective enzyme Heme Oxygenase-1 by statins is enhanced in vascular endothelium exposed to laminar shear stress and impaired by disturbed flow. *The Journal of Biological Chemistry*, **284**[28]:18882 – 18892, 2009. 19, 25

[3] S. ANSUMALI, I. V. KARLIN, AND H. C. ÖTTINGER. Minimal entropic kinetic models for hydrodynamics. *Europhysics Letters*, **63**[6]:798–804, 2003. 96

[4] T. ASAKURA AND T. KARINO. Flow patterns and spatial distribution of atherosclerotic lesions in human coronary arteries. *Circulation research*, **66**[4]:1045–1066, 1990. 9

[5] A. D. AUGST, B. ARIFF, S. A. THOM, X. Y. XU, AND A. D. HUGHES. Analysis of complex flow and the relationship between blood pressure, wall

shear stress, and intima-media thickness in the human carotid artery. *American Journal of Physiology: Heart and Circulatory Physiology*, **293**:H1031–H1037, 2007. 11

[6] X. BAO, C. B. CLARK, AND J. A. FRANGOS. Temporal gradient in shear-induced signaling pathway: involvement of MAP kinase, c-fos, and connexin43. *American Journal of Physiology-Heart and Circulatory Physiology*, **278**[5]:H1598 – H1605, 2000. 22

[7] X. BAO, C. LU, AND J.A. FRANGOS. Mechanism of temporal gradients in shear-induced ERK1/2 activation and proliferation in endothelial cells. *American Journal of Physiology: Heart and Circulatory Physiology*, **103**:H22 – H29, 2001. 22, 29

[8] N. BERGH, M. EKMAN, E. ULFHAMMER, M. ANDERSSON, L. KARLSSON, AND S. JERN. A new biomechanical perfusion system for ex vivo study of small biological intact vessels. *Annals of Biomedical Engineering*, **33**[12]:1808–1818, 2005. 26, 34, 35, 46, 67, 69

[9] N. BERGH, E. ULFHAMMER, K. GLISE, S. JERN, AND L. KARLSSON. Influence of TNF-α and biomechanical stress on endothelial anti- and prothrombotic genes. *Biochemical and Biophysical Research Communications*, **385**[3]:314–318, 2009. 21, 34, 46, 47

[10] P. L. BHATNAGAR, E. P. GROSS, AND M. KROOK. A model for collision processes in gases. I. Small amplitude processes in charged and neutral One-Component systems. *Physical Review*, **94**[3]:511–525, 1954. 78

[11] B. R. BLACKMAN, K. A. BARBEE, AND L. E. THIABAULT. In vitro cell shearing device to investigate the dynamic response of cells in a controlled hydrodynamic environment. *Annals of Biomedical Engineering*, **28**:363 – 372, 2000. 26, 33

[12] B.R. BLACKMAN, G. GARCA-CARDEA, AND M.A. GIMBRONE. A new in vitro model to evaluate differential responses of endothelial cells to simulated arterial shear stress waveforms. *Journal of Biomechanical Engineering*, **124**[4]:397–407, 2002. 33

[13] L. BOLTZMANN. Lectures on gas theory, translated by S brush. *(University of California, Berkeley, 1964)*, 1964. 74

[14] A.R. BOND, S. IFTIKHAR, A.A. BHARATH, AND P.D. WEINBERG. Morphological evidence for a change in the pattern of aortic wall shear stress with age. *Arteriosclerosis, Thrombosis and Vascular Biology*, **31**:543 – 550, 2011. 14, 17, 142, 143, 160, 161

[15] L. T. BREEN, P. E. MCHUGH, B. A. MCCORMACK, G. MUIR, N. J. QUINLAN, K. B. HERATY, AND B. P. MURPHY. Development of a novel bioreactor to apply shear stress and tensile strain simultaneously to cell monolayers. *Review of Scientific Instruments*, **77**[10]:104301, 2006. 27, 33, 35

[16] L.T. BREEN, P.E. MCHUGH, AND B.P. MURPHY. HUVEC ICAM-1 and VCAM-1 synthesis in response to potentially athero-prone and athero-protective mechanical and nicotine chemical stimuli. *Annals of Biomedical Engineering*, **38**[5]:1880–1892, 2010. 21, 24, 39, 45, 67, 143

[17] J. R. CALVERT AND R. A. FARRAR. *An engineering data book.* Palgrave, 1999. 59, 65

[18] C. G. CARO, J. M. FITZ-GERALD, AND R. C. SCHROTER. Atheroma and arterial wall shear observation, correlation and proposal of a shear dependent mass transfer mechanism for atherogenesis. *Proceedings of the Royal Society of London. Series B, Biological Sciences*, **177**[1046]:109–133, 1971. 6, 7, 13, 15

[19] C. G. CARO, J. M. FITZGERALD, AND R. C. SCHROTER. Arterial wall shear and distribution of early atheroma in man. *Nature*, **223**[5211]:1159 – 1161, 1969. 6, 7

[20] A. CHAKRABORTY, S. CHAKRABORTY, V. R. JALA, B. HARIBABU, M. K. SHARP, AND R. E. BERSON. Effects of biaxial oscillatory shear stress on endothelial cell proliferation and morphology. *Biotechnology and Bioengineering*, **109**:695–707, 2012. 12

[21] C. CHANG, C. H. LIU, AND C. A. LIN. Boundary conditions for lattice Boltzmann simulations with complex geometry flows. *Computers and Mathematics with Applications*, **58**[5]:940–949, 2009. 102

[22] L. CHAU, M. DORAN, AND J. COOPER-WHITE. A novel multishear microdevice for studying cell mechanics. *Lab on a Chip*, **9**:1897 –1902, 2009. 27, 28

[23] S. CHEN AND G. D. DOOLEN. Lattice Boltzmann method for fluid flows. *Annual Review of Fluid Mechanics*, **30**[1]:329–364, 1998. 78, 80

[24] C. CHENG, D. TEMPEL, R. VAN HAPEREN, A. VAN DER BAAN, F. GROSVELD, M.J.A.P. DAEMEN, R. KRAMS, AND R. DE CROM. Atherosclerotic lesion size and vulnerability are determined by patterns of fluid shear stress. *Circulation*, **113**:2744 – 2753, 2006. 10, 15, 24

[25] J.-J. CHENG, B.-S. WUNG, Y.-J. CHAO, AND D. L. WANG. Cyclic strain enhances adhesion of monocytes to endothelial cells by increasing intercellular adhesion molecule-1 expression. *Hypertension*, **28**[3]:386–391, 1996. 24

[26] D. CHETWYND, K. WORDEN, AND G. MANSON. An application of interval valued neural networks to a regression problem. *Proceedings of the Royal Society of London Part A*, **462**[2074]:3097–3114, 2006. 60

[27] S. CHIEN. Mechanotransduction and endothelial cell homeostasis: the wisdom of the cell. *American Journal of Physiology-Heart and Circulatory Physiology*, **101**[47]:16483 – 16488, 2004. 15

[28] S. S. CHIKATAMARLA, C. E. FROUZAKIS, I. V. KARLIN, A. G. TOMBOULIDES, AND K. B. BOULOUCHOS. Lattice Boltzmann method for direct numerical simulation of turbulent flows. *Journal of Fluid Mechanics*, **656**:298–308, 2010. 75, 102

[29] J. J. CHIU, L. J. CHEN, AND C. N. CHEN ET AL. A model for studying the effect of shear stress on interactions between vascular endothelial cells and smooth muscle cells. *Journal of Biomechanics*, **37**[4]:531 – 539, 2004. 165

[30] J.-J. CHIU AND S. CHIEN. Effects of disturbed flow on vascular endothelium: Pathophysiological basis and clinical perspectives. *Physiological Reviews*, **91**[1]:327–387, 2011. 7, 15, 16, 17, 24, 40

[31] B. S. CONKLIN, S. M. SUROWIEC, P. H. LIN, AND C. CHEN. A simple physiologic pulsatile perfusion system for the study of intact vascular tissue. *Medical Engineering & Physics*, **22**[6]:441–449, 2000. 26, 34, 46, 47, 66, 69

[32] J. P. COOKE, E. ROSSITCH, N. A. ANDON, J. LOSCALZO, AND V. J. DZAU. Flow activates an endothelial potassium channel to release an endogenous nitrovasodilator. *Journal of Clinical Investigation*, **88**:1663 – 1671, 1991. 17, 18

[33] M. H. CRIQUI, A. FRONEK, E. BARRETT-CONNOR, M. R. KLAUBER, S. GABRIEL, AND D. GOODMAN. The prevalence of peripheral arterial disease in a defined population. *Circulation*, **71**[3]:510–515, 1985. 10

[34] G. DAI, M. R. KAAZEMPUR-MOFRAD, S. NATARAJAN, Y. ZHANG, S. VAUGHN, B. R. BLACKMAN, R. D. KAMM, G. GARCA-CARDEA, AND M. A. GIMBRONE. Distinct endothelial phenotypes evoked by arterial waveforms derived from atherosclerosis-susceptible and -resistant regions of human vasculature. *Proceedings of the National Academy of Sciences of the United States of America*, **101**[41]:14871–14876, 2004. x, 13, 21, 45, 50, 62, 70, 143, 158, 164

[35] A. DARDIK, L. CHEN, J. FRATTINI, H. ASADA, F. AZIZ, F. A. KUDO, AND B. E. SUMPIO. Differential effects of laminar and orbital shear stress on endothelial cells. *Journal of Vascular Surgery*, **41**[5]:869 – 880, 2005. 27, 31

[36] P. F. DAVIES. Flow-mediated endothelial mechanotranduction. *Physiological Review*, **75**[3]:519 – 560, 1995. 3

[37] P. F. DAVIES, A. REMUZZA, E. J. GORDON, C. F. DEWEY, AND M. A. GIMBRONE. Turbulent fluid shear stress induces vasclar endothelial cell turnover in vitro. *Proceedings of the National Academy of Sciences of the United States of America*, **83**:713 – 726, 1996. 20

[38] R. J. DEKKER, S. VAN SOEST, R. D. FONTJIN, S. SALAMANCA, P. G. DE GROOT, E. VANBAVEL, H.PANNEKOEK, AND A. J. G. HORREVOETS. Prolonged fluid shear stress induces a distinct set of endothelial cell genes, most specifically lung kruppel-like factor (KLF2). *Blood*, **100**:1689 – 1698, 2002. 17

[39] P. J. DELLAR. Lattice kinetic schemes for magnetohydrodynamics. *Journal of Computational Physics*, **179**:95–126, 2002. 72

[40] C.F. DEWEY, S. R. BUSSOLARI, M. A. GIMBRONE, AND P. F. DAVIES. The dynamic response of endothelial cells to fluid shear stress. *Journal of Biomechanical Engineering*, **103**:177 – 185, 1981. 17, 28, 33, 158

[41] C. F. DEWEY JR. Effects of fluid flow on living vascular cells. *Journal of biomechanical engineering*, **106**[1]:31, 1984. 166

[42] D. D'HUMIÉRES, I. GINZBURG, M. KRAFCZYK, P. LALLEMAND, AND L.-S. LUO. Multiple-relaxation-time lattice Boltzmann models in three dimensions. *Philosophical Transactions of the Royal Society A*, **360**[1792]:437–451, 2002. 79

[43] J. DOLAN, H. MENG, S. SINGH, R. PALUCH, AND J. KOLEGA. High fluid shear stress and spatial shear stress gradients affect endothelial proliferation, survival, and alignment. *Annals of Biomedical Engineering*, **39**:1620–1631, 2011. 23, 27, 30, 46, 49, 68, 105, 106, 121, 144, 163

[44] M. A. VAN DOORMAAL AND C. R. ETHIER. Design and optimisation of a novel heilcal endothelial cell culture device. *Biomechanics and Modelling in Mechanobiology*, **9**:523 – 531, 2010. 27, 39

[45] M. S. EL-KURDI, J. S. VIPPERMAN, AND D. A. VORP. Control of circumferential wall stress and luminal shear stress within intact vascular segments perfused ex vivo. *Journal of Biomechanical Engineering*, **130**[5]:051003, 2008. 27, 34, 46, 47, 67, 69

[46] M. S. EL-KURDI, J. S. VIPPERMAN, AND D. A. VORP. Design and subspace system identification of an ex vivo vascular perfusion system. *Journal of Biomechanical Engineering*, **131**[4]:041012–8, 2009. 27, 34, 46, 47

[47] S. G. ESKIN, C. L. IVES, L. V. MCINTIRE, AND L. T. NAVARRO. Response of cultured endothelial cells to steady flow. *Microvascular research*, **28**[1]:87–94, 1984. 123

[48] R. ESTRADA, G. A. GIRIDHARAN, M.-D. NGUYEN, T. J. ROUSSEL, M. SHAKERI, V. PARICHEHREH, S. D. PRABHU, AND P. SETHU. Endothelial cell culture model for replication of physiological profiles of pressure, flow, stretch, and shear stress in vitro. *Analytical Chemistry*, **83**[8]:3170–3177, 2011. 27, 35, 48, 67, 69

[49] M. A. FARCAS, L. ROULEAU, R. FRASER, AND R. L. LEASK. The development of 3-D, in vitro, endothelial culture models for the study of coronary artery disease. *Biomedical engineering online*, **8**[1]:30, 2009. 27, 31, 46, 68

[50] R. K. FISHER, T. V. HOW, T. CARPENTER, J. A. BRENNAN, AND P. L. HARRIS. Optimising miller cuff dimensions. the influence of geometry on anasto-

motic flow patterns. *European Journal of Vascular and Endovascular Surgery*, **21**[3]:251 – 260, 2001. 50, 70

[51] M. D. FORD, H. N. NIKOLOV, J. S. MILNER, S. P. LOWNIE, E. M. DEMONT, W. KALATA, F. LOTH, D. W. HOLDSWORTH, AND D. A. STEINMAN. Piv-measured versus CFD-predicted flow dynamics in anatomically realistic cerebral aneurysm models. *Journal of biomechanical engineering*, **130**:021015, 2008. 39

[52] G. FOTEINOS, Y. HU, Q. XIAO, B. METZLER, AND Q. XU. Rapid endothelial cell turnover at atherosclerosis-prone areas coincides with stem cell repair in apolipoprotien e -deficient mice. *Circulation*, **117**:1856 – 1863, 2008. 18

[53] J. A. FRANGOS, L. V. MCINTIRE, AND S. G. ESKIN. Shear stress induced stimulation of mammalian cell metabolism. *Biotechnology and Bioengineering*, **32**:1053 – 1060, 1988. 26, 28, 36, 105, 121

[54] R. P. FRANKE, M. GRÄFE, H. SCHNITTLER, D. SEIFFGE, C. MITTERMAYER, AND D. DRENCKHAHN. Induction of human vascular endothelial stress fibres by fluid shear stress. *Nature*, 1984. 17, 142

[55] M. H. FRIEDMAN, O. J. DETERS, F. F. MARK, C. B. BARGERON, AND G. M. HUTCHINS. Arterial geometry affects hemodynamics: a potential risk factor for atherosclerosis. *Atherosclerosis*, **46**[2]:225–231, 1983. 10

[56] U. FRISCH, B. HASSLACHER, AND Y. POMEAU. Lattice-Gas automata for the Navier-Stokes equation. *Physical Review Letters*, **56**[14]:1505–1508, 1986. 98

[57] D. L. FRY. Certain chemorheologic considerations regarding the blood vascular interface with particular reference to coronary artery disease. *Circulation*, **40**[IV]:38–57, 1969. 6, 7

[58] C.G. GALBRAITH, R. SKALAK, AND S. CHIEN. Shear stress induces spatial reorganisation of the endothelial cell cytoskeleton. *Cell Motility and the Cytoskeleton*, **40**:317 – 330, 1998. 17, 142, 158

[59] G. GARCIA-CARDENA, J. COMANDER, K.R. ANDERSON, B.R. BLACKMAN, AND M.A. GIMBRONE. Biomechanical actaivation of vascular endothelium as a determinant of its functional phenotype. *Proceedings of the National Academy of Sciences of the United States of America*, **98**:4478 – 4485, 2001. 20

[60] C. M. GIBSON, L. DÍAZ, K. KANDARPA, F. M. SACKS, R. C. PASTERNAK, T. SANDOR, C. FELDMAN, AND P. H. STONE. Relation of vessel wall shear stress to atherosclerosis progression in human coronary arteries. *Arteriosclerosis, Thrombosis, and Vascular Biology*, **13**[2]:310–315, 1993. 9

[61] F. J. GIJSEN, J. J. WENTZEL, A. THURY, B. LAMERS, J. C. SCHUURBIERS, AND SERRUYS P. W. A new imaging technique to study 3-D plaque and shear stress distribution in human coronary artery bifurcations in vivo. *Journal of Biomechanics*, **40**:2349–2357, 2007. 11

[62] M. A. GIMBRONE AND G. GARCIA-CARDENA. Vascular endothelium, hemodynamics, and the pathobiology of atherosclerosis. *Cardiovascular Pathology*, **22**:9 – 15, 2013. 19

[63] S. GLAGOV, C. ZARINS, D.P. GIDDENS, AND D.N. KU. Hemodynamics and atherosclerosis. Insights and perspectives gained from studies of human arteries. *Archives of Pathology and Laboratory Medicine*, **112**[10]:1018–1031, 1988. 6

[64] V. GRAU, A. U. J. MEWES, M. ALCANIZ, R. KIKINIS, AND S. K. WARFIELD. Improved watershed transform for medical image segmentation using prior information. *Medical Imaging, IEEE Transactions on*, **23**[4]:447–458, 2004. 124, 138

[65] Z. GUO AND T. S. ZHAO. Lattice Boltzmann model for incompressible flows through porous media. *Physical Review E*, **66**[3]:036304, 2002. 72

[66] C. HAHN AND M. A. SCHWARTZ. Mechanotransduction in vascular physiology and atherogenesis. *Nature Reviews*, **10**:53 – 62, 2009. 15

[67] M. S. HAHN, M. K. MCHALE, E. WANG, R. H. SCHMEDLEN, AND J. L. WEST. Physiologic pulsatile flow bioreactor conditioning of Poly(ethylene glycol)-based tissue engineered vascular grafts. *Annals of Biomedical Engineering*, **35**[2]:190 – 200, 2006. 34, 46

[68] G. K. HANSSON. Inflammation, atherosclerosis and coronary artery disease. *New England Journal of Medicine*, **352**:1685 –1695, 2005. 4

[69] G. K. HANSSON. Mechanisms of thrombus formation. *New England Journal of Medicine*, **35**:938 – 949, 2008. 5

[70] J. HARDY, Y. POMEAU, AND O. DE PAZZIS. Time evolution of a two-dimensional model system. I. Invariant states and time correlation functions. *Journal of Mathematical Physics*, **14**[12]:1746, 1973. 98

[71] P. HARIHARAN, M. GIARRA, V. REDDY, S. W. DAY, K. B. MANNING, S. DEUTSCH, S. F. C. STEWART, M. R. MYERS, M. R. BERMAN, G. W. BURGREEN, E. G. PATERSON, AND R. A. MALINAUSKAS. Multilaboratory particle image velocimetry analysis of the FDA benchmark nozzle model to support validation of computational fluid dynamics simulations. *Journal of Biomechanical Engineering*, **133**[4]:041002, 2011. 14, 39, 72, 73, 74, 86, 95, 103, 119, 168

[72] S. E. HARRISON. *The use of the lattice Boltzmann method in thrombosis modelling.* PhD, University of Sheffield, 2007. 77, 99, 102

[73] X. HE, G. DUCKWILER, AND D. J. VALENTINO. Lattice Boltzmann simulation of cerebral artery hemodynamics. *Computers and Fluids*, **38**[4]:789–796, 2009. 72

[74] X. HE AND L.-S. LUO. Lattice Boltzmann model for the incompressible Navier-Stokes equation. *Journal of Statistical Physics*, **88**[3/4]:927–944, 1997. 78

[75] X. HE AND L.-S. LUO. Theory of the lattice Boltzmann method: From the Boltzmann equation to the lattice Boltzmann equation. *Physical Review E*, **56**[6]:6811–6817, 1997. 78

[76] K. VAN DER HEIDEN, B. P. HIERCK, R. KRAMS, R. DE CROM, C. CHENG, M. BAIKER, M. J. B. M. POURQUIE, F. E. ALKEMADE, M. C. DERUITER, A. C. GITTENBERGER-DE GROOT, AND R. E. POELMANN. Endothelial primary cilia in areas of disturbed flow are at the base of atherosclerosis. *Atherosclerosis*, **196**[2]:542 – 550, 2008. 16

[77] G. HELMLINGER, B. C. BERK, AND R. M. NEREM. Calcium responses of endothelial cell monolayers subjected to pulsatile and steady laminar flow. *American Journal of Physiology: Cell Physiology*, **269**:C367 – C 375, 1995. 21

[78] G. HELMLINGER, R. V. GEIGER, S. SCHRECK, AND R. M. NEREM. Effects of pulsatile flow on cultured vascular endothelial cell morphology. *Journal of biomechanical engineering*, **113**[2]:123, 1991. 143, 160, 161

[79] F. J. HIGUERA AND J. JIMNEZ. Boltzmann approach to lattice gas simulations. *Europhysics Letters*, **9**[7]:663–668, 1989. 78

[80] M. HOFER, G. RAPPITSCH, K. PERKTOLD, W. TRUBEL, AND H. SCHIMA. Numerical study of wall mechanics and fluid dynamics in end-to-side anastomoses and correlation to intimal hyperplasia. *Journal of Biomechanics*, **29**[10]:1297–1308, 1996. 10

[81] I. R. HUTCHESON AND T. M. GRIFFITH. Mechanotransduction through the endothelial cytokeleton: mediation of flow- but not agonist induced EDRF release. *British Journal of Pharmacology*, **118**:720 – 726, 1996. 16

[82] S. IFTIKHAR, A. R. BOND, A. I. WAGAN, P. D. WEINBERG, AND A. A. BHARATH. Segmentation of endothelial cell boundaries of rabbit aortic images using a machine learning approach. *Journal of Biomedical Imaging*, **2011**:4, 2011. 124

[83] C. IOMINI, K. TEJADA, W. MO, H. VAANANEN, AND G. PIPERNO. Primary cilia of human endothelial cells disassemble under laminar shear stress. *Journal of Cell Biology*, **164**:811 – 817, 2004. 16

[84] E. A. JAFFE, R. L. NACHMAN, C. G. BECKER, AND C. R. MINICK. Culture of human endothelial cells derived from umbilical veins. identification by morphologic and immunologic criteria. *Journal of Clinical Investigation*, **52**[11]:2745, 1973. 165

[85] A.D. JEAYS, P.V. LAWFORD, R. GILLOT, P. SPENCER, D.C. BARBER, K.D. BARDHAN, AND D.R. HOSE. Characterisation of the haemodynamics of the superior mesenteric artery. *Journal of Biomechanics*, **40**:1916 – 1926, 2007. 13, 25, 71

[86] A. K. JOSHI, R. L. LEASK, J. G. MYERS, M. OJHA, J. BUTANY, AND C. R. ETHIER. Intimal thickness is not associated with low wall shear stress in the human right coronary artery. *Arteriosclerosis, Thrombosis and Vascular Biology*, **24**:2408 – 2413, 2004. 9, 11, 12

[87] F. KAJIYA, Y. OGASAWARA, K. TSUJIOKA, M. NAKAI, M. GOTO, Y. WADA, S. TADAOKA, S. MATSUOKA, K. MITO, AND T. FUJIWARA. Evaluation of human coronary blood flow with an 80 channel 20MHz pulsed doppler velocimeter and zero-cross and fourier transform methods during cardiac surgery. *Circulation*, **74**[5]:1153–1160, 1986. 50, 70

[88] S. K. KANG AND Y. A. HASSAN. The effect of lattice models within the lattice Boltzmann method in the simulation of wall-bounded turbulent flows. *Journal of Computational Physics*, **232**[1]:100–117, 2012. 98, 99, 169

[89] A. KATSUMI, A. W. ORR, E. TZIMA, AND M. A. SCHWARTZ. Integrins in mechanotransduction. *The Journal of Biological Chemisrty*, **279**[13]:12001–12004, 2004. 16

[90] R. S. KEYNTON, M. M. EVANCHO, R. L. SIMS, N. V. RODWAY, A. GOBIN, AND S. E. RITTGERS. Intimal hyperplasia and wall shear in arterial bypass graft distal anastomoses: an in vivo model study. *Journal of biomechanical engineering*, **123**[5]:464, 2001. 10

[91] H.J. KIM, I.E. VIGNON-CLEMENTEL, J.S. COOGAN, C.A. FIGUEROA, K.E. JANSEN, AND C.A. TAYLOR. Patient-specific modeling of blood flow and pressure in human coronary arteries. *Annals of Biomedical Engineering*, **38**[10]:3195 – 3209, 2010. 13

[92] T. KRÜGER, F. VARNIK, AND D. RAABE. Shear stress in lattice Boltzmann simulations. *Physical Review E*, **79**[4 Pt 2]:046704, 2009. 80, 101

[93] D.N. KU, D.P. GIDDENS, C.K. ZARINS, AND S. GLAGOV. Pulsatile flow and atherosclerosis in the human carotid bifurcation. Positive correlation between plaque location and low oscillating shear stress. *Arteriosclerosis Thrombosis Vascular Biology*, **5**[3]:293–302, 1985. 8, 13, 15

[94] B. L. LANGILLE AND F. O'DONNELL. Reductions in arterial diameter produced by chronic decreases in blood flow are endothelium dependant. *Science*, **231**:405 – 407, 1986. 3, 18

[95] J. LATT AND B. CHOPARD. Lattice Boltzmann method with regularized pre-collision distribution functions. *Mathematics and Computers in Simulation*, **72**[2-6]:165–168, 2006. 78, 80

[96] J. LATT AND ET AL. The Palabos Project, Feb 2013. 72

[97] M. LEI, C. KLEINSTREUER, AND G. A. TRUSKEY. Numerical investigation and prediction of atherogenic sites in branching arteries. *Journal of biomechanical engineering*, **117**[3]:350, 1995. 12

[98] M. J. LEVESQUE, D. LIEPSCH, S. MORAVEC, AND R. M. NEREM. Correlation of endothelial cell shape and wall shear stress in a stenosed dog aorta. *Atherosclerosis*, **6**:220 – 229, 1986. 142

[99] M. J. LEVESQUE, E. A. SPRAGUE, C. J. SCHWARTZ, AND R. M. NEREM. The influence of shear stress on cultured vascular endothelial cells: The stress response of an anchorage-dependent mammalian cell. *Biotechnology progress*, **5**[1]:1–8, 1989. 166

[100] MJ LEVESQUE AND RM NEREM. The elongation and orientation of cultured endothelial cells in response to shear stress. *Journal of Biomechanical Engineering*, **107**[4]:341, 1985. 142, 143

[101] P. LIBBY. Inflammation in atherosclerosis. *Nature*, **420**[6917]:868 – 874, 2002. 4

[102] T. L. LITTLE, J. XIA, AND B. R. DULING. Dye tracers define differential endothelial and smooth muscle coupling patterns within the arteriolar wall. *Circulation Research*, **76**[3]:498 – 504, 1995. 165

[103] Y. LIU, B. P.-C. CHEN, M. LIU, Y. ZHU, M. B. STEMERMAN, S. CHIEN, AND J. Y.-J SHYY. Shear stress activation of SREBP1 in endothelial cells is mediated by integrins. *Arteriosclerosis, Thrombosis and Vascular Biology*, **22**:76 – 81, 2002. 39

[104] M. C. LUZIA, C. M. ALBUQUERQUE, C. M. WATERS, U. SALVA, H. W. SCHNAPER, AND A. S. FLOZAK. Shear stress enhances human endothelial cell wound closure in vitro. *American Journal of Physiology: Heart and Circulatory Physiology*, **279**:H293 – H302, 2000. 166

[105] A. M. MALEK, S. L. ALPER, AND S. IZUMO. Hemodynamic shear stress and its role in atherosclerosis. *Journal of the American Medical Association*, **282**[21]:2035–2042, 1999. 24

[106] A. M. MALEK, G. H. GIBBONS, V. J. DZAU, AND S. IZUMO. Fluid shear stress differentially modulates expression of genes encoding basic fibroblast growth factor and platelet-derived growth factor b chain in vascular endothelium. *Journal of Clinical Investigation*, **92**[4]:2013–2021, 1993. 20

[107] A.M. MALEK AND S. IZUMO. Mechanism of endothelial cell shape change and cytoskeletal remodelling in response to fluid shear stress. *Journal of Cell Science*, **109**:713 – 726, 1996. 19

[108] S. MATSUO, M. TSURUTA, M. HAYANO, Y. IMAMURA, Y. EGUCHI, T. TOKUSHIMA, AND S. TSUJI. Phasic coronary artery flow velocity determined by doppler flowmeter catheter in aortic stenosis and aortic regurgitation. *The American Journal of Cardiology*, **62**[13]:917 – 922, 1988. 50, 70

[109] G. MAYER AND G. HÁZI. Direct numerical and large eddy simulation of longitudinal flow along triangular array of rods using the lattice Boltzmann method. *Mathematics and Computers in Simulation*, **72**[2-6]:173–178, 2006. 77, 99, 102

[110] G. R. MCNAMARA AND G. ZANETTI. Use of the Boltzmann equation to simulate Lattice-Gas automata. *Physical Review Letters*, **61**[20]:2332–2335, 1988. 78

[111] S. MEAGHER, T. L. POEPPING, K. V. RAMNARINE, R. A. BLACK, AND P. R. HOSKINS. Anatomical flow phantoms of the nonplanar carotid bifurcation, part ii: experimental validation with doppler ultrasound. *Ultrasound in medicine & biology*, **33**[2]:303–310, 2007. 13

[112] R. MEI, W. SHYY, D. YU, AND L.-S. LUO. Lattice Boltzmann method for 3-D flows with curved boundary. *Journal of Computational Physics*, **161**[2]:680–699, 2000. 89

[113] S MEIER, A HENNEMUTH, N TCHIPEV, A HARLOFF, M MARKL, AND T PREUSSER. Towards patient-individual blood flow simulations based on PC-MRI measurements. *Proc. Informatik 2011*, pages 447–448, 2011. 14, 72

[114] H. MIAO, Y.-L. HU, Y.-T. SHIU, S. YUAN, Y. ZHAO, R. KAUNAS, Y. WANG, G. JIN, S. USAMI, AND S. CHIEN. Effects of flow patterns on the localization and expression of VE-Cadherin at vascular endothelial cell junctions: In vivo and in vitro investigation. *Arteriosclerosis, Thrombosis and Vascular Biology*, **42**:77 – 89, 2005. 39

[115] J. E. MOORE, E. BURKI, A. SUCIU, S. ZHAO, M. BURNIER, H. R. BRUNNER, AND J-J. MEISTER. A device for subjecting vascular endothelial cells to both fluid shear stress and circumferential cyclic stretch. *Annals of Biomedical Engineering*, **22**:416 – 422, 1994. 26, 28, 35, 69

[116] C. J. MURRAY AND A. D. LOPEZ. Global mortality, disability, and the contribution of risk factors: Global burden of disease study. *The Lancet*, **349**[9063]:1436 – 1442, 1997. 3

[117] H. NAKADATE, Y. HIROSE, E. SEKIZUKA, AND H. MINAMITANI. A new in vitro pulsatile perfusion system that mimics physiological transmural pressure and shear stress in any size of in vivo vessel. *Journal of Biomechanical Science and Engineering*, **3**[1]:25–37, 2008. 27, 30

[118] E. A. NAUMAN, K. J. RISIC, T. M. KEAVENY, AND R. L. SATCHER. Quantitative asessment of steady and pulsatile flow fields in a parallel plate flow chamber. *Annals of Biomedical Engineering*, **27**[2]:194–199, 1999. 67

[119] R. M. NEREM, M. J. LEVESQUE, AND J. F. CORNHILL. Vascular endothelial morphology as an indicator of the pattern of blood flow. *Journal of Biomechanical Engineering*, **103**:172 – 177, 1983. 17

[120] A. C. NEWBY AND A. B. ZALTSMAN. Fibrous cap formation or destruction - the critical importance of vascular smooth muscle cell proliferation, migration and matrix formation. *Cardiovascular Research*, **41**:345 – 360, 1999. 5, 6

[121] S. V. PATANKAR AND D. B. SPALDING. A calculation procedure for heat, mass and momentum transfer in three-dimensional parabolic flows. *International Journal of Heat and Mass Transfer*, **15**[10]:1787–1806, 1972. 82

[122] V. PEIFFER, A. A. BHARATH, S. J. SHERWIN, AND P. D. WEINBERG. A novel method for quantifying spatial correlations between patterns of atherosclerosis and haemodynamic factors. *Journal of Biomechanical Engineering*, **135**[2]:021023–021023, 2013. 15

[123] V. PEIFFER, S. J. SHERWIN, AND P. D. WEINBERG. Does low and oscillaroty wall shear stress correlate spatially with early atherosclerosis? *Cardiovascular Research (in press)*, 2013. 10

[124] O. PELLICCIONI, M. CERROLAZA, AND M. HERRERA. Lattice Boltzmann dynamic simulation of a mechanical heart valve device. *Mathematics and Computers in Simulation*, **75**[1-2]:1–14, 2007. 72, 74

[125] X. PENG, F.A. RECCHIA, B.J. BYRNE, I.S. WITTSTEIN, R.C. ZIEGELSTEIN, AND D.A. KASS. In vitro system to study realistic pulsatile flow and stretch signaling in cultured vascular cells. *American Journal of Physiology - Cell Physiology*, **279**[3 48-3]:C797–C805, 2000. 26, 32

[126] J. E. PHELPS AND N. DEPAOLA. Spatial variations in endothelial barrier function in disturbed flow in vitro. *American Journal of Physiology: Heart and Circulatory Physiology*, **278**:H469 – H476, 2000. 39

[127] M.A. PUNCHARD, C. STENSON-COX, E.D. O'CEARBHAILL, E. LYONS, S. GUNDY, L. MURPHY, A. PANDIT, P.E. MCHUGH, AND V. BARRON. Endothelial cell response to biomechanical forces under simulated vascular loading conditions. *Journal of Biomechanics*, **40**[14]:3146–3154, 2007. 27, 28, 30, 39, 69, 71, 121

[128] Y. H. QIAN, D. D'HUMIÉRES, AND P. LALLEMAND. Lattice BGK models for Navier-Stokes equation. *Europhysics Letters*, **17**[6]:479–484, 1992. 78

[129] U. RAEDLER. A disposable cell culture chip for live cell imaging. *American Biotechnology Laboratory*, **22**:10 – 12, 2004. 28

[130] J. RAVENSBERGEN, J. W. RAVENSBERGEN, J. K. B. KRIJGER, B. HILLEN, AND H. W. HOOGSTRATEN. Localizing role of hemodynamics in atherosclerosis in several human vertebrobasilar junction geometries. *Arteriosclerosis Thrombosis Vascular Biology*, **18**[5]:708–716, 1998. 9

[131] C. P. M. REUTELINGSPERGER, R. G. J. VAN GOOL, V. HEIJNEN, P. FREDERIK, AND T. LINDHOUT. The rotating disc as a device to study the adhesive properties of endothelial cells under differential shear stresses. *Materials in Medicine*, **5**:361 – 367, 1994. 33

[132] E. RINDFLEISCH. *Manual of Pathological Histology*. New Sydenham Society, 1872. 6

[133] J. B. T. M. ROERDINK AND A. MEIJSTER. The watershed transform: Definitions, algorithms and parallelization strategies. *Fundamenta Informaticae*, **41**[1]:187–228, 2000. 138

[134] V.L. ROGER, A.S. GO, D.M. LLOYD-JONES, E.J. BENJAMIN, J.D. BERRY, W.B. BORDEN, D.M. BRAVATA, S. DAI, E.S. FORD, C.S. FOX, ET AL. Heart disease and stroke statistics-2012 update: A report from the American Heart Association. *Circulation*, **125**[1]:e2–e220, 2012. 4, 6

[135] J. ROSSI, P. JONAK, L. ROULEAU, L. DANIELCZAK, J. C. TARDIF, AND R. L. LEASK. Differential response of endothelial cells to simvastatin when conditioned with steady, non-reversing pulsatile or oscillating shear stress. *Annals of Biomedical Engineering*, **39**[1]:402–413, 2011. 19

[136] L. ROULEAU, J. ROSSI, AND R. L. LEASK. Concentration and time effects of dextran exposure on endothelial cell viability, attachment, and inflammatory

marker expression in vitro. *Annals of Biomedical Engineering*, **38**[4]:1451–1462, 2010. 37

[137] R. D. RUDIC, E. G. SHESELY, N. MAEDA, O. SMITHIES, S. S. SEGAL, AND W. C. SESSA. Direct evidence for the importance of endothelium-derived nitric oxide in vascular remodeling. *Journal of Clinical Investigation*, **101**[4]:731, 1998. 3

[138] N. SAKAMOTO, N. SAITO, X. HAN, T. OHASHI, AND M. SATO. Effect of spatial gradient in fluid shear stress on morphological changes in endothelial cells in response to flow. *Biochemical and Biophysical Resaerch Communications*, **395**:264 – 269, 2010. 23, 31, 46, 105, 144, 163

[139] P. M. H. SCHIFFERS, D. HENRION, C. M. BOULANGER, E. COLUCCI-GUYON, F. LANGA-VUVES, H. VAN ESSEN, E. FAZZI, B. I. LEVY, AND J. G. R. DE MAY. Altered flow-induced arterial remodeling in vimentin-deficient mice. *Arteriosclerosis, Thrombosis and Vascular Biology*, **20**:611 – 616, 2009. 16

[140] H. SCHLICHTING. *Boundary Layer Theory*. McGraw Hill Book Company inc., 1955. 37

[141] H. J. SCHNITTLER, R. P. FRANKE, U. AKBAY, C. MROWIETZ, AND D. DREECKHAHN. Improved in vitro rheological system for studying the effect of fluid shear stress on cultured endothelial cells. *American Journal of Physiology: Cell Physiology*, **265**:C289 – C298, 1993. 33

[142] T. SEIMON AND I. TABAS. Mechanisms and consequences of macrophage apoptosis in atherosclerosis. *Journal of Lipid Research*, **50**[Supplement]:S382–S387, 2009. 5

[143] J. SHAO, L. WU, J. WU, Y. ZHENG, H. ZHAO, Q. JIN, AND J. ZHAO. Integrated microfluidic chip for endothelial cells culture and analysis exposed to a pulsatile and oscillatory shear stress. *Lab on a Chip*, **9**:3118 – 3125, 2009. 27, 28

[144] M. L. SMITH, D. S. LONG, E. R. DAMIANO, AND K. LEY. Near-wall micro PIV reveals a hydrodynamicaly relevant endothelial surface layer in venules in vivo. *Biophysical Journal*, **85**:637 – 645, 2003. 15

[145] J. W. SONG, W. GU, N. FUKAI, K. A. WARNER, J. E. NOR, AND S. TAKAYAMA. Computer-controlled microcirculatory support system for endothelial cell culture and shearing. *Analytical Chemistry*, **77**:3993–3999, 2005. 27

[146] S. SRIGUNAPALAN, C. LAM, A. R. WHEELER, AND C. A. SIMMONS. A microfluidic membrane device to mimic critical components of the vascular microenvironment. *Biomicrofluidics*, **9**, 2011. 27, 28

[147] H. C. STARY. Natural history and histological classification of atherosclerotic lesions : An update. *Arteriosclerosis, Thrombosis and Vascular Biology*, **20**:1177 – 1178, 2000. 4

[148] H. C. STARY, A. B. BLEAKLEY, S. GLAGOV, J. R. GUYTON, W. INSULL, M. E. ROSENFELD, S. A. SCHAFFER, C. J. SCHWARTZ, W. D. WAGNER,

AND R. W. WISSLER. A definition of initia, fatty streak, and intermediate lesions of atherosclerosis. *Circulation*, **89**:2462 – 2478, 1994. 4, 5

[149] D. A. STEINMAN, J. B. THOMAS, H. M. LADAK, J. S. MILNER, B. K. BUTT, AND J. D. SPENCE. Reconstruction of carotid birufcation hemodynamics and wall thickness using computational fluid dynamics and MRI. *MRI. Magnetic Resonance Medicine*, **47**:149–159, 2002. 11

[150] S. SUCCI. *The lattice Boltzmann equation for fluid dynamics and beyond*. Oxford University Press, 2001. 72

[151] M. TAMAGAWA, H. KANEDA, M. HIRAMOTO, AND S. NAGAHAMA. Simulation of thrombus formation in shear flows using lattice Boltzmann method. *Artificial Organs*, **33**:604–610, August 2009. 72, 74

[152] J. M. TARBELL. Mass transport in arteries and the localization of atherosclerosis. *Annual Review of Biomedical Engineering*, **5**[1]:79–118, 2003. 8

[153] C.A. TAYLOR AND C.A. FIGUEROA. Patient-specific modelling of cardiovascular fluid mechanics. *Annual Review of Biomedical Engineering*, **11**:109 – 134, 2009. 13, 14, 25

[154] M. M. THI, J. M. TARBELL, S. WEINBAUM, AND D. C. SPRAY. The role of the glycocalyx in reorganization of the actin cytoskeleton under fluid shear stress: a "bumper car" model. *Proceedings of the National Academy of Sciences of the United States of America*, **292**[3]:H1209–H1224, 2007. 161

[155] F. TOSCHI AND S. SUCCI. Lattice Boltzmann method at finite Knudsen numbers. *Europhysics Letters*, **69**[4]:549–555, 2005. 79

[156] E. TZIMA, M. IRANI-TEHRANI, W. B. KIOSSES, E. DEJANA, D. A. SCHULTZ, B. ENGELHARDT, G. CAO, H. DELISSER, AND M. A. SCHWARTZ. A mechanosensory complex that mediates the endothelial cell response to shear stress. *Nature*, **437**:426 – 431, 2005. 16

[157] S USAMI, H.-H. CHEN, Y. ZHAO, S. CHIEN, AND R. SKALAK. Design and construction of a linear shear stress flow chamber. *Annals of Biomedical Engineering*, **21**:77–83, 1993. 30, 46, 68, 105, 106

[158] P. A. VANDERLAAN, C. A. REARDON, AND G. S. GOTZ. Site specifity of atherosclerosis: Site-selective responses to atherosclerotic modulators. *Arteriosclerosis, Thrombosis and Vascular Biology*, **24**:12 – 22, 2004. ix, 10, 11

[159] K. B. VARTANIAN, M. A. BERNY, O. J. T. MCCARTHY, S. R. HANSON, AND M. T. HINDS. Cytoskeletal structure regulates endothelial cell immunogenicity independent of fluid shear stress. *American Journal of Physiology: Cell Physiology*, **298**:C333 – C341, 2010. 18, 143, 162

[160] H. K. VERSTEEG AND W. MALALASEKERA. *An introduction to computational fluid dynamics: The finite volume method.* Pearson Education ltd., 2007. 72

[161] H. VINK AND B. R. DULING. Capillary endothelial surface layer selectively reduces plasma solute distribution volume. *American Journal of Physiology: Heart and Circulatory Physiology*, **278**:H285 – H289, 2000. 15

[162] C. WANG, H. LU, AND M. A. SCHWARTZ. A novel in vitro flow system for changing flow direction on endothelial cells. *Journal of Biomechanics*, **45**:1212–1218, 2012. 28

[163] N. WANG, H. MIAO, Y.-S. LI, P. ZHANG, J. H. HAGA, Y. HU, A. YOUNG, S. YUAN, P. NGUYEN, C.-C. WU, AND S. CHIEN. Shear stress regulation of kruppel-like factor 2 expression is flow pattern-specific. *Biochemical and Biophysical Research Communications*, **341**[4]:1244–1251, 2006. 19, 30, 46, 105, 165

[164] C. M. WARBOYS, N. AMINI, A. DE LUCA, AND P. C. EVANS. The role of blood flow in determining the sites of atherosclerotic plaques. *F1000 medicine reports*, **3**, 2011. 8

[165] C.M. WARBOYS, R.E. BERSON, G.E. MANN, J.D. PEARSON, AND P.D. WEINBERG. Acute and chronic exposure to shear have opposite effects on endothelial cell permeability to macromolecules. *American Journal of Physiology - Heart and Circulatory Physiology*, **298**:H1850 – H1856, 2010. 8, 17, 30, 165

[166] S. WEINBAUM, J. M. TARBELL, AND E. R. DAMIANO. The structure and function of the endothelial glycocalyx layer. *Annual Review of Biomedical Engineering*, **9**:121 – 167, 2007. 16

[167] P. D. WEINBERG. Rate-limiting steps in the development of atherosclerosis: The response-to-influx theory. *Journal of Vascluar Research*, **41**[1]:1 – 17, 2004. 8, 17

[168] J. J. WENTZEL, Y. S. CHATZIZISIS, F. J. GIJSEN, G. D. GIANNOULOU, C. L. FELDMAN, AND P. H. STONE. Endothelial shear stress in the evolution of coronary atherosclerotic plaque and vascular remodelling: current understanding and remaining questions. *Cardiovascular Research*, **96**:234–243, 2012. 7

[169] J. J. WENTZEL, F. J. GIJSEN, J. C. SCHUURBIERS, R. KRAMS, P. W. SERRUYS, AND P. J. DE FEYTER. Geometry guided data averaging enables the interpretation of shear stress related plaque development in human coronary arteries. *Journal of Biomechanics*, **38**:1551–1555, 2005. 11, 12

[170] A. T. WHITE AND C. K. CHONG. A dynamic flow-bioreactor system for subjecting endothelial cells to physiological shear stress and shear gradients. *Oral presentation at Bioengineering11, Queen Mary, University of London, 12 - 13 September 2011*, 2011. 168

[171] A. T. WHITE AND C. K. CHONG. Rotational invariance in the three-dimensional lattice Boltzmann method is dependent on the choice of lattice. *Journal of Computational Physics*, **230**[16]:6367–6378, 2011. 169

[172] A. T. WHITE AND C. K. CHONG. Effects of physiologically realistic shear stress profiles on endothelial cell morphology. *Journal of Biomechanics*, **45**:S438, 2012. 169

[173] A. T. WHITE AND C. K. CHONG. Effects of physiologically realistic shear stress waveforms on endothelial cell morphology. *Oral presentation at ESB2013, Patras, Greece, 25-28 August 2013*, 2013. 170

[174] C.R. WHITE, H.Y. STEVENS M. HAIDEKKER, AND J.A. FRANGOS. Temporal gradients in shear stress, but not spatial gradients, stimulate ERK1/2 activation in endothelial cells. *American Journal of Physiology: Heart and Circulatory Physiology*, **289**:H2350 – H2355, 2005. 22, 29

[175] C.R. WHITE, M. HAIDEKKER, X. BAO, AND J.A. FRANGOS. Temporal gradients in shear stress, but not spatial gradients, stimulate endothelial cell proliferation. *Circulation*, **103**:2508 – 2513, 2001. 22, 26, 29, 30, 39

[176] N. B. WOOD, S. Z. ZHAO, A. ZAMBANINI, M. JACKSON, W. GEDROYC, S. A. THOM, A. D. HUGHES, AND X. Y. XU. Curvature and tortuosity of the superficial femoral artery: a possible risk factor for peripheral arterial disease. *Journal of Applied Physiology*, **101**[5]:1412–1418, 2006. 10, 13

[177] WORLD HEALTH ORGANISATION. World health organisation statistics 2009 - cause specific mortality and morbidity, 2009. 3

[178] H. P. WRIGHT. Mitosis patterns in the aortic endothelium. *Atherosclerosis*, **15**:93 – 100, 1972. 18

[179] F. L. XIONG AND C. K. CHONG. PIV-validated numerical modeling of pulsatile flows in distal coronary end-to-side anastomoses. *Journal of Biomechanics*, **40**[13]:2872–2881, 2007. 14, 39, 70, 95

[180] F. L. XIONG AND C. K. CHONG. Numerical study on the influence of anastomotic configuration on hemodynamics in miller cuff models. *Annals of Biomedical Engineering*, **37**[2]:310 – 314, 2009. 70

[181] F.L. XIONG AND C.K. CHONG. A parametric numerical investigation on haemodynamics in distal coronary anastomoses. *Medical Physics and Engineering*, **30**:311 – 320, 2008. 14, 70

[182] Q. XU. Disturbed flow-enhanced endothelial turnover in atherosclerosis. *Trends in cardiovascular medicine*, **19**[6]:191–195, 2009. 18

[183] A. YEE, K. A. BOSWORTH, D. E. CONWAY, S. G. ESKIN, AND L. V. MCINTIRE. Gene expression of endothelial cells under pulsatile non-reversing vs. steady shear stress; comparison of nitric oxide production. *Annals of Biomedical Engineering*, **36**[4]:571–579, 2008. 17, 18, 22

[184] A. YEE, Y. SAKURAI, S. G. ESKIN, AND L. V. MCINTIRE. A vaildated system for simulating common carotid arterial flow in vitro: alteration of endothelial cell response. *Annals of Biomedical Engineering*, **34**[4]:593 – 604, 2006. 21, 27, 34, 67, 69, 143

[185] E. W. K. YOUNG AND C. A. SIMMONS. Macro- and microscale systems for endothelial cell biology. *Lab on a Chip*, **10**:143 – 160, 2009. 40

[186] W. P. YUDISTIAWAN, S. K. KWAK, D. V. PATIL, AND S. ANSUMALI. Higher-order Galilean-invariant lattice Boltzmann model for microflows: Single-component gas. *Physical Review E*, **82**[4]:046701, 2010. 102

[187] M. ZAKKAR, K. VAN DER HEIDEN, L. A. LUONG, H. CHAUDHURY, S. CUHLMANN, S. S. HAMDULAY, R. KRAMS, I. EDIRISINGHE, I. RAHMAN, H. CARLSEN, D. O. HASKARD, J. C. MASON, AND P. C. EVANS. Activation of Nrf2 in endothelial cells protects arteries from exhibiting a proinflammatory state. *Arteriosclerosis, thrombosis, and vascular biology*, **29**[11]:1851–1857, 2009. 19, 165

[188] C.K. ZARINS, D.P. GIDDENS, B.K. BHARADVAJ, V.S. SOTTIURAI, R.F. MABON, AND S. GLAGOV. Carotid bifurcation and atherosclerosis. Quantitative correlation of plaque localization with flow velocity profiles and wall shear stress. *Circulation Research*, **53**:502 – 514, 1983. 9

[189] Y. ZHAO, B. P. C. CHEN, H. MIAO, S. YUAN, Y. S. LI, Y. HU, D. M. ROCKE, AND S. CHIEN. Improved significance test for microarray data: temporal effects of shear stress on endothelial genes. *Physiological Genomics*, **12**:1 – 11, 2002. 19

[190] H. ZHU, Z. DING, R. N. PIANA, T. R. GEHRIG, AND M. H. FRIEDMAN. Cataloguing the geometry of the human coronary arteries: a potential tool for predicting risk of coronary artery disease. *International Journal of Cardiology*, **135**[1]:43–52, 2009. 10